# Triplet exciton management towards electrically driven organic lasers

コホナ，パハラ，ワラウェ，ブッディカ，サンジーワ，バンダラ，カルナティラカ

2020

Doctoral Dissertation

# Triplet exciton management towards electrically driven organic lasers

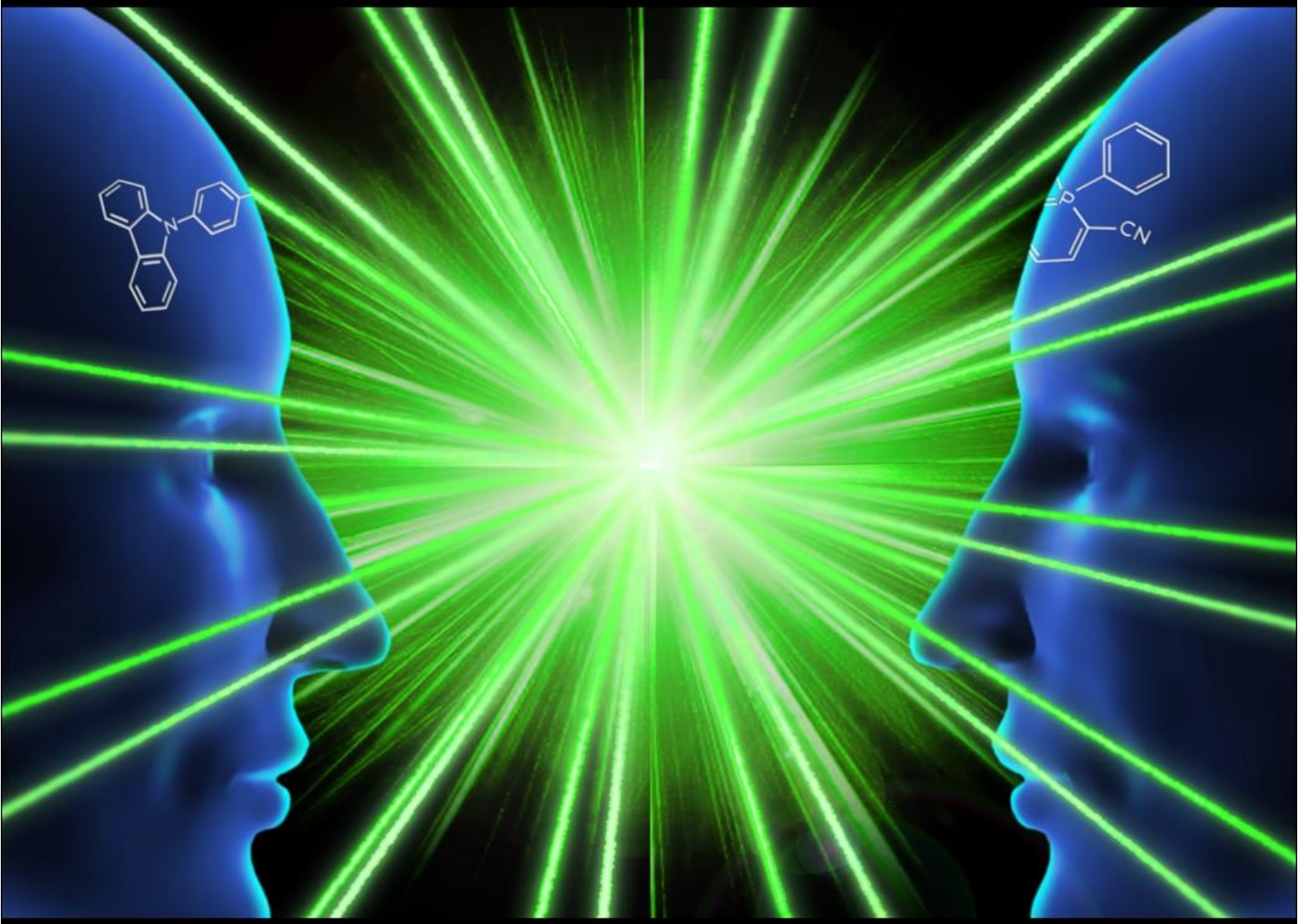


**Kohona Pahala Walawwe Buddhika Sanjeewa Bandara Karunathilaka**

**Department of Chemistry and Biochemistry**
**Graduate School of Engineering**
**Kyushu University**

2020

Doctoral Dissertation

# Triplet exciton management towards electrically driven organic lasers

Kohona Pahala Walawwe Buddhika Sanjeewa Bandara Karunathilaka

Department of Chemistry and Biochemistry
Graduate School of Engineering
Kyushu University

# Table of contents

# Chapter 1

## Introduction

## 1.1 History of lasers

The word "laser" is an acronym for "Light Amplification by Stimulated Emission of Radiation". Albert Einstein in 1917 theoretically proved that the process of stimulated emission must exist[1,2]. In fact, very first amplification of electromagnetic radiation was demonstrated in microwave wavelength, i.e., "Microwave Amplification by Stimulated Emission of Radiation (Maser)[3], by the group of scientists headed by Charles S. Towns in 1954. In 1960, T. H. Maiman of the Hughes Research Laboratories achieved the very first laser action from Ruby crystal in optical frequency[4]. Successively, in 1962, Robert N. Hall demonstrated the first semiconductor laser using Gallium-Arsenide[5]. Since 1962, the development of lasers has been extremely rapid[2,6]. In particular, the very first stimulated emission from an organic material was reported by Sorokin *et al.* in 1966[7]. Figure 1.1 shows the important milestones in the invention and innovations of laser technology.

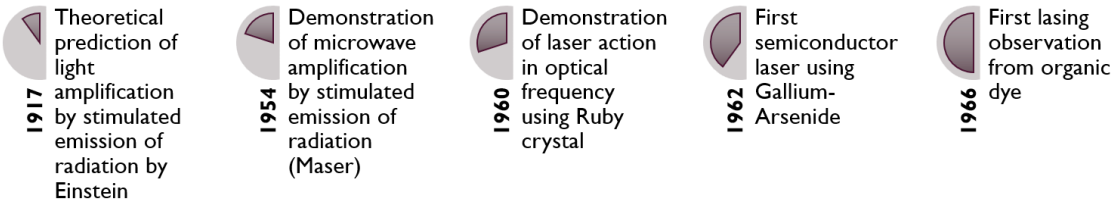


**Figure 1.1.** Significant milestones of laser technology[2,6].

Now, the term of "laser" stands for a device having a gain medium which amplifies light by stimulated emission, a resonator which induces feedback of light (i.e., light travels back and forth through the gain medium) and a pumping source which keeps the population inversion during stimulated emission[8,9].

## 1.2 Introduction to organic lasers

### 1.2.1 Organic semiconductor materials

Energy levels of inorganic semiconductors are well explained based on the band

structures which originate from the properties of crystalline structures of inorganic materials[10]. In general, there are valence and conduction bands which are separated by a forbidden energy gap (bandgap). However, unlike inorganic crystals, organic molecules are usually characterized with molecular orbital theory. Therefore, although there are significant differences in their electronic structures, it is usually assumed that the highest occupied molecular orbital (HOMO) and lowest unoccupied molecular orbital (LUMO) of an organic solid-state are analogous to the valence and conduction bands of an inorganic solid-state, respectively[11–13].

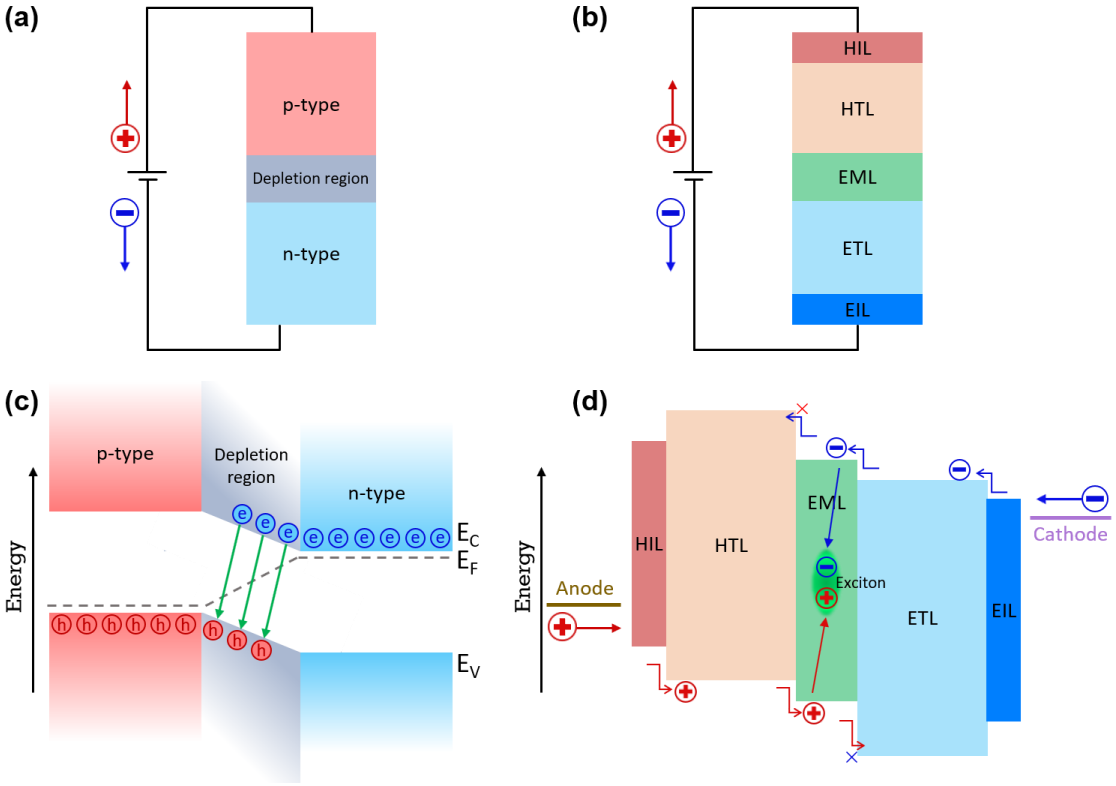


**Figure 1.2.** Schematic device architectures of conventional (a) inorganic and (b) organic LEDs. Energy-level diagrams of conventional (c) inorganic and (d) organic LEDs. In these figures, $E_C$ is the energy level of a conduction band, $E_F$ is the energy of a Fermi level, $E_V$ is the energy level of a valence band. HIL is the hole injection layer, HTL is the hole transport layer, EML is the emitting layer, ETL is the electron transport layer, and EIL is the electron injection layer.

In addition, here I highlight the difference of electroluminescence (EL) processes between organic and inorganic semiconductors. In inorganic semiconductors, an electron

and a hole recombination occur through the electron transition between the conduction and valence bands, leading to radiative or non-radiative decay with photon or phonon emission respectively (Figure 1.2a,c). In contrast, injected and transported holes and electrons recombine in a molecule, forming an exciton[13] (Figure 1.2b,d) with the branching ratio of 1:3 in singlet and triplet states[14]. Compared to the band-to-band transition in inorganic semiconductors, the exciton generation is the most unique process in organic semiconductors.

### 1.2.2 Organic laser gain materials

Analogous to a four-level energy scheme of inorganic laser materials, common organic fluorescent materials possess the similar energy diagram[15] (Figure 1.3). In general, internal conversion between vibration energy levels within the same electronic state is faster than the transition between different electronic states. As depicted in Figure 1.3a, the vibrational transitions between $E_3$ to $E_2$, and $E_1$ to $E_0$ are usually in a picosecond regime. The transition between $E_2$ to $E_1$ is either radiative or non-radiative, and this spontaneous transition is called fluorescence emission. Relationship between radiative and non-radiative transitions can be expressed using the following equation:

$$\Phi_{PL} = k_r \times \tau_s = \frac{k_r}{k_r + k_{nr}} \quad \text{(Eq. 1.1)}$$

where, $\Phi_{PL}$, $k_r$, $\tau_s$ and $k_{nr}$ are the photoluminescence quantum yield (PLQY), radiative decay constant, fluorescence emission lifetime (corresponding to a lifetime of singlet excited state) and nonradiative decay constant, respectively. As depicted in Figure 1.3b, a fluorescence emission spectrum is a combination of several transitions between the lowest vibrational energy level of the upper electronic state ($E_2$) to several different vibrational states of the ground electronics state ($E_1$). Thus, using a waveguided feed-back resonator, it is possible to isolate one particular transition as the stimulated emission while suppressing other transitions.

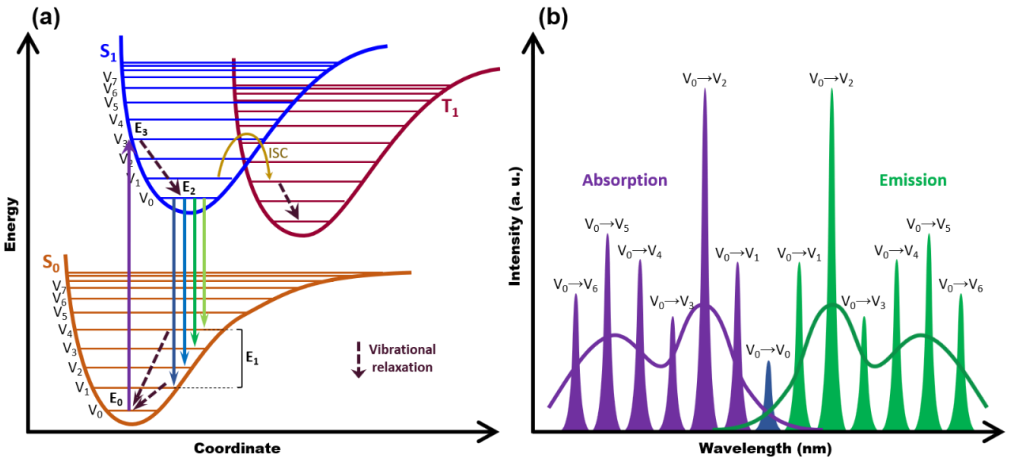


**Figure 1.3.** (a) Frank-Condon energy level diagram of a four-level organic fluorescent laser gain material. (b) Respective absorption and emission spectra showing vibrational peaks[16].

When the excitation pump energy is increased, the gain of stimulated emission surpasses the optical losses, and then the light amplification begins[15,17]. The minimum required pump energy to begin light amplification is defined as the threshold energy, $E_{th}$. The $E_{th}$ of a slab-waveguide thin film on a low-refractive-index substrate can be expressed as amplified spontaneous emission (ASE) threshold, which is given by;

$$E_{th} = C' \frac{1}{\Gamma n_{eff} \Phi_{PL}} \left( \int \frac{\sigma_a}{\lambda} d\lambda \right)^{-2} \quad \text{(Eq. 1.2)}$$

where $C'$ is a constant, $\Gamma$ is the confinement factor, $n_{eff}$ is the effective refractive index in an emission region, $\sigma_a$ is the steady-state absorption cross-section, and $\lambda$ is the wavelength. Here, if Eq. 1.3 satisfies;

$$\left( \int \frac{\sigma_a}{\lambda} d\lambda \right) = constant \quad \text{(Eq. 1.3)}$$

Then, $E_{th}$ is inversely proportional to $k_r$ as;

$$E_{th} \propto 1 + \frac{k_{nr}}{k_r} \quad \text{(Eq. 1.4)}$$

Therefore, to reduce $E_{th}$, we have to use a material with higher PLQY, shorter $\tau_s$ or higher $k_r$[17,18]. There are thousands of organic molecules exhibiting laser characteristics reported from 1966 up to date which have different, unique and special properties based on each class of molecules[11,13,15]. Figure 1.4 shows few common examples of polymers and small

molecules that exhibit light amplification under optical excitation over whole visible region[19,20].

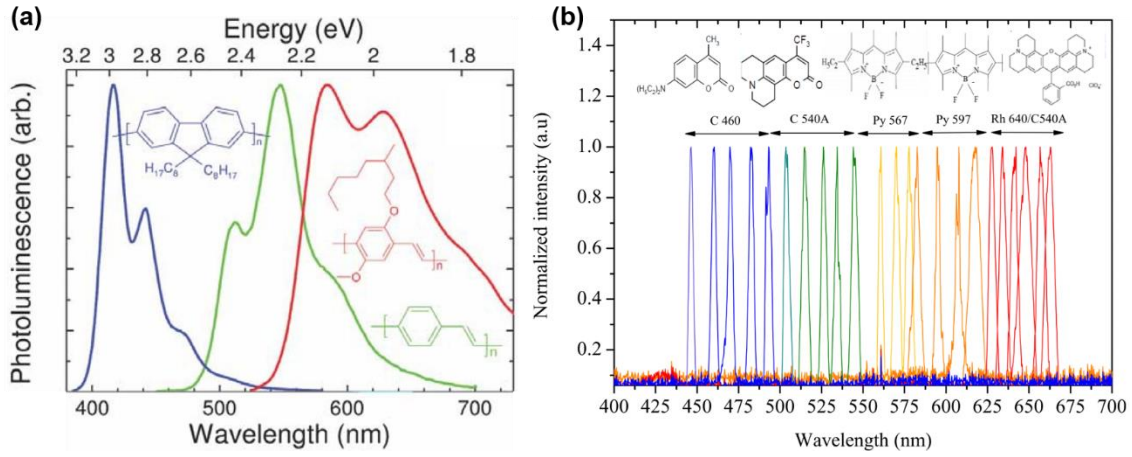


**Figure 1.4.** (a) Emission spectra of three commonly used conjugated polymers for lasing. (a-inset) respective polymer structures[21]. (b) Laser spectra of coumarin 460 (C 460, blue solid line), coumarin 540 A (C 540 A, green solid line), pyrromethene 567 (Py 567, light orange solid line), pyrromethene 597 (Py 597, dark orange solid line), and a blend of rhodamine 640 (Rh 640) and C 540 A (red solid line)[22].

### 1.2.3 Optically pumped organic lasers

After the first demonstration of ASE from an organic material in March 1966[7], Schafer *et al.* reported the first organic laser in September 1966[23]. Later, the continuous-wave (CW) operation from organic lasers was demonstrated by Peterson *et al.* in 1970[24]. However, most of the organic lasers used solutions of π-conjugated highly luminescent molecules as the gain medium, which were sometimes inconvenient to solid-state applications[25]. Another organic laser was proposed in 1967[26], with the incorporation of organic laser dyes into solid-state polymeric matrices, indicating that these devices have the benefit to convenient, compact light sources with a low cost[27]. The first organic solid-state semiconductor laser (OSSL) under optical pulse pumping was demonstrated by Hide *et al.* in 1996[28,29], and the lasing from solid-state conjugated polymer microcavities was also reported by Tessler *et al.* in the same year[30].

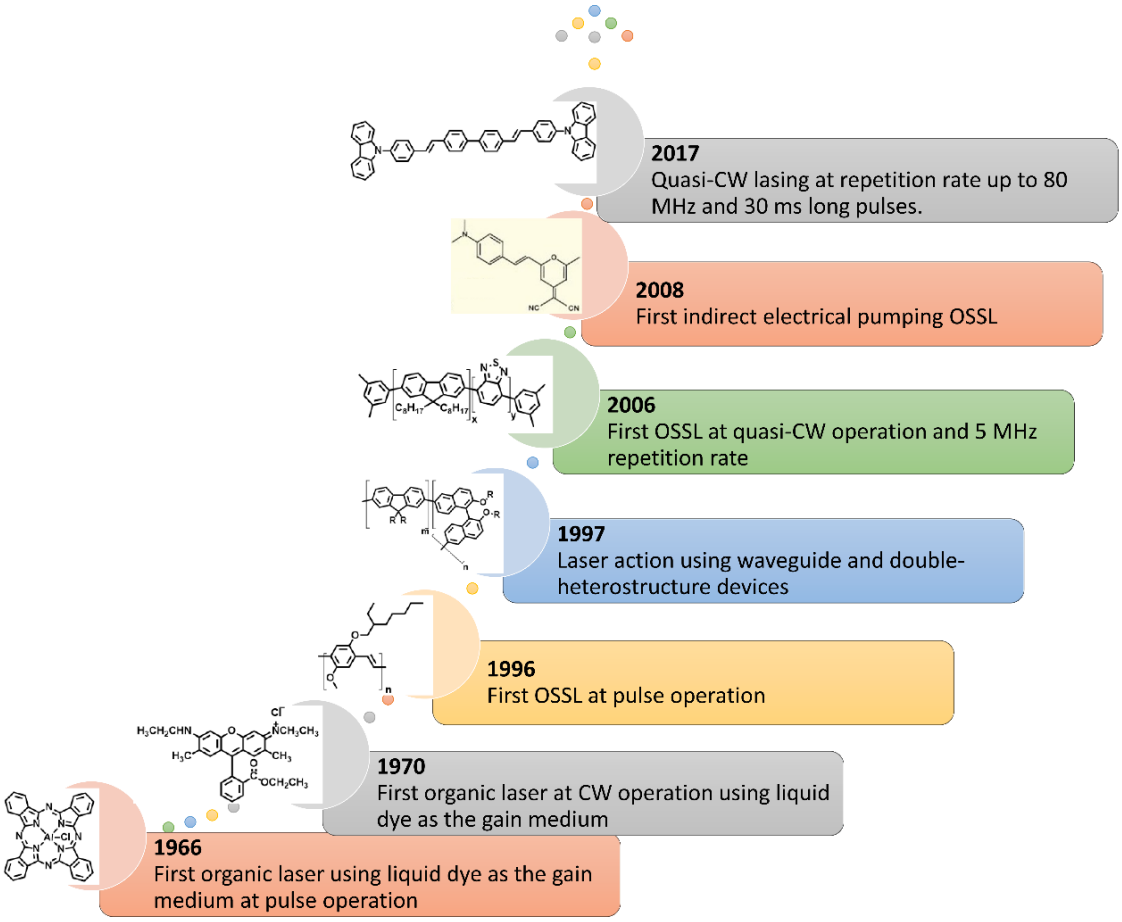


**Figure 1.5.** The milestones in the history of breakthrough innovations and inventions of organic lasers.

Subsequently, many researchers then focused on improving the photostability of laser dyes and host matrix molecules to decrease the required pump thresholds under the CW condition and to realize electrically driven organic semiconductor laser diodes (OSLDs)[27,29,31]. The first optically pumped quasi-CW lasers from organic solid-state films were realized by Rabe *et al.* in 2006[32], and an indirect electrical pumping OSSLs, which otherwise called as a tandem laser diode, was reported by Yang *et al.* in 2008[33,34]. Further, Sandanayaka *et al.,* demonstrated low threshold surface-emitting OSSLs operating in the quasi-CW regime at 80 MHz as well as under long pulse photo-excitation of 30 ms in 2017[35–37]. Now, true-CW (t-CW) lasing in organic semiconductor films attracts great interest. The milestones in the organic laser history are

summarized in Figure 1.5.

### 1.2.4 Organic light-emitting diodes and electrical injection organic semiconductor laser diodes

The very first EL from organic materials was reported in 1963 by Pope *et al.*[38] and the first practical multi-layered OLEDs were realized in 1986 by Hayashi *et al.*[39,40]. Later, Tang and Vanslyke demonstrated efficient EL using a bilayer device, which produced high brightness ( > 1000 cd $m^{-2}$) with the voltage less than 10 V and high external quantum efficiency (EQE) of about 1 %[39]. Then, Adachi *et al.* reported a fundamental double hetero-architecture consisting of an HTL, an EML and an ETL in 1988[40]. These first-generation OLEDs are referred to as fluorescent OLEDs based on the radiative recombination of singlet excitons. Later, Baldo *et al.* reported a phosphorescent mechanism, i.e., all singlet excitons rapidly decay to a triplet state by intersystem crossing (ISC) and the generated triplet excitons decay radiatively by employing organometallic compounds such as $Ir(ppy)_3$ in 1998[41]. The devices exploiting such a mechanism are called phosphorescent OLEDs (PHOLEDs) and became the second generation of OLEDs[42]. Later, a very promising alternative mechanism that converts triplet excitons into a singlet state was firstly demonstrated by Adachi group in 2009[43] and their successive studies realized ultimate OLEDs with a high EQE over 20 % by utilizing very efficient triplet up-conversion via reverse-ISC (RISC)[44]. This mechanism is named as thermally activated delayed fluorescence (TADF) and became the third generation of OLEDs as TADF-OLEDs[45,46].

Although the performance of OLEDs has been rapidly developed to the level of practical applications such as displays and lighting, fabricating OSLDs has been a still very difficult task due to Joule heating[47], wave guiding loss[37], quenching of radiative singlets by triplets (singlet-triplet annihilation; STA) or polarons (singlet-polaron

annihilation; SPA) simultaneously[48–52]. In particular, utilization of organic materials with low laser thresholds is crucial to make the threshold currents lower for OSLDs[53,54].

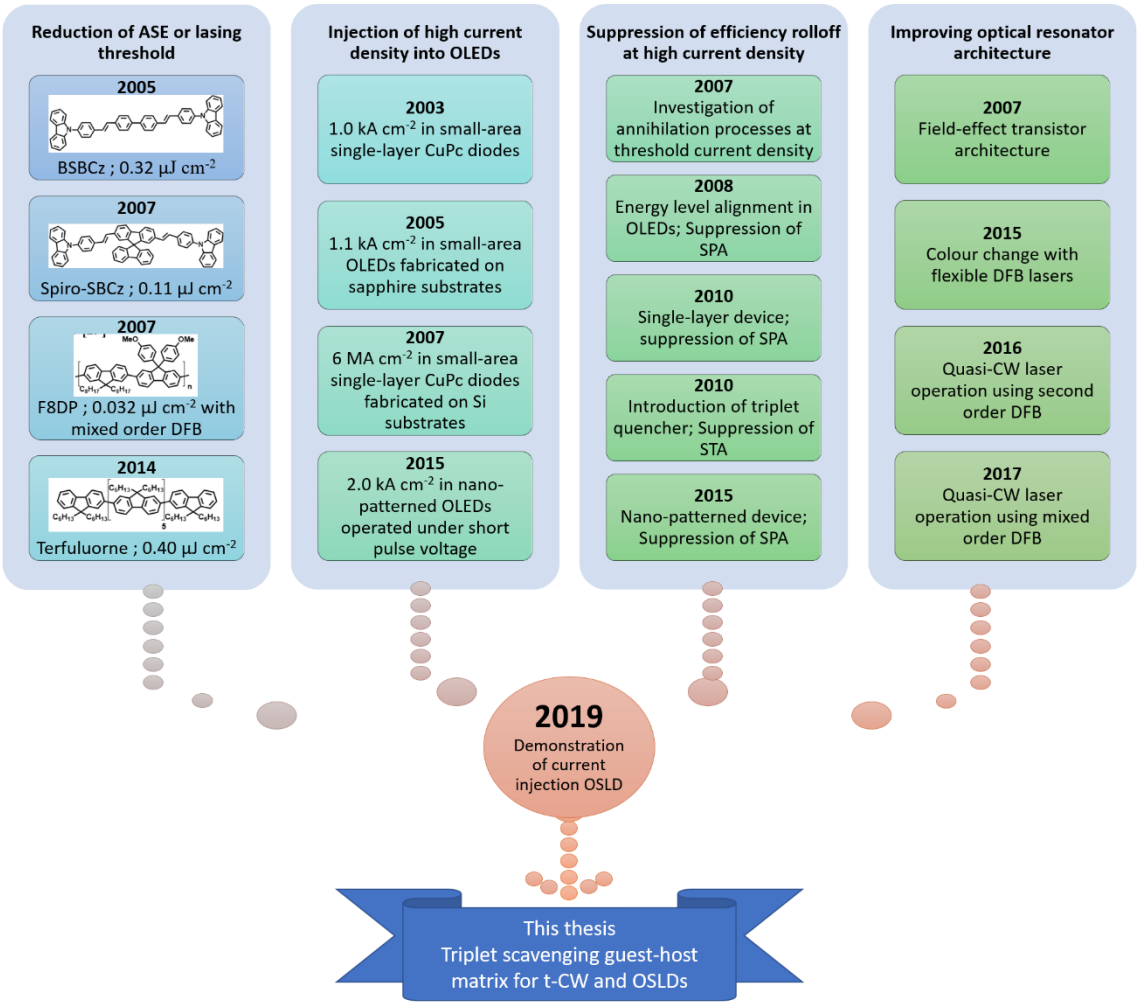


**Figure 1.6.** Work done in Adachi laboratory to overcome issues affecting for the realization of current injection OSLDs.

To overcome the aforementioned issues, as shown in Figure 1.6, Adachi laboratory has been developed many organic laser dye materials having low ASE and laser thresholds[55–59] with emission colors ranging from deep blue to near IR regime[59]. Light amplification from a TADF material was also reported in 2017[60]. Degradation mechanism of laser dyes[61] and design strategies of robust laser dyes[62] have been clarified. Molecular orientation of efficient laser gain materials has been investigated in order to get better lasing characteristics[63]. Several device and resonator architectures

were investigated to decrease wave guiding losses of distributed feed-back resonators (DFBs)[20,36,37] in OLED and organic field effect transistor (OFET) structures[57]. Use of short pulse electrical excitation has been investigated in order to drive OLEDs and OSLDs at higher current densities with reduced joule heat[47,53,64]. Using triplet quencher molecules in order to manage triplet excitons and effects of STA has been investigated[35,61,65]. Moreover, laser operation under quasi-CW operation has been demonstrated by Sandanayaka *et al.*[35–37]. More interestingly, a record-breaking publication about an indication of current injection lasing from OSLDs was reported recently in 2019 by Sandanayaka *et al.*[53]. Afterward, there are huge attentions has been paid about current excitation and various efforts for reducing the current threshold have been started.

One of the big issues frequently observed in OLEDs is the significant decrease in external quantum efficiency (EQE) at high current densities. This decrease in EQE is termed as “efficiency roll-off”. Major reasons for the efficiency roll-off are triplet induced emission quenching such as STA[37,52,55,66] and SPA. In fact, to suppress roll-off characteristics, it has been clarified that the use of non-heterostructured device architecture leads to suppression of roll-offs (Figure 1.7e), since the heterointerfaces tend to accumulate charge carriers and squeezing the carrier recombination width (Figure 1.7b).

Due to the localization of charge carriers and excitons in organic molecules in case of organic semiconductors, the interaction between charge carriers (radical cations and anions; polarons) and the adjacent molecules is much stronger than that of inorganic compounds. Thus, polaron induced exciton quenching causes serious issues in OSLD performance at higher current densities[53,64]. As shown in Figure 1.7a,c, charge injection in a multilayer device is relatively easier and controllable by combining appropriate HTL and ETL materials. Other advantage of the multilayer devices is charge blocking ability at either side of EML that can confine charges in EML, leading to high efficiency

(Figure 1.2d and Figure 1.7b)[46]. However, in case of OSLDs, these HTLs and ETLs can yield additional emission quenching sites by the cation and anion absorptions in HTL and ETL, respectively (Figure 1.8), since light travels back and forth between anode and cathode before light is outcoupled[53,64].

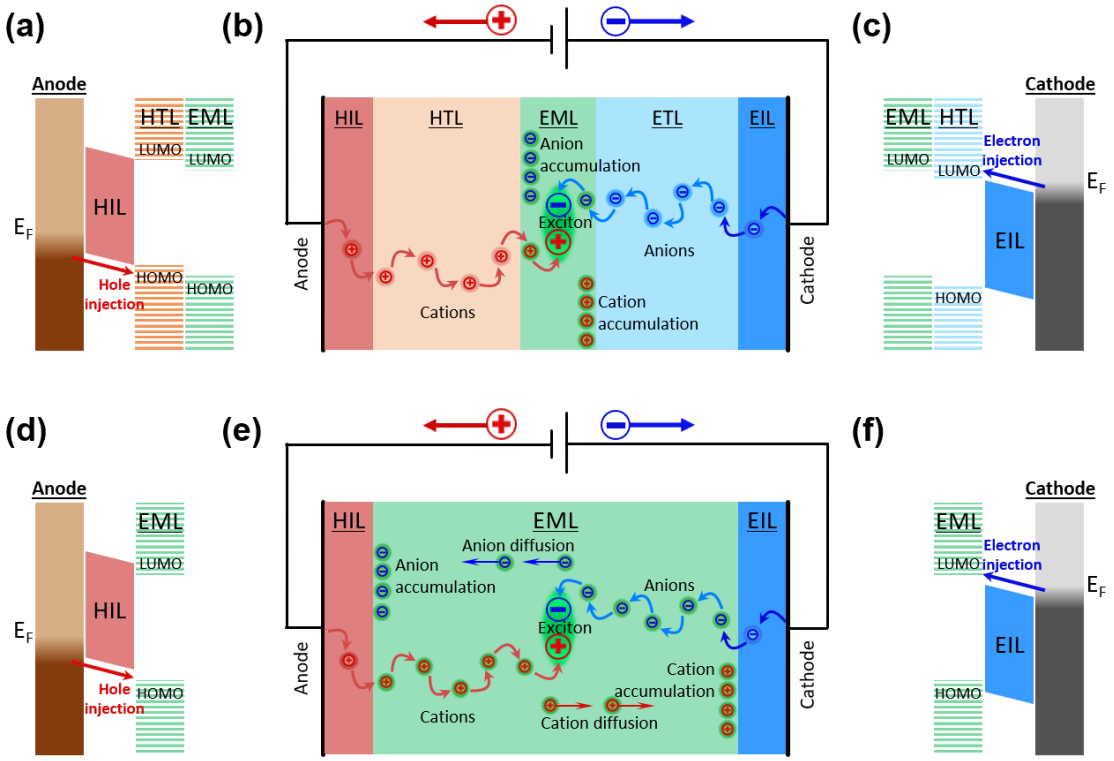


**Figure 1.7.** Schematic of multilayer OLED; (a) hole injection from anode (b) charge hopping and recombination (c) electron injection from cathode. Schematic of single layer OLED; (d) hole injection from anode (e) charge hopping and recombination (f) electron injection from cathode[53,67–70].

Therefore, single layer OLED architecture is vital since we only need to consider about the polaron absorption of an EML material to suppress polaron quenching (Figure 1.7e, Figure 1.8)[53,64]. However, even if the numbers of injected electrons and holes are same, the mobilities of holes and electrons may still be different. Thus, this may lead to non-radiative recombination of holes and electrons near the interface between the injection layer and EML, leading to low efficiency and a high driving voltage[53,67–70]. Specially at high voltages, holes and electrons may drift towards the counter electrodes without recombination each other[47,64]. Therefore, in order to get ideal charge balance in

single layer devices, we have to carefully optimize charge injection and transport characteristics (Figure 1.7d,f)[53,64,71].

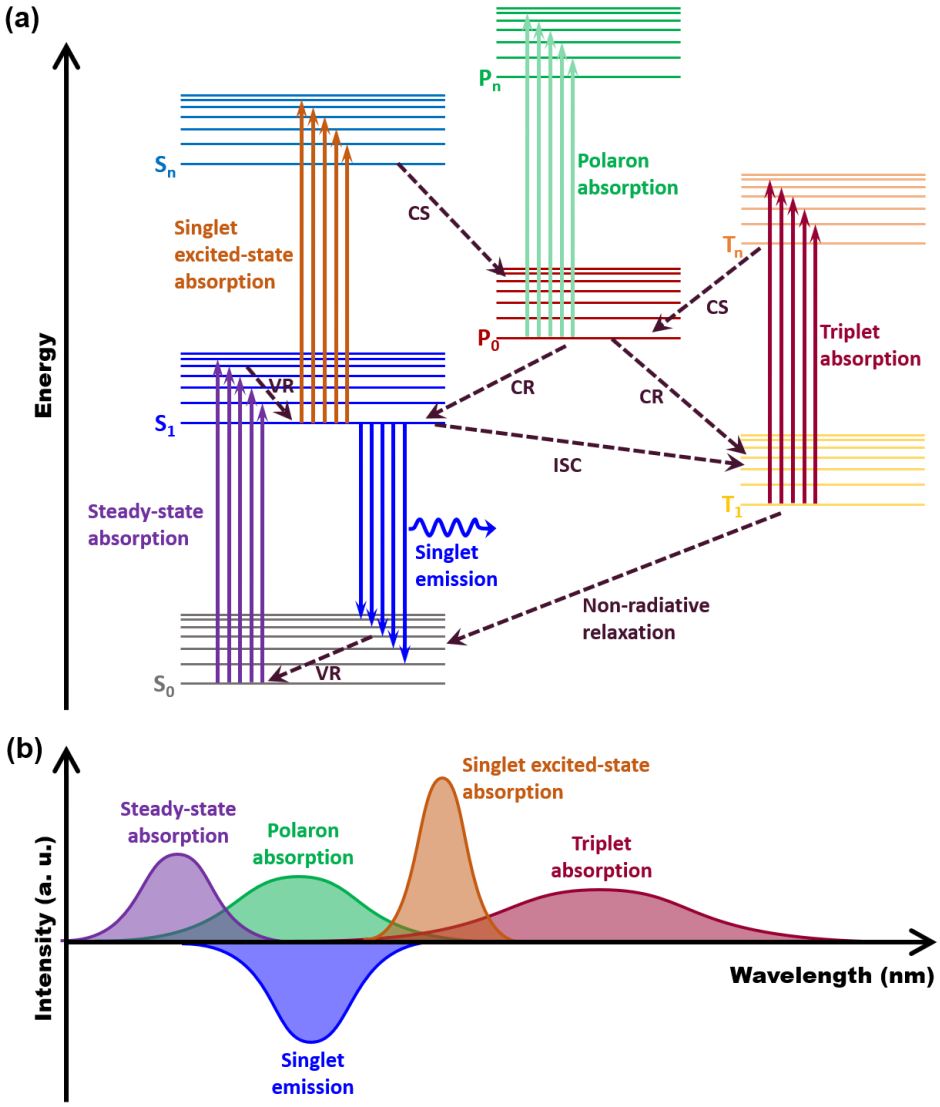


**Figure 1.8.** Various quenching mechanisms affecting to a typical organic laser gain material under current injection; (a) Jablonski energy diagram (b) respective emission and absorption spectra. CR, CS, VR and ISC stands for charge separation, charge recombination, vibrational relaxation and intersystem crossing respectively.

### 1.2.5 Advantages of OSLDs

Lasers have extremely unique and useful properties such as high intensity, directionality, monochromatic emission, and coherence. Due to these properties, lasers have found applications in almost every industrial sector, for example, in scanners,

printers, and sensors. Until now, lasers for these applications are typically based on inorganic materials which are generally brittle, nonflexible, and high cost processing[8,17].

In contrast to inorganic semiconductors, organic semiconductor materials are generally easier to process, and the resulting devices can be mechanically flexible. Thus, lasing from organic semiconductor materials can be used for a wide range of applications such as displays[72], lighting[29,31], sensors[73], optical communications[74,75] and spectroscopy[31]. Interestingly, OLEDs paved the way to curved displays which are commercially available now. Pixels in those displays outcouples light with Lambertian distribution. However, if we can make those pixels with OSLDs which outcouple highly directional laser light, OSLDs can pioneer new applications such as curved holographic displays that can create virtual objects in 3D space outside of the display plane[76–79].


**Figure 1.9.** Potential applications of current injection OSLDs.

Moreover, due to the ultimate opportunities to change the molecular structures of lasing materials, we can tune the emission wavelength[27] and may optimize the material stability[62], crystallinity, PLQY and electronic energy levels[80]. In addition, organic emitter materials are often biodegradable, and devices based on them will be

environmental-friendly. Due to their facile processability, they are compatible with a large variety of optical resonator structures and, in many cases, the resonator can be inscribed directly into the organic gain medium, leading to versatile and relatively low-cost laser devices. Few examples for future potential applications of current injection OSLD is given in Figure 1.9.

## 1.3 Triplet excitons management in organic laser

### 1.3.1 Triplet accumulation

Regarding organic laser materials, the formation of long-lived triplet excitons and triplet accumulation is one of the major disadvantages. The population of triplet excitons mainly depends on the rates of triplet formation and relaxation (Figure 1.10a,b). In a pristine film, the rate of triplet exciton formation solely depends on the rate of intersystem crossing (ISC) from a singlet state to a triplet state which is an intrinsic property of the molecule. However, as shown in Figure 1.10a, in case of a guest-host system, the rate of triplet exciton formation depends on triplet sensitization and the molar ratio. On the other hand, under electrical excitation, triplets are formed on emitter molecules either as direct exciton formation by charge recombination on emitter molecules or as triplet sensitizing by host molecules in a guest-host system (Figure 1.10b). Therefore, with an increase of current density, the rate of triplet formation significantly increases due to the branching ratio of singlets and triplets (1:3)[14]. Therefore, at high current densities, triplet accumulation and triplet induced losses can be a serious problem in OSLDs and decrease the operational durability[61].

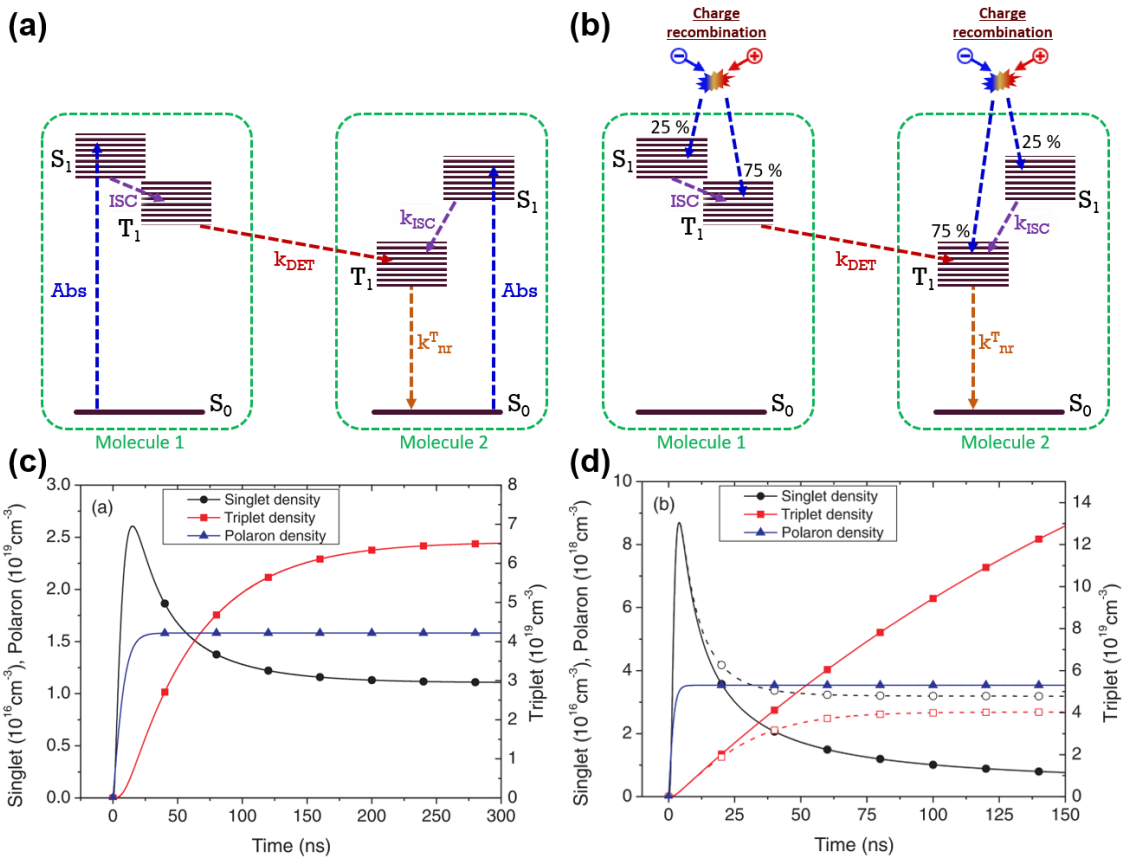


**Figure 1.10.** Rate of exciton dynamics related to triplet accumulation; (a) optical excitation (b) electrical excitation. Calculated exciton density versus long pulsed electrical excitation in a guest-host film at a current density of 1 kA/cm$^2$; (c) without (d) with considering electric field across the electrodes. The closed symbols indicate the dynamics for the low $k_{TTA}$ of the host:guest system. The open symbols (dashed lines) have been calculated with a TTA rate of $k_{TTA} = 5.0 \times 10^{-13}$ cm$^3$ s$^{-1}$.[81]

As shown in Figure 1.10c,d Kasemann *et al.* calculated, singlet and triplet population of 40 nm thick 2 wt.% 4-dicyanomethylene-2-methyl-6-p-dimethylaminostyryl-4*H*-pyran (DCM) in tris(8-hydroxyquinoline) ($Alq_3$) guest:host film under electrical excitation at 1 kA cm$^{-2}$. Figure 1.10c shows the population when the electron mobility is $1\times10^{-5}$ cm$^2$ V$^{-1}$ s$^{-1}$ and Figure 1.10d shows the population when the electron mobility is $2\times10^{-4}$ cm$^2$ V$^{-1}$ s$^{-1}$. The results clearly showing the population of triplets are increasing with excitation time, while singlet exciton population is decreasing, and the behavior is more severe under high current mobilities[81–83]. Thus, these accumulated triplets can hamper light amplification by singlet excitons even without

annihilation processes. Moreover, the open symbols with dashed lines in Figure 1.10d shows when a triplet-triplet annihilation (TTA) mechanism involved in, the population of singlets could increase while decreasing the population of triplets[81].

The accumulated triplets will induce two major exciton quenching processes, i.e., STA and TTA. Note that quenching of singlet excitons by other singlet excitons [singlet-singlet annihilation (SSA)], quenching of singlet excitons by polarons (SPA), Joule heating [singlet-heat quenching (SHQ)][84], electric field induced quenching are other exciton quenching mechanisms of singlets which are not induced by triplet excitons.

Here, I explain STA and TTA processes in more detail. In the event of TTA, the collision of two excited state triplets ($T_1$) in the absence of a magnetic field may result in one ground state singlet molecule and nine equally probable statistical outcomes of excited state molecules, one of which is singlet ($S_n$), three are triplets ($T_n$) and five are quintets ($Q_n$) which can represent by following Eq. 1.5;

$$T_1 + T_1 \rightarrow S_0 + \frac{1}{9}S_n + \frac{3}{9}T_n + \frac{5}{9}Q_n \qquad \text{(Eq. 1.5)}$$

Here, the event of TTA requires close proximity of two triplet excitons by high triplet exciton density, thus this is a bimolecular Dexter energy transfer (DET) process. TTA is relatively significant at high current densities of electrical excitation due to 75 % triplet formation efficiency. Low doping ratio of triplet accumulating molecules in a blend can increase the distance between triplet excitons, thus it decreases the DET efficiency for TTA. Interestingly, a TTA process can yields singlet excitons after the annihilation process, leading to the enhancement of EL efficiency in case of fluorescence emitters[85–90].

On the other hand, quenching of singlets by long-lived triplets, which is known as STA (Figure 1.11a), is the most serious triplet induced quenching process for organic lasers[52,81,91–95]. When the singlet emission ($S_1$-$S_0$ energy gap) of a donor molecule is

approximately equal to the triplet absorption ($T_1$-$T_n$ energy gap) of an accepter molecule, the STA takes place (Figure 1.11a). Since this is a Förster resonance energy transfer (FRET) process, a long-range energy transfer is possible at STA. Moreover, since triplet population is three times larger than singlet population at electrical excitation, STA is much more severe and detrimental. Thus, as explained in section 1.2.4, the major cause for the efficiency rolloff in OLEDs is STA[37,52,55,66].

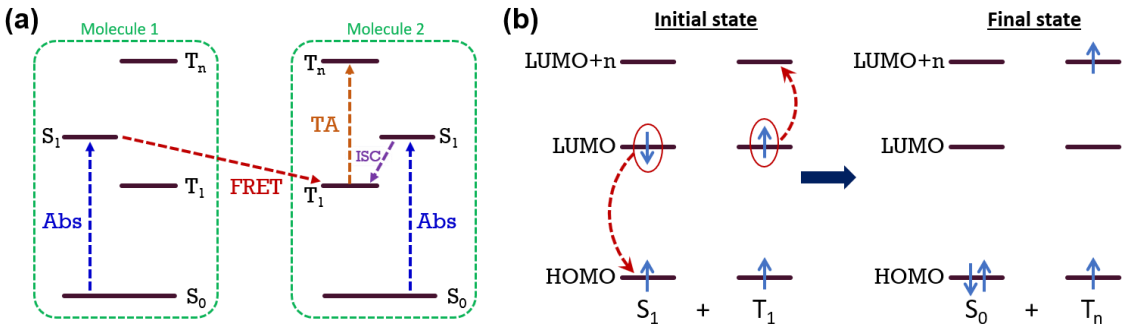


**Figure 1.11.** Schematic exciton energy transfer mechanism of STA; (a) Energy level diagram, (b) molecular orbital diagram. Abs, ISC, FRET and TA stands for steady state absorption, intersystem crossing, Förster resonance energy transfer and triplet absorption respectively.

### 1.3.2 Short pulse excitation to overcome STA

Since triplet lifetime is longer than singlet lifetime, using long pulse excitation increases the population density of triplets (Figure 1.10). Therefore, one way to suppress the triplet accumulation is to use optically and electrically short-pulse excitation (nanoseconds or lower) with longer rest time (low pulse frequency). Thus, shorter pulse excitation leads smaller triplet population and those triplets relax to a ground state after longer relaxation time. In addition, this short-pulsed excitation helps to dissipate joule heat and thereby increase device stability. However, there are plenty of organic materials that show lasing under a short-pulsed optical excitation but do not show lasing under long pulse or CW optical excitation.

### 1.3.3 Spectral separation to overcome STA

One way to suppress the STA is to design and synthesis organic emitters, which have no spectral overlap between the singlet emission ($S_1$-$S_0$) and the triplet absorption ($T_1$-$T_n$). The FRET efficiency between singlet and triplet excitons will be minimized (Figure 1.11a). Therefore, as depicted in Figure 1.12, strong STA can be observed when there is the large spectral overlap. There are few molecules such as 4-4′-bis[(*N*-carbazole)styryl]biphenyl (BSBCz)[36,53,96,97] and ter(9,9'-spirobifluorene) (TSBF)[55] which satisfy this condition[52,92,98]. Moreover, even though no spectral overlap could completely overcome STA, it is hard to avoid triplet accumulation on emitter molecules specially under CW operation and electrical excitation.

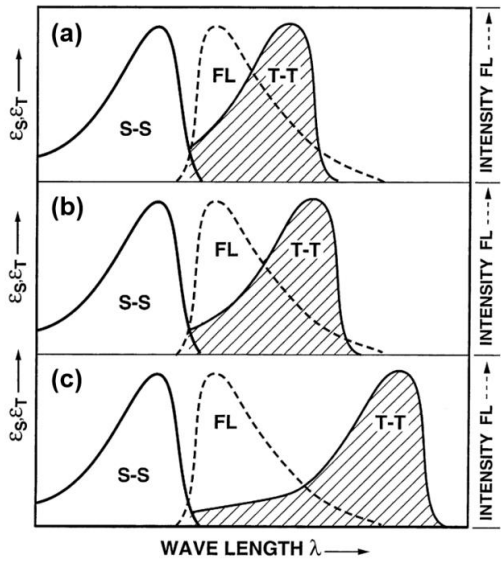


**Figure 1.12.** Depicts three representative cases of an organic compounds that exhibits (A) strong (B) moderate and (C) small FRET efficiencies of STA. S-S denotes steady state singlet-singlet absorption, FL denotes fluorescence emission from $S_1$ to $S_0$ and T-T denotes excited state triplet-triplet absorption from $T_1$ to $T_n$.[52]

### 1.3.4 Triplet management to overcome STA

Another intrinsic way to manage triplet excitons can be realized by blending organic emitters with triplet manager molecules[93,99,100]. In this case, it is important to consider the spectral overlap of the singlet emission of an emitter molecule and the triplet

excited-state absorption of a scavenger molecule, because this spectral overlap causes the STA between them. To have efficient triplet scavenging, the triplet manager molecule should meet a set of important requirements[101];

1) Triplet manager should be able to accept a triplet exciton from the emitter molecules, implying that the triplet energy level of a triplet manager molecule should be low enough than that of the emitter.
2) At the same time, the singlet energy level of a triplet manager should be high enough to prevent quenching of singlet excitons of the emitter molecules. This implies that the $S_1$–$T_1$ splitting for the triplet manager should be enough large.
3) Triplet manager should possess a reasonably short intrinsic triplet lifetime to quickly deplete the triplet population so that triplet accumulation would not happen.
4) It should have the spectral separation between the emission region and the excited state absorption, i.e., triplet absorption (TA), polaron absorption (PA) of triplet managers.
5) Triplet manager should not enhance ISC of the emitter molecules to prevent converting singlets into triplet excitons. This criterion imposes certain limitations for employing compounds containing heavy atoms (such as metal–organic complexes) as triplet managers[101,102].

Mostly, triplet oxygen[65,100], perylene derivatives[103], cyclooctatetraene (COT)[101,104], and anthracene derivatives[101,105–107] have been used as triplet managers in previous studies. However, in most of these scenarios, the triplet managers are either in gas phase or in solid-state with high crystallinity, which implies that those cannot be used as an efficient host material. Therefore, finding such materials, which possess requirements for a host as well as requirements for a triplet scavenger, is rather hard[101].

In general, a good host molecule should possess the following set of important requirements[108–110];

1) Effective spectral overlap between the emission spectra of a host molecule and the absorption spectra of an emitter molecule, thereby having efficient forward FRET.
2) Bipolar charge transport properties for use in electrical operation.
3) Crystallization should be minimum so that the charge accumulation and light scattering at grain boundaries can be minimized.
4) It should not form degenerated energy states at the aggregation of host molecules such as excimer or dimer states.
5) It should not form an exciplex with an emitter molecule to avoid any degenerated energy states.
6) It should have proper matching of highest occupied molecular orbital (HOMO) and lowest unoccupied molecular orbital (LUMO) levels compatible with an emitter molecule and electrodes for use in electrical operation.

## 1.4 Aim and outline of this thesis

Although it is obvious that organic lasers have many advantages as a potential alternative[58] to inorganic semiconductor lasers, organic lasers have to overcome several issues to realize high performance CW lasing[24,111–114] and current injection organic lasers[48,50,53]. Major obstacles of organic laser materials for enhancing laser device performance originate from the accumulation of triplet excitons which lead to various deactivation effects such as STA.

In this thesis, instead of designing a molecule with all requirements for a triplet scavenger and for a host molecule, I selected a fluorescent material having a small singlet-triplet energy gap ($\Delta E_{ST}$). Hence, the triplets of a guest emitter are easily transferred to a

host material, realizing efficient removal of triplets from emitter molecules. In **Chapter 2**, the proposed strategy is proved by incorporating a novel fluorescent emitter having a rather small $\Delta E_{ST}$ into a host layer having efficient triplet scavenging capability. Then, the proposed guest-host matrix is embedded into a DFB architecture to demonstrate optically driven CW lasers. Based on the promising result under optical excitation, **Chapter 3** demonstrate the suppression of efficiency roll-off at high current densities and long-pulse excitation in the OLED. **Chapter 4** summarizes this thesis and discuss future perspectives. Finally, fundamentals of DFB lasers are discussed in **Appendix A**, to clarify optical physics behind DFB optical resonators, and its usage for integrated organic lasers.

**References**


[1] A. Einstein, *Physiol Z* **1917**, *18*, 121.

[2] M. Rose and H. Hogan, *A History of the Laser : 1960 – 2019*, Available at: https://www.photonics.com/Articles/A_History_of_the_Laser_1960_-_2019/a42279.

[3] A. L. Schawlow and C. H. Townes, *Phys. Rev.* **1958**, *112*, 1940.

[4] T. H. Maiman, *Nature* **1960**, *187*, 493.

[5] R. N. Hall, G. E. Fenner, J. D. Kingsley, T. J. Soltys, R. O. Carlson, *Phys. Rev. Lett.* **1962**, *9*, 366.

[6] On the shoulders of giants. *Photonics media* **2019**, Available at: https://www.photonics.com/Article.aspx?AID=42280.

[7] P. P. Sorokin, J. R. Lankard, *IBM J. Res. Dev.* **1966**, *10*, 162.

[8] W. F. Coleman, *J. Chem. Educ.* **1982**, *59*, 441.

[9] R. M. Herd, J. S. Dover, K. A. Arndt, *Dermatol. Clin.* **1997**, *15*, 355.

[10] R. Dabu, *Crystals* **2019**, *9*, 347.

[11] R. Goyena and A. Fallis, *Hand book of organic materials for optical and (opto)electronic devices*; Woodhead Publishing Series in Electronic and Optical Materials:, 2013; Vol. 39, pp. 17.

[12] A. Köhler, H. Bässler, *Mater. Sci. Eng. R Reports* **2009**, *66*, 71.

[13] Z. Li, H. Meng, *Organic Light Emitting Materials and Devices*; Taylor & Francis Group, 2007; pp. 12.

[14] M. A. Baldo, D. F. O'Brien, M. E. Thompson, S. R. Forrest, *Phys. Rev. B - Condens. Matter Mater. Phys.* **1999**, *60*, 14422.

[15] M. Anni, S. Lattante, *Organic Lasers Fundamentals, Developments and Application*; Pan Stanford Publishing Pte. Ltd., 2018; pp. 6.

[16] Wikimedia Commons contributors, File:Vibration-fluor-abs.png. *Wikimedia Commons, Free media Repos,* DOI:361032222.

[17] W. T. Silfvast, Fundamentals of Photonics; Lasers (Module 5 of 10). *Mater. Dev. under Proj. STEP (Scientific Technol. Educ. Photonics) by Univ. Connect. CORD* **2003;** pp. 5.

[18] H. Ye, Development of deep-red and near-infrared organic luminescent materials and their applications in organic light-emitting diodes and continuous-wave organic semiconductor lasers. Doctoral thesis, Graduate School of Engineering Kyushu University, 2019.

[19] H. Xia, C. Hu, T. Chen, D. Hu, M. Zhang, K. Xie, *Polymers (Basel)* **2019**, *11(3)*,433.

[20] J. H. Kim, M. Inoue, L. Zhao, T. Komino, S. Seo, J. C. Ribierre, C. Adachi, *Appl. Phys. Lett.* **2015**, *106*, 053302.

[21] I. D. W. Samuel, G. A. Turnbull, *Mater. Today* **2004**, *7(9)*, 28.

[22] O. Mhibik, T. Leang, A. Siove, S. Forget, S. Chénais, *Appl. Phys. Lett.* **2013**, *102*, 041112.

[23] F. P. Schäfer, W. Schmidt, J. Volze, *Appl. Phys. Lett.* **1966**, *9*, 306.

[24] O. G. Peterson, S. A. Tuccio, B. B. Snavely, *Appl. Phys. Lett.* **1970**, *17*, 245.

[25] D. Strickland, G. Mourou, *Opt. Commun.* **1985**, *56*, 219.

[26] B. H. Soffer, B. B. McFarland, *Appl. Phys. Lett.* **1967**, *10*, 266.

[27] I. D. W. Samuel, G. A. Turnbull, *Chem. Rev.* **2007**, *107*, 1272.

[28] M. A. Díaz-García, F. Hide, B. J. Schwartz, M. D. McGehee, M. R. Andersson, A. J. Heeger, *Appl. Phys. Lett.* **1997**, *70*, 3191.

[29] A. J. C. Kuehne, M. C. Gather, *Chem. Rev.* **2016**, *116*, 12823.

[30] N. Tessler, G. J. Denton, R. H. Friend, *Nature* **1996**, *382*, 695.

[31] S. Chénais, S. Forget, *Polym. Int.* **2012**, *61*, 390.

[32] T. Rabe, K. Gerlach, T. Riedl, H. H. Johannes, W. Kowalsky, J. Niederhofer, W. Gries, J. Wang, T. Weimann, P. Hinze, F. Galbrecht, U. Scherf, *Appl. Phys. Lett.* **2006**, *89*, 87.

[33] Y. Yang, G. A. Turnbull, I. D. W. Samuel, *Appl. Phys. Lett.* **2008**, *92*, 92.

[34] F. J. Duarte, L. S. Liao, K. M. Vaeth, *Opt. Lett.* **2005**, *30*, 3072.

[35] A. S. D. Sandanayaka, L. Zhao, D. Pitrat, J. C. Mulatier, T. Matsushima, C. Andraud, J. H. Kim, J. C. Ribierre, C. Adachi, *Appl. Phys. Lett.* **2016**, *108*, 223301.

[36] A. S. D. Sandanayaka, T. Matsushima, F. Bencheikh, K. Yoshida, M. Inoue, T. Fujihara, K. Goushi, J. C. Ribierre, C. Adachi, *Sci. Adv.* **2017**, *3(4)*, e1602570.

[37] A. S. D. Sandanayaka, K. Yoshida, M. Inoue, C. Qin, K. Goushi, J. C. Ribierre, T. Matsushima, C. Adachi, *Adv. Opt. Mater.* **2016**, *4(6)*, 834.

[38] M. Pope, H. P. Kallmann, P. Magnante, *J. Chem. Phys.* **1963**, *38*, 2042.

[39] C. W. Tang, S. A. Vanslyke, *Appl. Phys. Lett.* **1987**, *51*, 913.

[40] C. Adachi, S. Tokito, T. Tsutsui, S. Saito, *Jpn. J. Appl. Phys.* **1988**, *27*, 269.

[41] M. A. Baldo, D. F. O'Brien, Y. You, A. Shoustikov, S. Sibley, M. E. Thompson, S. R. Forrest, *Nature* **1998**, *395*, 151.

[42] C. Adachi, M. A. Baldo, M. E. Thompson, S. R. Forrest, *J. Appl. Phys.* **2001**, *90*, 5048.

[43] A. Endo, M. Ogasawara, A. Takahashi, D. Yokoyama, Y. Kato, C. Adachi, *Adv. Mater.* **2009**, *21*, 4802.

[44] H. Uoyama, K. Goushi, K. Shizu, H. Nomura, C. Adachi, *Nature* **2012**, *492*, 234.

[45] F. B. Dias, T. J. Penfold, A. P. Monkman, *Methods Appl. Fluoresc.* **2017**, *5*, 012001.

[46] H. Nakanotani, K. Masui, J. Nishide, T. Shibata, C. Adachi, *Sci. Rep.* **2013**, *3*, 2127.

[47] H. Nakanotani, T. Oyamada, Y. Kawamura, H. Sasabe, C. Adachi, *Japanese J. Appl. Physics, Part 1 Regul. Pap. Short Notes Rev. Pap.* **2005**, *44*, 3659.

[48] M. A. Baldo, R. J. Holmes, S. R. Forrest, *Phys. Rev. B - Condens. Matter Mater. Phys.* **2002**, *66*, 353211.

[49] S. Z. Bisri, T. Takenobu, Y. Iwasa, *J. Mater. Chem. C* **2014**, *2*, 2827.

[50] M. Chakaroun, A. Coens, N. Fabre, F. Gourdon, J. Solard, A. Fischer, A. Boudrioua, C. C. Lee, *Opt. Express* **2011**, *19(2)*, 493.

[51] F. J. Duarte, K. M. Vaeth, Chapter 11; Electrically-pumped organic semiconductor laser emission, *Organic Lasers and Organic Photonics*; IOP Publishing, 2018; pp. 2053-2563.

[52] T. G. Pavlopoulos, *Prog. Quantum Electron.* **2002**, *26*, 193.

[53] A. S. D. Sandanayaka, T. Matsushima, F. Bencheikh, S. Terakawa, W. J. Potscavage, C. Qin, T. Fujihara, K. Goushi, J. C. Ribierre, C. Adachi, *Appl. Phys. Express* **2019**, *12*, 061010.

[54] J. Lin, Y. Hu, Y. Lv, X. Guo, X. Liu, *Sci. Bull.* **2017**, *62*, 1637.

[55] M. Inoue, T. Matsushima, C. Adachi, *Appl. Phys. Lett.* **2016**, *108*, 133302.

[56] D. H. Kim, A. S. D. Sandanayaka, L. Zhao, D. Pitrat, J. C. Mulatier, T. Matsushima, C. Andraud, J. C. Ribierre, C. Adachi, *Appl. Phys. Lett.* **2017**, *110*, 023303.

[57] H. Nakanotani, S. Akiyama, D. Ohnishi, M. Moriwake, M. Yahiro, T. Yoshihara, S. Tobita, C. Adachi, *Adv. Funct. Mater.* **2007**, *17*, 2328.

[58] V. T. N. Mai, A. Shukla, M. Mamada, S. Maedera, P. E. Shaw, J. Sobus, I. Allison, C. Adachi, E. B. Namdas, S. C. Lo, *ACS Photonics* **2018**, *5*, 4447.

[59] A. D'Aléo, M. H. Sazzad, D. H. Kim, E. Y. Choi, J. W. Wu, G. Canard, F. Fages, J.-C. Ribierre, C. Adachi, *Chem. Commun.* **2017**, *53*, 7003.

[60] H. Nakanotani, T. Furukawa, T. Hosokai, T. Hatakeyama, C. Adachi, *Adv. Opt. Mater.* **2017**, *5(12)*, 1700051.

[61] T. Matsushima, S. Yoshida, K. Inada, Y. Esaki, T. Fukunaga, H. Mieno, N.

Nakamura, F. Bencheikh, M. R. Leyden, R. Komatsu, C. Qin, A. S. D. Sandanayaka, C. Adachi, *Adv. Funct. Mater.* **2019**, *29*, 1807148.

[62] Y. Oyama, M. Mamada, A. Shukla, E. G. Moore, S.-C. Lo, E. B. Namdas, C. Adachi, *ACS Mater. Lett.* **2020**, *2*, 161.

[63] D. Yokoyama, A. Sakaguchi, M. Suzuki, C. Adachi, *Org. Electron.* **2009**, *10(1)*, 127.

[64] F. Bencheikh, A. S. D. Sandanayaka, T. Fukunaga, T. Matsushima, C. Adachi, **2019**, *126*, 185501.

[65] L. Zhao, M. Inoue, K. Yoshida, A. S. D. Sandanayaka, J. H. Kim, J. C. Ribierre, C. Adachi, *IEEE J. Sel. Top. Quantum Electron.* **2016**, *22*, 26.

[66] C. Murawski, K. Leo, M. C. Gather, *Adv. Mater.* **2013**, *25*, 6801.

[67] C. Poriel, J. Rault-Berthelot, *Adv. Funct. Mater.* **2020**, *30(17)*, 1910040.

[68] Z. Wu, Z. Yang, K. Xue, C. Fei, F. Wang, M. Yan, H. Zhang, D. Ma, W. Huang, *RSC Adv.* **2018**, *8*, 11255.

[69] N. B. Kotadiya, P. W. M. Blom, G. J. A. H. Wetzelaer, *Nat. Photonics* **2019**, *13*, 765.

[70] X. Kai, Y. Minnan, P. Fei, T. Mengying, P. Xudong, Z. Hongmei, *Acta Phys. - Chim. Sin.* **2019**, *35*, 896.

[71] I. D. W. Samuel, E. B. Namdas, G. A. Turnbull, *Nat. Photonics* **2009**, *3*, 546.

[72] J. Zhao, Y. Yan, Z. Gao, Y. Du, H. Dong, J. Yao, Y. S. Zhao, *Nat. Commun.* **2019**, *10*, 870.

[73] A. Rose, Z. Zhu, C. F. Madigan, T. M. Swager, V. Bulović, *Nature* **2005**, *434*, 876.

[74] D. A. Vithanage, P. P. Manousiadis, M. T. Sajjad, S. Rajbhandari, H. Chun, C. Orofino, D. Cortizo-Lacalle, A. L. Kanibolotsky, G. Faulkner, N. J. Findlay, D. C. O'Brien, P. J. Skabara, I. D. W. Samuel, G. A. Turnbull, *Appl. Phys. Lett.* **2016**, *109*, 013302.

[75] J. Clark, G. Lanzani, *Nat. Photonics* **2010**, *4*, 438.

[76] J. Hahn, H. Kim, Y. Lim, G. Park, B. Lee, *Opt. Express* **2008**, *16*, 12379.

[77] M. Guillaumee, S. P. Vahdati, E. Tremblay, A. Mader, G. Bernasconi, V. J. Cadarso, J. Grossenbacher, J. Brugger, R. Sprague, C. Moser, *IEEE/OSA J. Disp. Technol.* **2014**, *10*, 444.

[78] J. Park, K. R. Lee, Y. K. Park, *Nat. Commun.* **2019**, *10*, 1304.

[79] W. Wan, W. Qiao, D. Pu, R. Li, C. Wang, Y. Hu, H. Duan, L. J. Guo, L. Chen, *iScience* **2020**, *23*, 100773.

[80] M. Goossens, A. Ruseckas, G. A. Turnbull, I. D. W. Samuel, *Appl. Phys. Lett.* **2004**, *85*, 31.

[81] D. Kasemann, R. Brückner, H. Fröb, K. Leo, *Phys. Rev. B* **2011**, *84*, 115208.

[82] T. Hori, K. Totani, S. Hirata, T. Watanabe, *Chem. Phys. Lett.* **2018**, *704*, 5.

[83] S. Hirata, M. Vacha, *Adv. Opt. Mater.* **2016**, *4*, 297.

[84] K. Yoshida, T. Matsushima, Y. Shiihara, H. Kuwae, J. Mizuno, C. Adachi, *J. Appl. Phys.* **2017**, *121*.

[85] N. Chitraningrum, T. Y. Chu, P. T. Huang, T. C. Wen, T. F. Guo, *Org. Electron.* **2018**, *62*, 505.

[86] A. S. Gertsen, M. Koerstz, K. V. Mikkelsen, *Phys. Chem. Chem. Phys.* **2018**, *20*, 12182.

[87] R. R. Islangulov, D. V. Kozlov, F. N. Castellano, *Chem. Commun.* **2005**, *1*, 3776.

[88] J. E. Auckett, Y. Y. Chen, T. Khoury, R. G. C. R. Clady, N. J. Ekins-Daukes, M. J. Crossley, T. W. Schmidt, *J. Phys. Conf. Ser.* **2009**, *185*, 6.

[89] D. Y. Kondakov, *Philos. Trans. R. Soc. A Math. Phys. Eng. Sci.* **2015**, *373*.

[90] J. Saltiel, G. R. Marchand, W. K. Smothers, S. A. Stout, J. L. Charlton, *J. Am. Chem. Soc.* **1981**, *103*, 7159.

[91] Y. Zhang, M. Whited, M. E. Thompson, S. R. Forrest, *Chem. Phys. Lett.* **2010**, *495*, 161.

[92] M. Lehnhardt, T. Riedl, T. Weimann, W. Kowalsky, *Phys. Rev. B* **2010**, *81*, 165206.

[93] Y. Zhang, S. R. Forrest, *Phys. Rev. B* **2011**, *84*, 241301.

[94] E. B. Namdas, A. Ruseckas, I. D. W. Samuel, S. C. Lo, P. L. Burn, *Appl. Phys. Lett.* **2005**, *86*, 091104.

[95] A. Dey, N. Chandrasekaran, D. Chakraborty, P. Johari, C. R. McNeill, A. Rao, D. Kabra, *npj Flex Electron.* **2018**, *2*, 28.

[96] H. Nakanotani, C. Adachi, S. Watanabe, R. Katoh, *Appl. Phys. Lett.* **2007**, *90*, 4.

[97] T. Aimono, Y. Kawamura, K. Goushi, H. Yamamoto, H. Sasabe, C. Adachi, *Appl. Phys. Lett.* **2005**, *86*, 071110.

[98] C. Xiang, X. Fu, W. Wei, R. Liu, Y. Zhang, V. Balema, B. Nelson, F. So, *Adv. Funct. Mater.* **2016**, *26*, 1463.

[99] A. Salehi, C. Dong, D. H. Shin, L. Zhu, C. Papa, A. Thy Bui, F. N. Castellano, F. So, *Nat. Commun.* **2019**, *10*, 2305.

[100] M. Inoue, T. Matsushima, H. Nakanotani, C. Adachi, *Chem. Phys. Lett.* **2015**, *624*, 43.

[101] S. Schols, A. Kadashchuk, P. Heremans, A. Helfer, U. Scherf, *ChemPhysChem* **2009**, *10*, 1071.

[102] A. Dey, D. Kabra, *J. Phys. Chem. A* **2019**, *123*, 4858.

[103] M. Ahmad, M. D. Rahn, T. A. King, *Appl. Opt.* **1999**, *38*, 6337.

[104] T. N. Das, K. I. Priyadarsini, *J. Chem. Soc. Faraday Trans.* **1994**, *90*, 963.

[105] S. Schols, A. Kadashchuk, P. Heremans, A. Helfer, U. Scherf, In *Organic Light Emitting Materials and Devices XIII*; So, F.; Adachi, C., Eds.; SPIE, 2009; Vol. 7415, pp. 43.

[106] Y. Zhang, M. Slootsky, S. R. Forrest, in *Conference on Lasers and Electro-Optics 2012, OSA Technical Digest,* **2012**, paper CW1L.6.

[107] Y. J. Pu, G. Nakata, F. Satoh, H. Sasabe, D. Yokoyama, J. Kido, *Adv. Mater.* **2012**, *24*, 1765.

[108] X. Ren, J. Li, R. J. Holmes, P. I. Djurovich, S. R. Forrest, M. E. Thompson, *Chem. Mater.* **2004**, *16*, 4743.

[109] C. Han, Y. Zhao, H. Xu, J. Chen, Z. Deng, D. Ma, Q. Li, P. Yan, *Chem. - A Eur. J.* **2011**, *17*, 5800.

[110] S. Gong, X. He, Y. Chen, Z. Jiang, C. Zhong, D. Ma, J. Qin, C. Yang, *J. Mater. Chem.* **2012**, *22*, 2894.

[111] T. Rabe, K. Gerlach, T. Riedl, H. H. Johannes, W. Kowalsky, J. Niederhofer, W. Gries, J. Wang, T. Weimann, P. Hinze, F. Galbrecht, U. Scherf, *Appl. Phys. Lett.* **2006**, *89*, 081115.

[112] R. Bornemann, U. Lemmer, E. Thiel, *Opt. Lett.* **2006**, *31*, 1669.

[113] P. Brenner, O. Bar-On, M. Jakoby, I. Allegro, B. S. Richards, U. W. Paetzold, I. A. Howard, J. Scheuer, U. Lemmer, *Nat. Commun.* **2019**, *10*, 988.

[114] T. Riedl, In *2015 European Conference on Lasers and Electro-Optics - European Quantum Electronics Conference*, **2015,** paper CE_8_1.

# Chapter 2

## An organic laser dye having a small singlet-triplet energy gap makes the selection of a host material easier

## 2.1 Introduction

In this Chapter, I proposed and proved an ideal lasing system that induces efficient triplet scavenging by developing a novel laser material having a rather small singlet-triplet energy gap ($\Delta E_{ST}$) which promotes efficient triplet energy transfer from a guest to a host while the single energy transfer only occurs from a host to a guest. Here, I synthesized a promising lasing molecule of 2,6-dicyano-1,1-diphenyl-$\lambda^5\sigma^4$-phosphinine (DCNP) based on the synthesis route reported by N. Hashimoto *et al.*[1]. I used DCNP as a laser dye and BSBCz as a triplet scavenging host to realize a stable green organic laser. Since the triplet exciton formed on DCNP is easily transferred to BSBCz, I was able to eliminate the triplet-induced losses. Here, the excited state absorption spectrum of BSBCz[2–4] does not seriously overlap with the laser emission spectrum of DCNP. In addition, BSBCz as a triplet-scavenging-host molecule fulfills most of the requirements described in Chapter 1, such as a high $S_1$ than that of the emitter, a low $T_1$ than that of the emitter, faster nonradiative relaxation from the $T_1$, no heavy metals, no serious crystallization, bipolar charge transport characteristics, matching HOMO and LUMO levels, and the capability of vacuum deposition. By taking these advantages, in this Chapter, I realized high performance from an optically pumped laser system based on DCNP-doped BSBCz films.

## 2.2 Experimental

***Synthesis and molecular characterization of DCNP***

Detail methods and explanation are given in section 2.3.1.

***Organic film fabrication***

DCNP, BSBCz neat films and 0.5, 1, 2, 4, 8 wt.%-DCNP doped BSBCz films each with a thickness of 200 nm were fabricated on clean fused quartz substrates by vacuum deposition under a pressure of $2\times10^{-4}$ Pa. The deposition rate was set at

0.25 nm $s^{-1}$. These films were transferred directly into a nitrogen-filled glove box without exposure to air and then encapsulated using a sapphire plate and transparent fluoropolymer CYTOP® as reported previously[3]. PMMA films doped with DCNP at 0.1, 0.3, 0.5, 1, 2, 3, 4, 5, 6, and 8 wt.%, each with a thickness of approximately 200 nm, were also prepared using a spin-coating method for comparison.

***Photo-physical characterization***

Steady-state absorption spectra, PL spectra and PL quantum yields of the aforementioned films were measured using a double beam absorption spectrometer (Lambda 950, Perkin Elmer), a spectro- fluorometer (FP 8600 by JASCO) and an absolute PL quantum yield measurement system (Quantaurus-QY plus, Hamamatsu Photonics), respectively. Time-resolved PL decays were measured using a transient emission spectrometry setup, in which the excitation source was; Nd:YAG/YVO laser (EKSPLA PL-2250, third harmonic wave generation) with an excitation wavelength of 355 nm and pulse duration of 30 ps and the detector was a streak camera (C10910-01, Hamamatsu Photonics). Excited-state absorption spectra were measured using two separate transient absorption setups designed for ns and μs time scales. The measurement with the ns-time scale was taken using the same excitation laser source used for transient emission measurement by coupled with a Xe lamp and streak camera (C7700, Hamamatsu Photonics). The measurement at the μs time scale was taken using third-harmonic-wave laser light from a Nd:YAG laser with a wavelength of 355 nm (Quanta-Ray GCR-130, Spectra-Physics) as the pump light, and pulsed white light from a Xe lamp as the probe light and the streak camera (C7700, Hamamatsu Photonics) as the detector. The ionization energies of BSBCz and 1 wt.%-DCNP:BSBCz films were measured using photoelectron yield spectroscopy (AC-3, Riken Keiki).

***ASE characterization***

200 nm thick films were prepared on quartz substrates. For the ASE

measurements, pulsed excitation light from a $N_2$ laser (KEN-2020, Usho) was focused on the edge of the films in a stripe shaped irradiation area of 0.12×0.32 $cm^2$ using a lens and slit. For the pulsed excitation, an excitation wavelength was 337 nm, pulse width was 0.8 ns, and repetition rate was 20 Hz. The emitted light from the films was collected from the edge of the substrates using a multichannel spectrometer (PMA-12, Hamamatsu Photonics). All the measurements were performed in a nitrogen atmosphere to prevent any degradation resulting from moisture and oxygen. The ASE threshold values were estimated from PL intensity versus excitation power plots, without taking account of transmission losses, i.e., optical density (OD) of the films.

***DFB structure fabrication***

Silicon substrates covered with a thermally grown silicon dioxide layer with a thickness of 1 μm were cleaned by ultrasonication using alkali detergent, pure water, acetone, and isopropanol followed by ultraviolet-ozone treatment. The silicon dioxide surfaces were treated with hexamethyldisilazane by spin coating at 4000 rpm for 15 s and annealed at 120 °C for 120 s. A resist layer with a thickness of around 70 nm was spin-coated on the substrates at 4000 rpm for 30 s from a ZEP520A-7 solution (ZEON Co.) and baked at 180 °C for 240 s. Electron beam lithography was performed to draw grating patterns on the resist layer using a JBX-5500SC system (JEOL) with an optimized dose of 0.1 nC $cm^{-2}$. After the electron beam irradiation, the patterns were developed in a developer solution (ZED-N50, ZEON Co.) at room temperature. The patterned resist layer was used as an etching mask. Then the substrate was plasma-etched with $CHF_3$ using an EIS-200ERT etching system (Elionix). To completely remove the resist layer from the substrate, the substrate was further plasma-etched with $O_2$ using a FA-1EA etching system (SAMCO). The gratings formed on the silicon dioxide surfaces were observed with SEM (SU8000, Hitachi)[3–5].

***Organic laser devices for optical pumping***

To complete the laser devices, 1 wt.%-DCNP:BSBCz blend films with a thickness of 200 nm was deposited on the grating structures by vacuum thermal evaporation under a pressure of $2.0\times10^{-4}$ Pa with a total evaporation rate of 0.25 nm $s^{-1}$. Finally, 0.05 ml of CYTOP® (Asahi Glass Co. Ltd.) was directly spin-coated at 1000 rpm for 30 s onto the DFB laser devices, sandwiched with sapphire lids to seal the top of the laser devices, and dried in a vacuum overnight.

***Laser characterization at short pulsed excitation***

For the characterization of the pulsed organic lasers, pulsed excitation light from a nitrogen gas laser (NL100, $N_2$ laser, Stanford Research System) was focused on a $6.89\times10^{-3}$ $cm^2$ area of the devices through a lens and slit. The excitation wavelength was 337 nm, the pulse width was 3 ns, and the repetition rate was 20 Hz. Excitation intensities were controlled using a set of neutral density filters. For the surface emitter DFB device characterization, the excitation light was incident upon the devices at around 20° with respect to the normal to the device plane. The emitted light was collected normal to the device surface with an optical fiber connected to a multichannel spectrometer (PMA-50, Hamamatsu Photonics) and placed 3 cm away from the device. Excitation intensities were controlled using a set of neutral density filters. Near-field patterns far-field patterns of DFB-OSSL were taken using a laser beam profiler (C9164-01, Hamamatsu Photonics) and (C9664-01G02, Hamamatsu Photonics) respectively.

***CW and long pulse characterization***

CW laser diode, with a maximum power of 25 mW (coherent, OBIS), was used to generate excitation light with an excitation wavelength of 355 nm. In these measurements, excitation pulses were delivered using an acousto-optic modulator (Gooch and Housego) that was triggered with a pulse generator (WF 1974, NF Co.). The excitation light was focused on a $3.52\times10^{-6}$ $cm^2$ area of the devices through a lens and

slit, and the emitted light was collected using a streak scope (C7700, Hamamatsu Photonics) with a time resolution of 100 ps, which was connected with a digital camera (C9300, Hamamatsu Photonics). The emission intensities were recorded using a photomultiplier tube (PMT) (C9525-02, Hamamatsu Photonics) for the measurement of temporal emission profiles. Both the PMT response and the driving square wave signal were monitored with a multichannel oscilloscope (MSO6104A, Agilent Technologies). The same irradiation and detection angles were used for this measurement, as described in short pulsed excitation. The size of the excitation area was carefully checked by using a beam profiler (WinCamD-LCM, DataRay). Excitation power was measured using a laser power meter (OPHIR Optronics Solution Ltd., StarLite 7Z01565).

## 2.3 Results and discussion

### 2.3.1 Synthesis and characterization

A novel organic laser gain material, DCNP, which is a member of $\lambda^5$-phosphinine was synthesized according to a method reported by Naoki Hashimoto *et al.*[1] The Synthesis scheme of DCNP is shown in Figure 2.1.

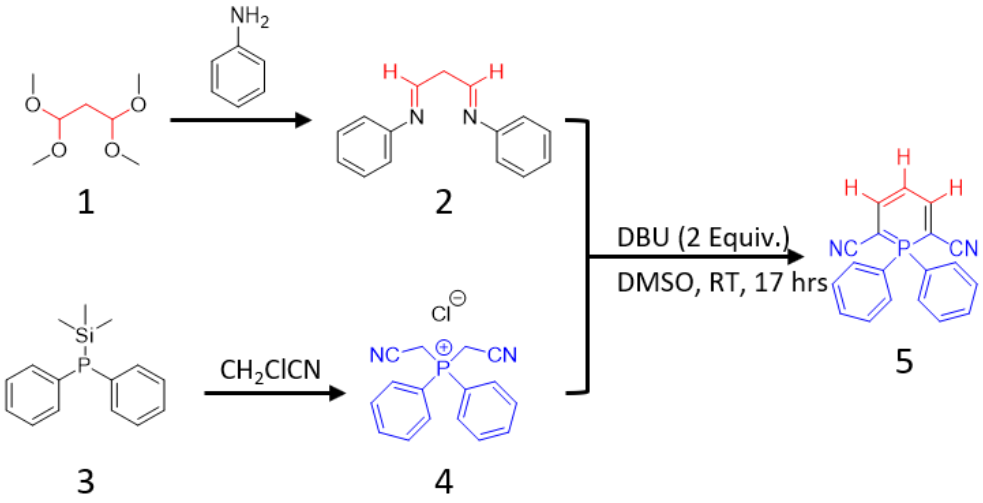


**Figure 2.1.** Synthesis scheme of DCNP

First, *N*,*N*'-diphenyl-1,3-diiminopropane (**2**) was synthesized from 1,1,3,3 tetramethoxypropane (**1**) and aniline in ethanol. Similarly, the phosphonium salt (**4**) was prepared by the treatment of commercially available diphenyltrimethylsilylphosphine (**3**) with an excess of chloroacetonitrile. Then the cyclisation reaction of *N*,*N*'-diphenyl-1,3-diiminopropane (**2**) with phosphonium salt (**4**) in the presence of 1,8-diazabicyclo(5.4.0)undec-7-ene (DBU) gave DCNP (**5**) as a yellow solid in 90 % yield. DCNP was freely soluble in common organic solvents and purified by column chromatography using a mixture of ethylacetate / chloroform / *n*-hexane as the eluent. Further, the purity was performed by a few consecutive vacuum train sublimation steps. The chemical structure was ascertained by nuclear magnetic resonance (NMR) and mass spectrum analysis (Figure 2.2, 2.3 and 2.4).

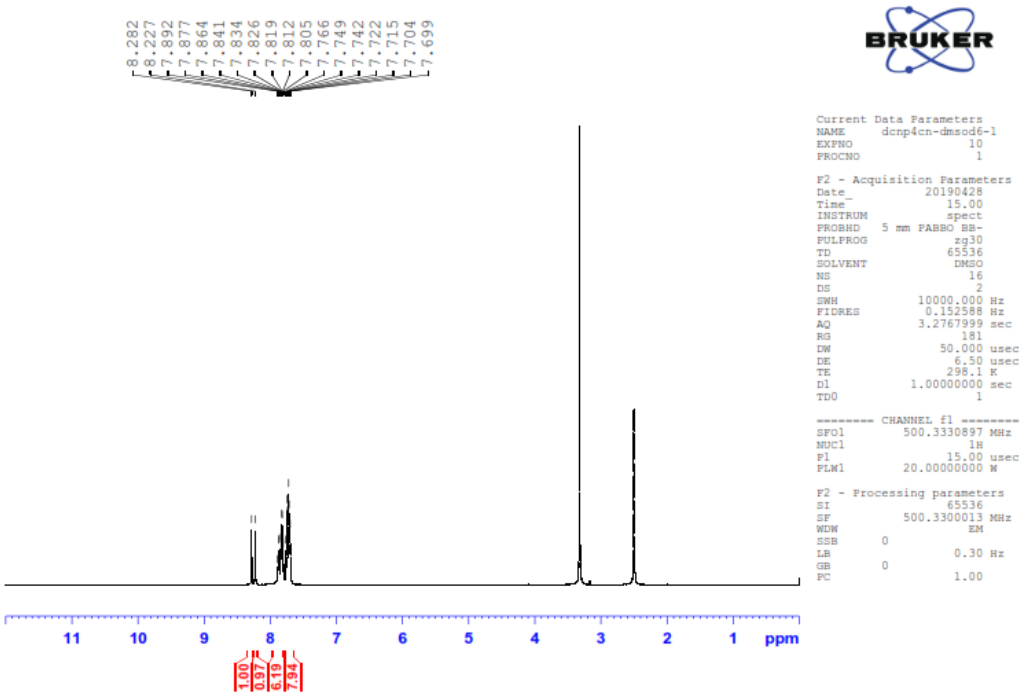


**Figure 2.2.** $^{1}$H-NMR spectra of DCNP

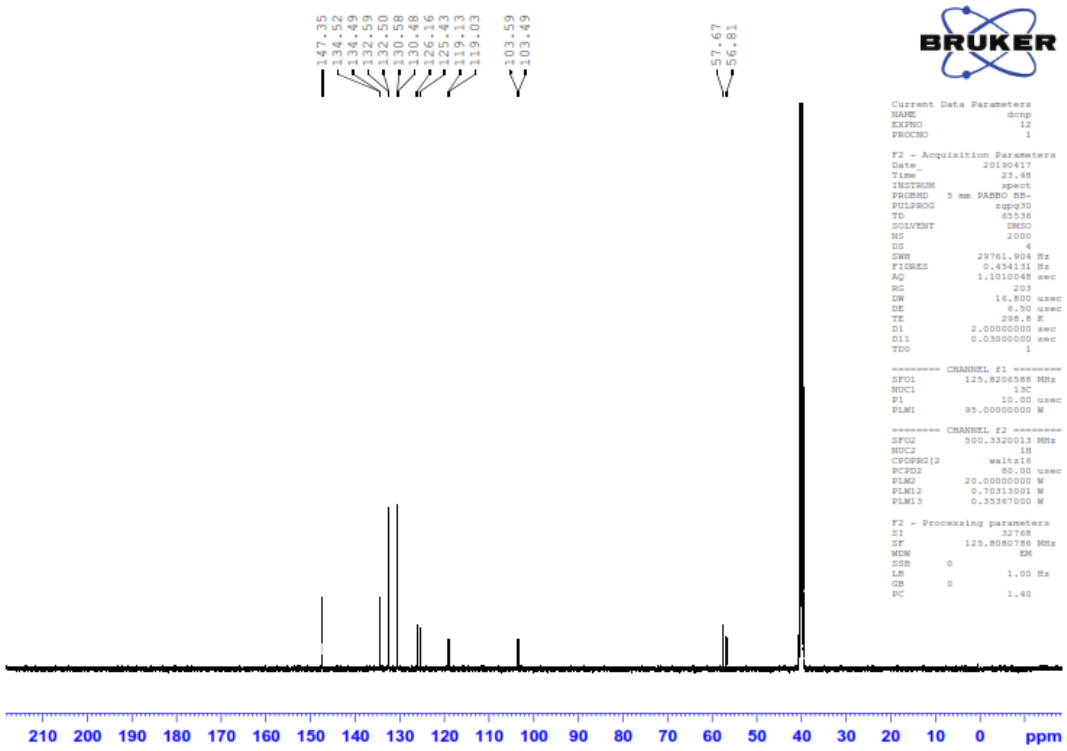


**Figure 2.3.** $^{13}$C-NMR spectra of DCNP

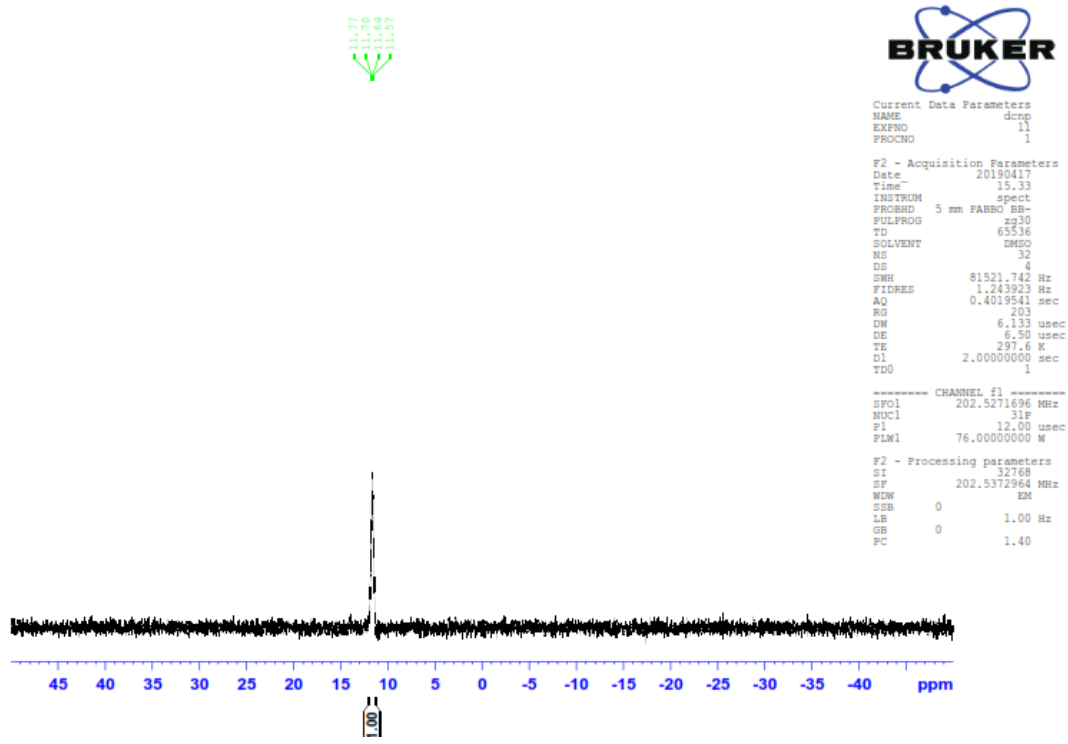


**Figure 2.4.** $^{31}$P-NMR spectra of DCNP

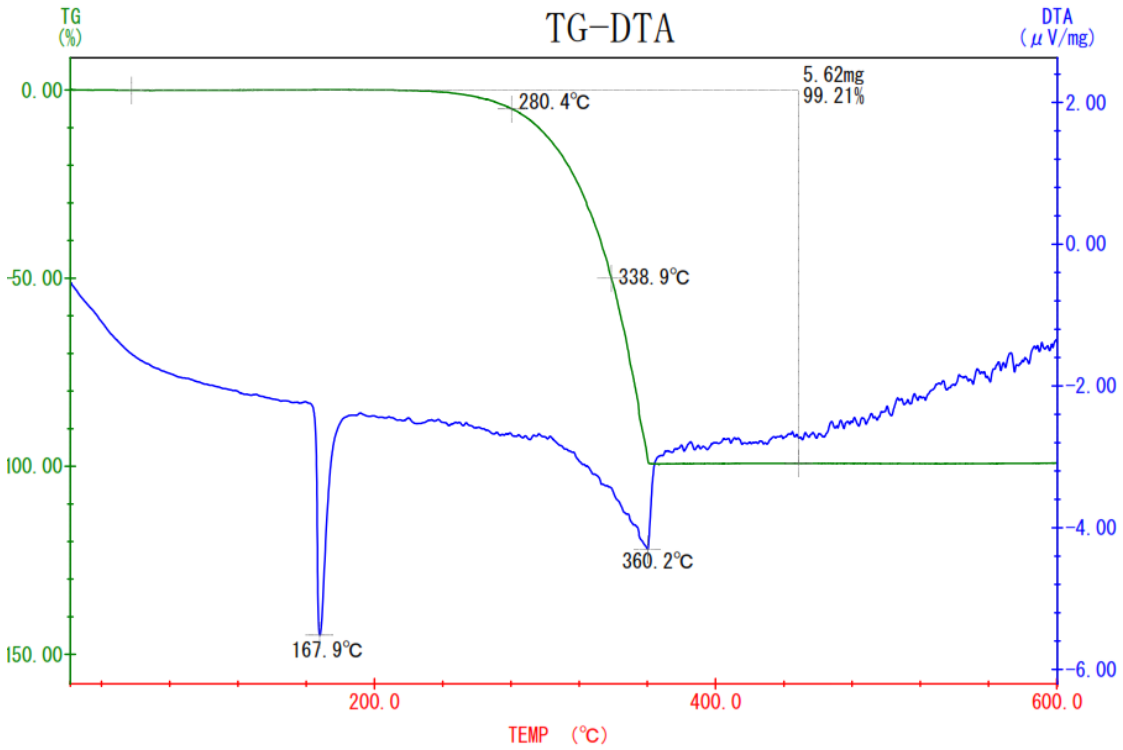


**Figure 2.5.** Thermogravimetric analysis (TGA) and differential thermal analysis (DTA) results of DCNP at ambient pressure.

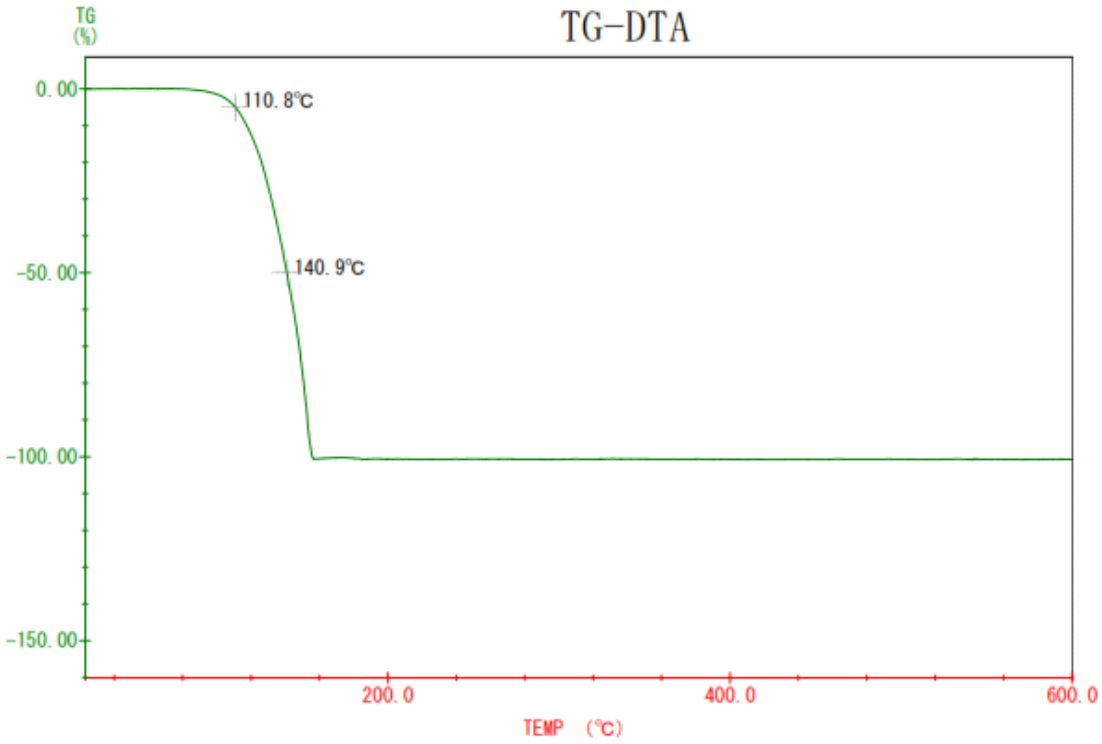


**Figure 2.6.** TGA and DTA results of DCNP at low pressure (1 Pa).

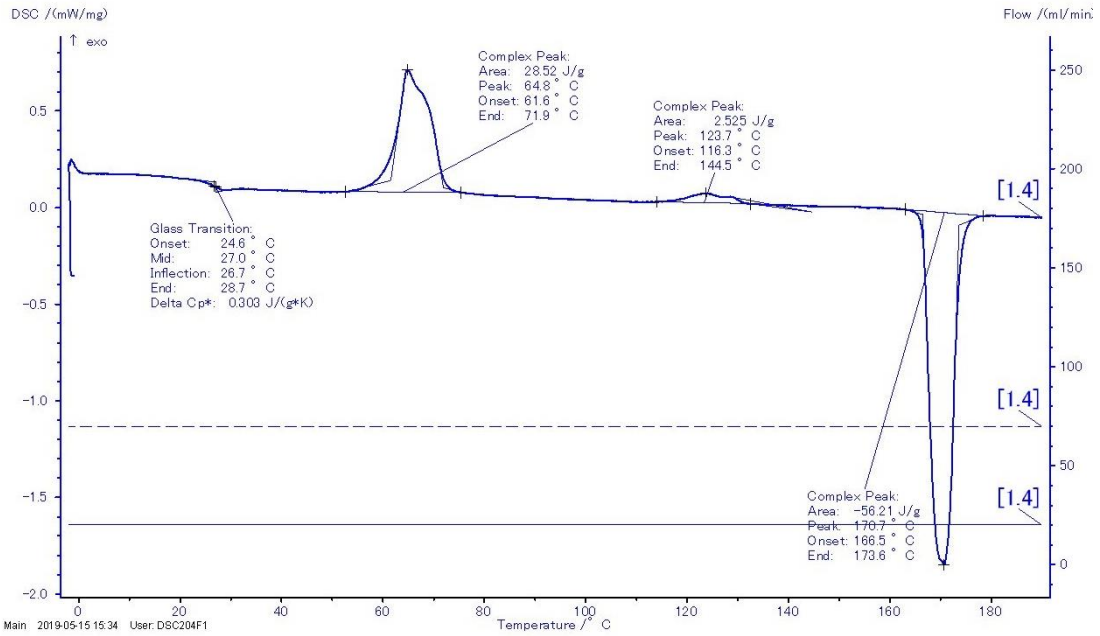


**Figure 2.7.** Differential scanning calorimetry (DSC) results of DCNP.

Even though the DTA revealed an absorption of energy (an endothermic process) at 167.9 ˚C, on the basis of TGA, there is no weight loss occurring at this temperature (Figure 2.5). Thus, the peak at 167.9 ˚C can be assigned for a phase transition of DCNP (the melting point). With further increase of temperature, I observed the boiling point at 280.4 ˚C under ambient pressure. On the other hand, when the pressure was reduced to 1 Pa, the TGA result revealed the weight loss occurred at 110.8 ˚C, corresponding to the sublimation temperature without going through the liquid phase (Figure 2.6). Differential scanning calorimetry (DSC) measurement of DCNP provided the glass transition temperature ($T_g$) of 27 °C (Figure 2.7) and a peak for the endothermic process appeared at 170.7 ˚C, which nearly agrees with the aforementioned phase transition temperature at 167.9 ˚C in Figure 2.5. Exothermic peaks observed at 64.8 °C and 123.7 °C in the DSC curve are assigned to the release of heat, which is associated with the crystallization of DCNP. (Figure 2.7). A proposed simple phase diagram is depicted for making it clearer to understand by readers as given in Figure 2.8. Thus, at low pressure, DCNP molecules are easier to sublimate without going through the liquid phase or decomposition.

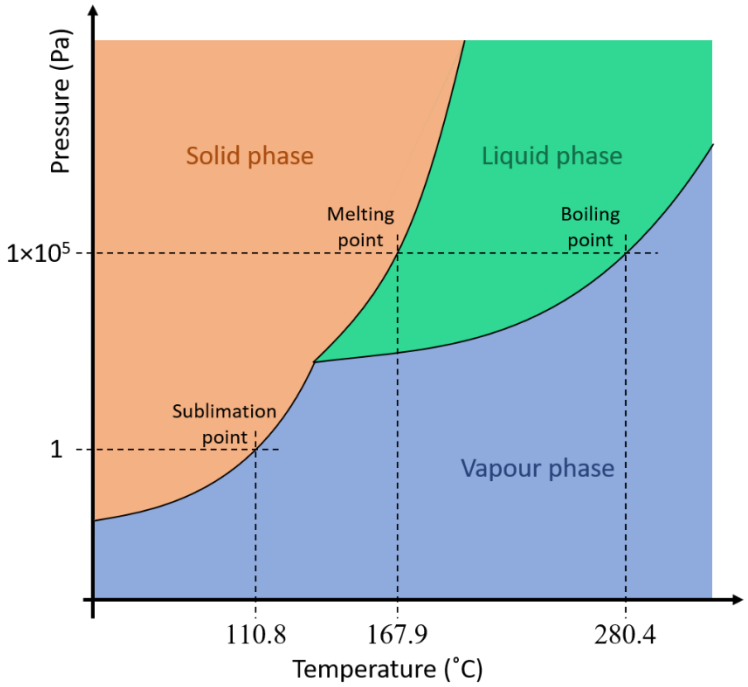


**Figure 2.8:** Proposed phase diagram for DCNP based on the results of TGA and DTA.

### 2.3.2 Photo-physical properties

The samples, which were used to measure the photo-physical properties, were DCNP solutions with various solvents, DCNP-doped poly(methylmethacrylate) (PMMA) films, DCNP neat films, and DCNP-doped BSBCz films. Figure 2.9a shows the photographs of these films under UV light. As shown in Figure 2.9b, the large overlap of the BSBCz emission band and the DCNP absorption band enables efficient Förster-type energy transfer from BSBCz to DCNP[6,7]. The effective FRET from BSBCz to DCNP was further confirmed by the fact that the PL of a 1 wt.%-DCNP:BSBCz film fully originates from DCNP and no shoulder peaks observed from BSBCz. Here, the PL was measured with an excitation wavelength of 337 nm, which is mainly absorbed by BSBCz host molecules.

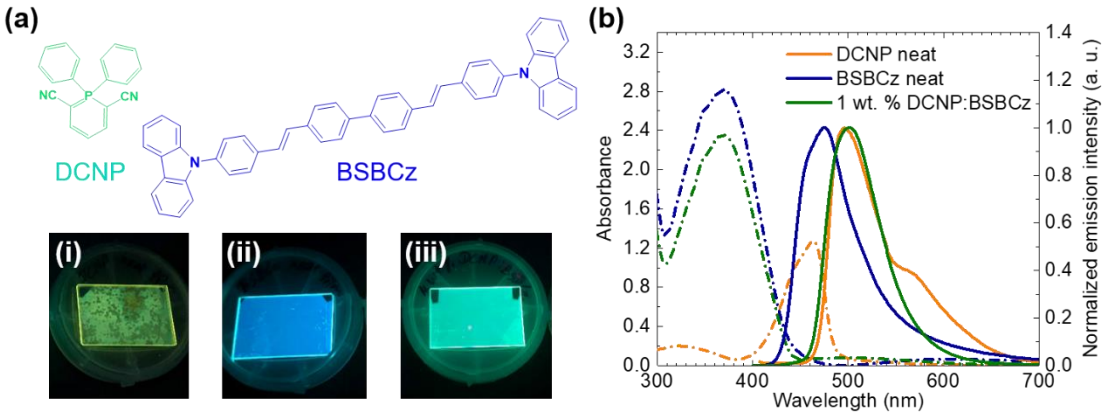


**Figure 2.9.** (a) Molecular structures of DCNP and BSBCz and photographs of (i) a DCNP neat film, (ii) a BSBCz neat film and, (iii) a 1 wt.%-DCNP-doped BSBCz film (200 nm) fabricated on quartz substrates under UV light irradiation ($\lambda_{ex}$ = 356 nm). DCNP easily crystallized in neat films [see (i) in (a)]. However, this crystallization was suppressed by doping DCNP into BSBCz [see (iii) in (a)] because BSBCz forms stable amorphous films without crystallization [see (ii) in (a)]. (b) Absorbance and normalized emission spectra of these samples. The excitation wavelength used for the PL measurement was $\lambda_{ex}$ = 337 nm.

An additional shoulder peak appeared around 575 nm in the PL spectrum of a DCNP neat film (Figure 2.9b), which was not observed in both solution and doped films. Thus, this additional peak is caused by the degenerated energy states of aggregated DCNP molecules in neat films. This common phenomenon of aggregation-induced emission quenching and considerably large concentration quenching of DCNP emission lead to a low PLQY of 5±2 % in the neat film. However, the PLQY was nearly 100 % in a diluted solution ($1\times10^{-5}$ M, in toluene). To investigate the emission quenching and identify the optimum doping concentration, several drop-casted DCNP:PMMA films and vacuum-deposited DCNP:BSBCz films were fabricated. The PLQY values increased as the DCNP concentrations were decreased, because of the suppressed concentration quenching and aggregation. The optimum PLQY reached (83~90 %) at a DCNP concentration of 0.3 wt.% for drop-casted PMMA films and 1 wt.% for vacuum-deposited BSBCz films (Figure 2.10).

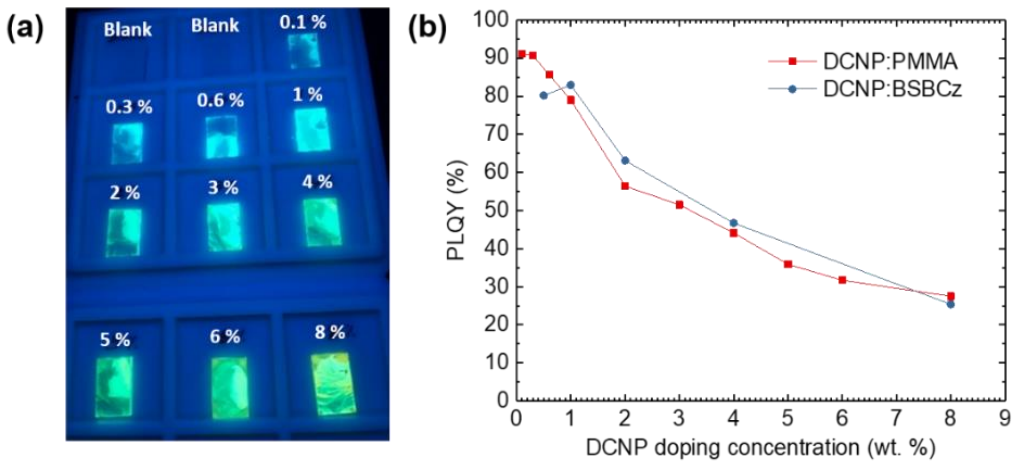


**Figure 2.10.** (a) Photograph under UV light ($\lambda_{ex}$ = 356 nm) when DCNP of different concentrations was doped into PMMA films. (b) Plot of PLQYs as a function of DCNP doping concentration in PMMA or BSBCz host films ($\lambda_{ex}$ = 337 nm).

The doping concentration of DCNP in BSBCz has to be optimized in order to obtain minimum concentration quenching of emission, efficient FRET from the BSBCz's singlets to the DCNP's singlets ($FRET_{S\text{-}S}$), high DET efficiency of reverse triplet transfer from the emitter to the host ($DET_{T\text{-}T}$) and suppressed STA by minimum FRET efficiency of emitter-emitter and emitter-host ($FRET_{STA}$). Here, I discussed the distance between excitons (molecules) to express the effect of doping concentration.

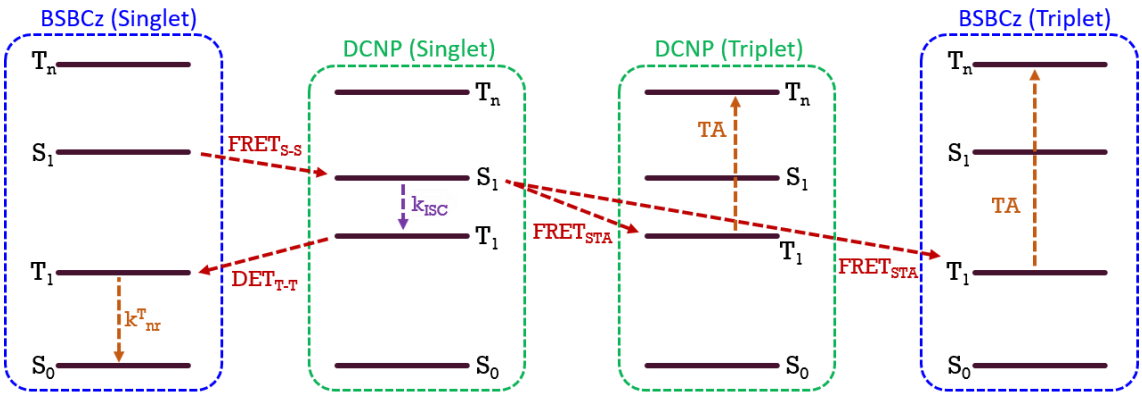


**Figure 2.11.** Schematic energy level diagram for plausible exciton energy transfer mechanisms in a DCNP:BSBCz guest-host system. $FRET_{S\text{-}S}$, $FRET_{STA}$, $DET_{T\text{-}T}$, $k_{ISC}$, $k^{T}_{nr}$, and TA stands for bimolecular FRET of singlet to singlet, FRET of singlet to triplet (STA), DET of triplet to triplet,and monomolecular intersystem crossing, triplet relaxation, and triplet absorption, respectively.

The rate of bimolecular FRET is expressed by the equation:

$$k_{FRET} = \frac{1}{\tau_D} \cdot \left(\frac{R_0}{r}\right)^6 \quad \text{(Eq. 2.1)}$$

where, $\tau_D$ is the donor lifetime (when no energy transfer occurs, ~ns), $R_0$ is the Förster radius, and $r$ is the distance between the donor and acceptor molecules. Here, $R_0$ is defined as the distance at which spontaneous decay from the donor and energy transfer to the acceptor are equally probable. Thus, decreasing the doping concentration increases the distance between the host and guest molecules, and eventually the FRET efficiency decreases. Therefore, it is important to decrease the doping concentration until the marginal level of residual host emission can be observed. At this marginal concentration, we can get the maximum distance to suppress STA while keeping efficient FRET from the host to guest molecules.

In an effort to understand an energy transfer process, time-resolved PL decay curves were measured from BSBCz neat films, 1 wt.%-DCNP:BSBCz films, and 1 wt.%-DCNP:PMMA films (Figure 2.12). The photophysical parameters of the BSBCz neat films and 1 wt.%-DCNP:PMMA films are shown in Table 2.1. As depicted in Figure 2.12d, 1 wt.%-DCNP:BSBCz films had two distinctive decay components in their transient PL decay curves. Here, I selected the two separate wavelength regions of interest (ROI), i.e., (A) 350–420 nm (BSBCz emission only) and (B) 550–700 nm (DCNP emission only), in order to estimate the decay lifetimes of a BSBCz host and a DCNP emitter, respectively. By assuming complete energy transfer from BSBCz to DCNP, the rate constants were estimated and tabulated in Table 2.2 and Figure 2.12e. The rate constants of the energy transfer ($k^S_{ET}$) and radiative emission ($k_r$) of the DCNP-doped BSBCz system were estimated to be $>2.0\times10^{10}$ $s^{-1}$ and $1.0\times10^{8}$ $s^{-1}$, respectively, which implies the high possibility of a DCNP-doped BSBCz composite film for a laser gain medium.

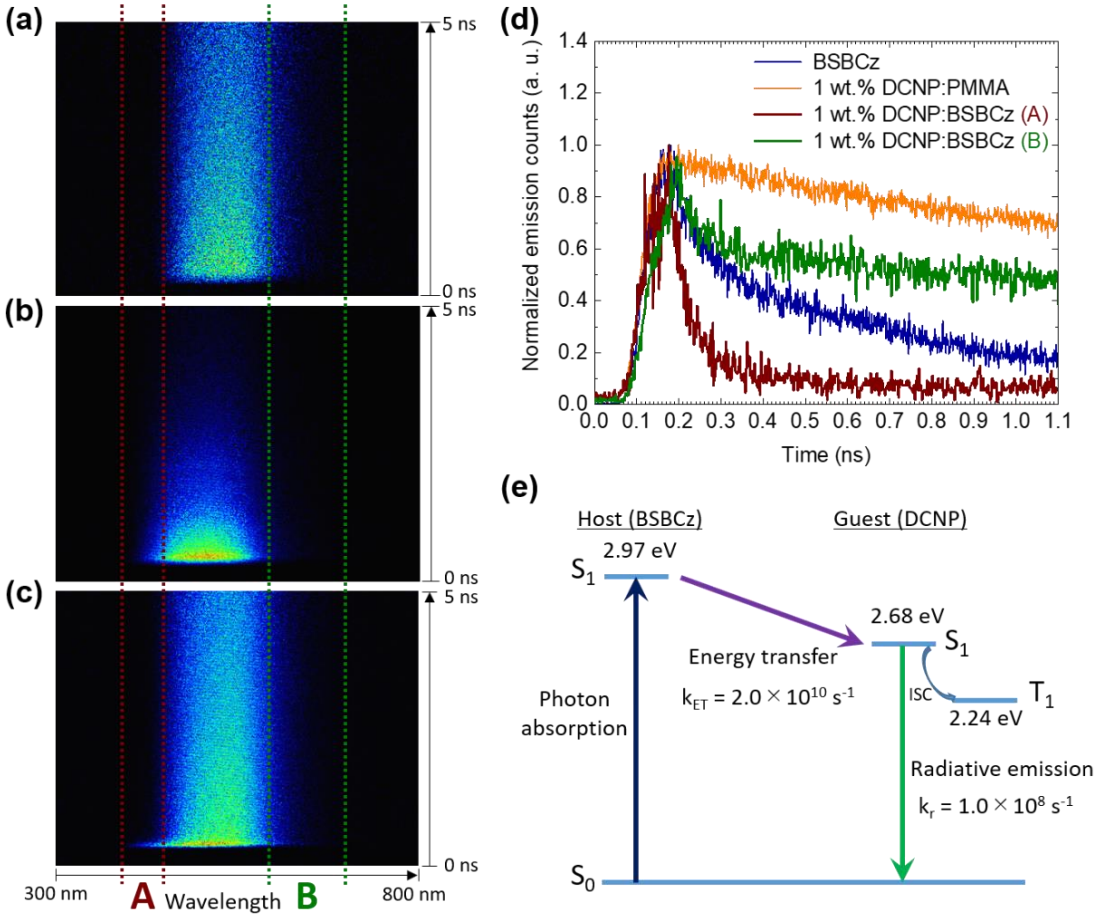


**Figure 2.12.** Streak camera imagesof (a) a 1 wt.%-DCNP:PMMA film, (b) a BSBCz neat film, and (c) a 1 wt.%-DCNP:BSBCz film. (d) Transient emission decays estimated from the streak camera images. (e) Using the fitting curves for transient emission decay, lifetime values were estimated and tabulated in Table 2.1 and Table 2.2, then the rate of exciton conversion processes in the host-guest matrix are depicted in the Jablonski diagram.

**Table 2.1.** Emission decay lifetimes estimated from Figure 2.12d, PLQYs and rate constants for a BSBCz neat film and a 1 wt.%-DCNP:PMMA film at 300 K.

| Film | Lifetime [ns][a)] (wavelength ROI [nm]) | PLQY [b)] | Rate constant [$s^{-1}$] |
|---|---|---|---|
| BSBCz neat film | 1.1 (350 to 700) | 0.78 | $6.8\times10^{8}$ |
| 1 wt.%-DCNP:PMMA film | 5.3 (350 to 700) | 0.79 | $1.5\times10^{8}$ |

**Table 2.2.** Emission decay lifetimes measured from Figure 2.12d, quantum yields and rate constants for a 1 wt.%-DCNP:BSBCz guest-host system at 300 K.

| Processes in guest-host film (1 wt.%-DCNP:BSBCz) | Lifetime [ns][a], (wavelength ROI [nm]) | Quantum yield [b] | Rate constant [$s^{-1}$] |
|---|---|---|---|
| Energy transfer from BSBCz to DCNP | 0.05 (A = 350 to 420) | 1.00 | $2.0\times10^{10}$ |
| Radiative emission from DCNP | 8.23 (B= 550 to 700) | 0.83 | $1.0\times10^{8}$ |

To understand the plausible exciton transfer mechanism from BSBCz to DCNP, a Jablonski energy diagram is illustrated in Figure 2.13. The energy levels of lowest excited singlet states of BSBCz and DCNP were estimated from the onset values of their PL spectra (Figure 2.9b). The energy level of the lowest triplet state of DCNP was estimated using the onset value of the monomolecular phosphorescent spectrum at 77 K (Figure 2.14), leading to the rather small $\Delta E_{ST}$ value of 0.44 eV for DCNP. Moreover, the reported triplet energy level for the BSBCz [calculated by density functional theory (DFT)][8] was taken into account, resulting in the $\Delta E_{ST}$ value of 1.49 eV.

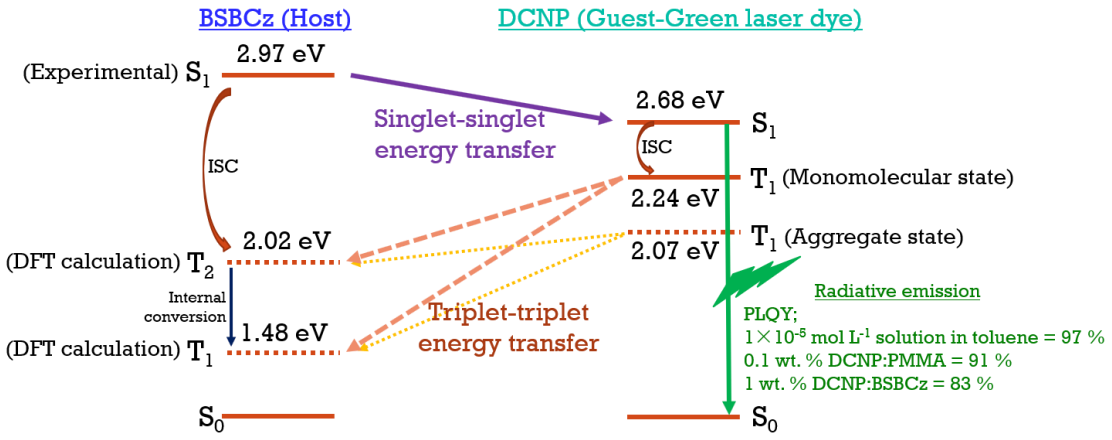


**Figure 2.13.** Jablonski diagram showing energy transfer in a DCNP:BSBCz guest-host matrix (For BSBCz, the reported triplet energy values were obtained from DFT calculation[8]).

As reported previously, the triplet exciton formation efficiency in BSBCz is approximately 4 %[2–4,9]. However, the rate of singlet energy transfer from BSBCz to DCNP is faster than the rate of ISC of BSBCz which can suppress the conversion of BSBCz singlet excitons into triplet excitons, resulting in almost all the singlet excitons transfer to DCNP molecules. Here, note that although the PLQY of 1 wt.%-DCNP:BSBCz is 83±2 %, the PLQYs of 0.1 wt.%-DCNP:PMMA and $1\times10^{-5}$ M solution in toluene are 91±2 % and 97±2 %, respectively. Therefore, it suggests that even a 1 wt.%-DCNP:BSBCz host-guest film has concentration quenching probably by self-absorption[10] due to the small Stokes-shift between DCNP absorption and emission (Figure 2.9b). By assuming $1\times10^{-5}$ M solution in toluene has negligible self-absorption, it can be estimated that 97±2 % singlet excitons of DCNP relaxed through radiative emission pathway while 3±2 % excitons are converted into triplet excitons via ISC. Interestingly, even those 3±2 % triplet excitons could be transferred to BSBCz host molecules via DET mechanism due to the lower triplet energy of BSBCz. Here, this DET energy transfer would be faster than the rate of triplet exciton formation in DCNP [$k_{ISC}$(DCNP)], because the DCNP:BSBCz molar ratio is 1:43 in the blend film. Therefore, this mechanism exhibits that triplet exciton formation in DCNP molecules is extremely negligible, that is further confirmed by phosphorescence, transient absorption measurement and transient emission decay at long pulsed excitation (temporal profiles) in 1 wt.%-DCNP-doped BSBCz films. As shown in Figure 2.14a, it is important to note that phosphorescence from the DCNP-doped BSBCz film at 77 K was not observable. However, DCNP in toluene solution, DCNP neat film, DCNP-doped 4,4’-bis(*N*-carbazolyl)-1,1’-biphenyl (CBP) or, PMMA films showed phosphorescence at 77 K.

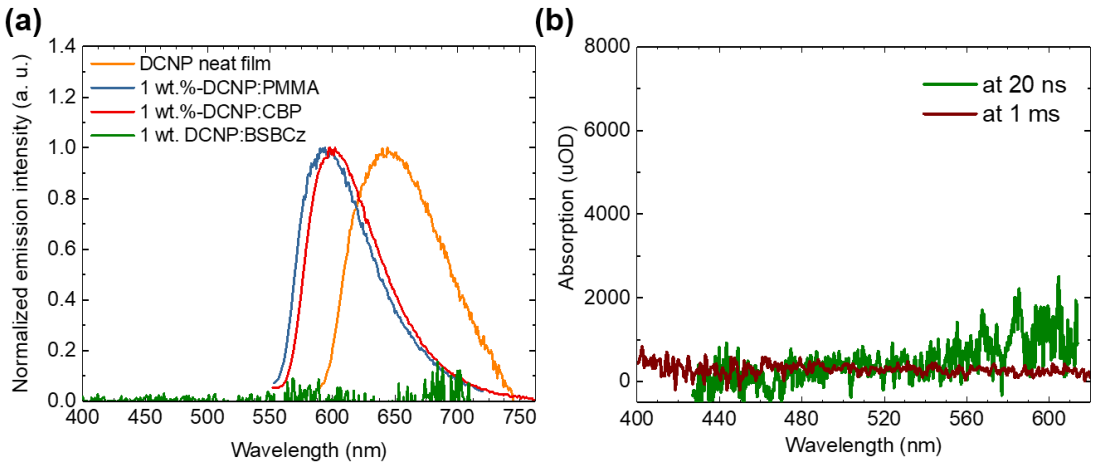


**Figure 2.14.** (a) Phosphorescence spectra at 77 K ($\lambda_{ex}$ = 337 nm). (b) Transient absorption spectra of a 1 wt.%-DCNP:BSBCz film at room temperature ($\lambda_{ex}^{pump}$ = 355 nm).

On the other hand, the rate of a bimolecular DET process is expressed as follows:

$$k_{DET} \propto \frac{h}{2\pi} P^2 J \cdot e^{\left[\frac{-2R_{DA}}{L}\right]} \quad \text{(Eq. 2.2)}$$

where $R_{DA}$ is the distance between donor and acceptor molecules, $L$ is the sum of van der Waals radius, $J$ is the normalized spectral overlap integral, $P$ is a constant, which is not easily related to experimentally determinable quantities, $h$ is the Plank constant. In order to get the efficient triplet scavenging process, the DET efficiency of the triplet energy transfer from the guest to host molecules should be higher. Decreasing doping concentration means an increase in distance between the host and guest molecules, which might be detriment for the triplet scavenging process. In a 1 wt.% DCNP:BSBCz system, the molar ratio between guest to host is 1:43 which means that the number of host molecules surrounding the emitter molecules are presumably high. However, even at this small doping concentration which I used in this thesis, the triplet scavenging process seemed working well, since, favorably, the triplet excitons formed on the host molecules migrate away from the emitter molecules via diffusion to the other host molecules. This process also leads to the suppression of FRET efficiency of the emitter-host STA. In addition, even if the triplet excitons of host molecules are living for long time, the triplet

scavenging process will not be overloaded, because there are 43 host molecules per emitter molecule, which readily accept triplet excitons. It is worth mentioning here that we have to choose the suitable doping concentration considering or balancing the above effects.

To evaluate more insights about triplet states of DCNP and BSBCz, I paid attention to observe transient absorption spectra. However, triplet absorption was not observable for DCNP in toluene solution, DCNP neat film, DCNP-doped CBP or PMMA films, DCNP-doped BSBCz films, and BSBCz neat films (Figure 2.14b). In order to increase the population of triplets to a detectable level, triplet absorption spectra were measured using tris[2-phenylpyridinato-C2,N]iridium(III) [$Ir(ppy)_3$] as a triplet sensitizer (Figure 2.15a,b). As depicted in Figure 2.15e,f, the triplet lifetimes of BSBCz and DCNP were estimated at 224 ns and 35 μs respectively. Therefore, $k^{T}_{nr}$(BSBCz) is $4.5\times10^{6}$ $s^{-1}$ and $k^{T}_{nr}$(DCNP) is $2.9\times10^{4}$ $s^{-1}$, showing that the triplet relaxation of BSBCz is approximately 100 times faster than the triplet relaxation of DCNP itself (Figure 2.16). $k_{ISC}$(DCNP) is calculated using Eq. 2.3;

$$k_{\mathrm{ISC}} = \frac{\Phi_{\mathrm{ISC}}}{\tau_{\mathrm{FL}}} = \Phi_{\mathrm{ISC}} \cdot k_{\mathrm{FL}} = (1 - \Phi_{\mathrm{FL}})k_{\mathrm{FL}} \qquad \text{(Eq. 2.3)}$$

where, $\Phi_{FL}$ and $\Phi_{ISC}$ are the quantum efficiency of prompt fluorescence and intersystem crossing, respectively. $k_{FL}$ and $k_{ISC}$ are the rates of prompt fluorescence and intersystem crossing, respectively. $\tau_{FL}$ is fluorescence lifetime. Using Eq. 2.3 and considering $\Phi_{FL}$(DCNP in toluene) = 0.97 and $k_{FL} = 1.0\times10^{8}$ $s^{-1}$ (Figure 2.12, Table 2.2), the $k_{ISC}$(DCNP) resulted in $3.0\times10^{6}$ $s^{-1}$ (Figure 2.16).

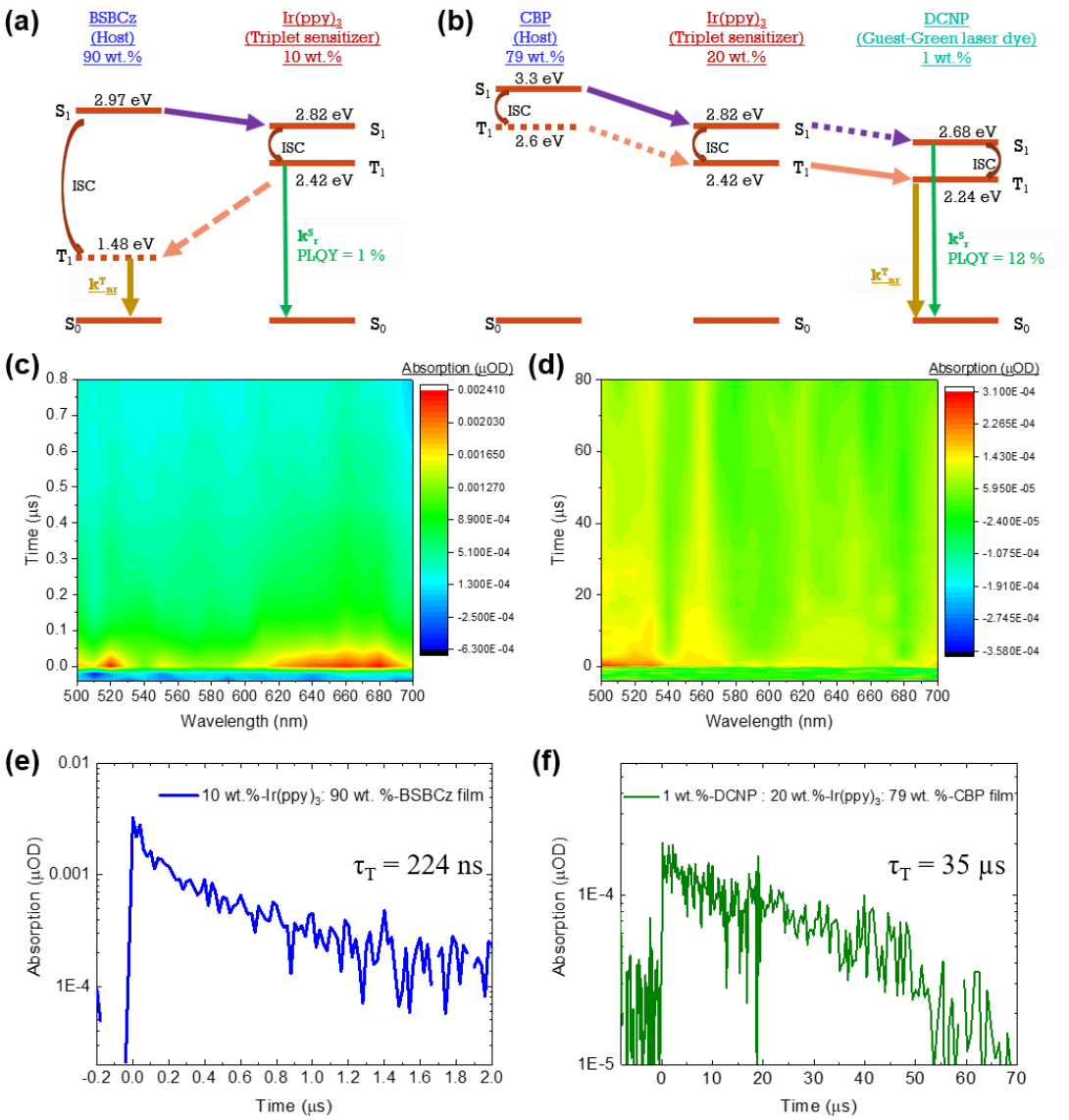


**Figure 2.15.** Triplet exciton sensitization onto BSBCz and DCNP; energy level diagrams of doped systems used to sensitize triplet excitons on (a) BSBCz and (b) DCNP. Contour map of time versus transient absorption spectra for (c) BSBCz and (d) DCNP. Triplet exciton decay spectra at 600 nm for (e) BSBCz and (f) DCNP.

The reverse energy transfer from DCNP to BSBCz ($k^{T}_{ET}$) is a bimolecular triplet-triplet energy transfer which depends on the rate of a Dexter process (Figure 2.16). Thus, it depends on the distance between a DCNP guest molecule and a BSBCz host molecule. In the 1 wt.%-DCNP:BSBCz system, the molar ratio of the BSBCz host molecules to the DCNP guest molecules is 43:1. Thus, a DCNP guest molecule is assumed to be surrounded by many host BSBCz molecules, leading to a high possibility of DET

mechanism in case of the reverse triplet transfer. In addition, even if the triplet excitons of host molecules are living for long time, the triplet scavenging process will not overloaded, because there are 43 host molecules per emitter molecule, which are readily available to accept triplet excitons. Moreover, this reverse triplet transfer from DCNP to BSBCz is spin conserved transition. Hence, when compared with the rate of intersystem crossing of DCNP [$k_{ISC}$(DCNP)] and the rate of triplet relaxation in BSBCz host molecules [$k^{T}_{nr}$(BSBCz)], this bimolecular DET process should be much faster. Therefore, in the 1 wt.%-DCNP:BSBCz guest-host system, the rate-determining step is the $k_{ISC}$(DCNP) which is the slowest step among all of the processes.

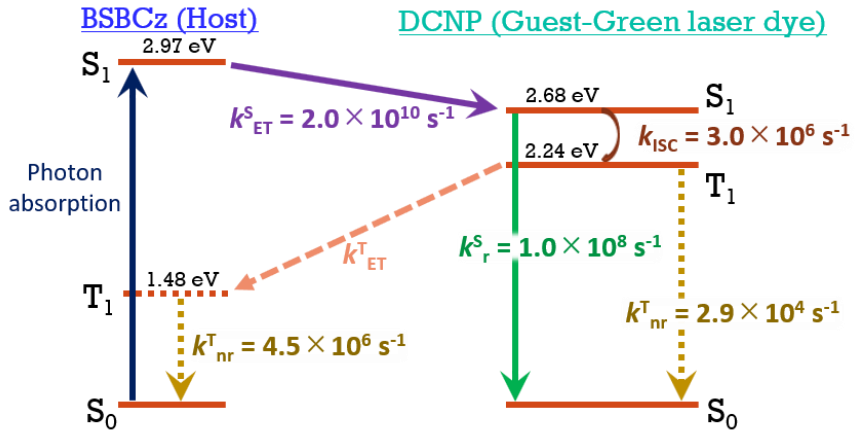


**Figure 2.16.** Excited-state energy diagram of BSBCz and DCNP, with rate constant values.

This mechanism was experimentally proved by the phosphorescence spectra and transient absorption spectra. Phosphorescence from a DCNP-doped BSBCz film at 77 K was not observable, while a DCNP solution in toluene, a DCNP neat film, a DCNP-doped CBP or PMMA film showed phosphorescence at 77 K. These results indicate that the triplets of DCNP cannot contribute to phosphorescence but are quickly scavenged by the BSBCz host molecules in the DCNP doped BSBCz films. Even though, DCNP solution in toluene, a DCNP neat film and a DCNP-doped PMMA film showed phosphorescence at 77 K, those samples did not show detectable triplet absorption at room temperature.

Reason for this result might be due to increased nonradiative triplet relaxation rate of DCNP [$k^{T}_{nr}$(DCNP)] at room temperature compared to 77 K. Thus, low $\phi_{ISC}$ and high $k^{T}_{nr}$(DCNP) lead to negligible triplet exciton population density on DCNP molecules at room temperature which is not at the detectable level for transient absorption of our instrument. With consistence to non-detectable phosphorescence from DCNP doped BSBCz films, the same films showed no detectable triplet absorption due to negligible triplet exciton population density in either DCNP or BSBCz which resulted by the efficient triplet scavenging mechanism. These results also verified that the rate of triplet energy transfer ($k^{T}_{ET}$) and $k^{T}_{nr}$(BSBCz) is faster than $k_{ISC}$(DCNP) (Figure 2.16). Overall, because of $k_{ISC}$(DCNP) being the rate-determining step (slowest step) in the DCNP:BSBCz system, $k^{T}_{ET}$ cannot be estimated experimentally in this guest-host system. Advantageously, no triplet accumulation can be observed in the DCNP:BSBCz guest-host matrix, leading to a significant improvement of the CW laser performance.

### 2.3.3 ASE properties

Solid-state ASE studies were conducted with neat and composite films to evaluate their potential use as optical gain material (Figure 2.17a-c). For the ASE measurement, each film was measured 6 times at the different positions of the sample edge. Each measurement was separately plotted, providing plots similar to Figure 2.17a and then the ASE threshold values were averaged with standard deviation. This guest-host matrix demonstrated a low ASE threshold of 1.1 μJ $cm^{-2}$ for doped films (Figure 2.17b) without taking account for transmission losses, i.e., OD of the films. With an increase of DCNP doping concentrations, PLQYs decreased while ASE threshold increased accordingly (Figure 2.17b) and ASE peaks were redshifted (Figure 2.17c).

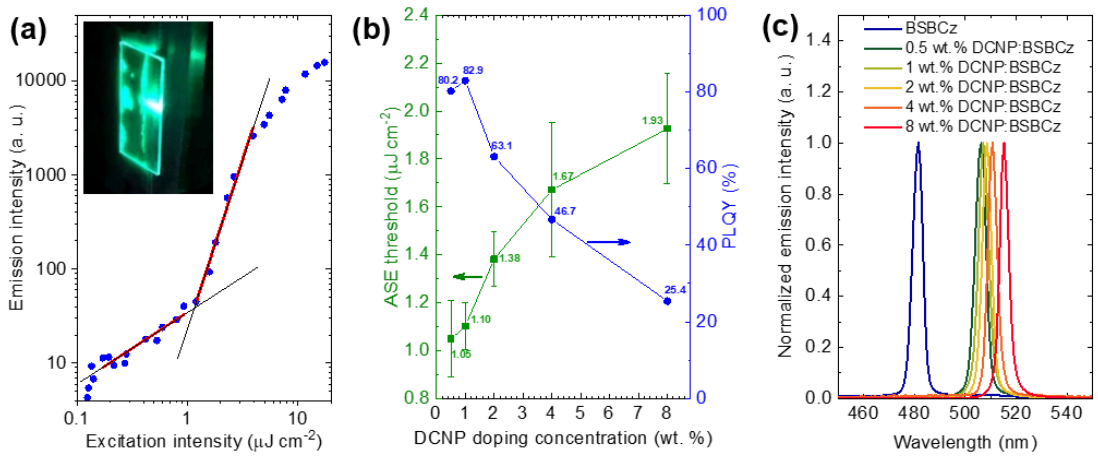


**Figure 2.17.** ASE from DCNP:BSBCz film on quartz substrate in nitrogen environment; (a) normalized ASE spectra variation upon DCNP doping concentration in BSBCz (b) emission intensity versus excitation intensity plot of 1 wt.%-DCNP:BSBCz film, (b-inset) photograph of ASE operation at 5 times above threshold, (c) average ASE threshold and PLQY versus DCNP doping concentration in BSBCz.

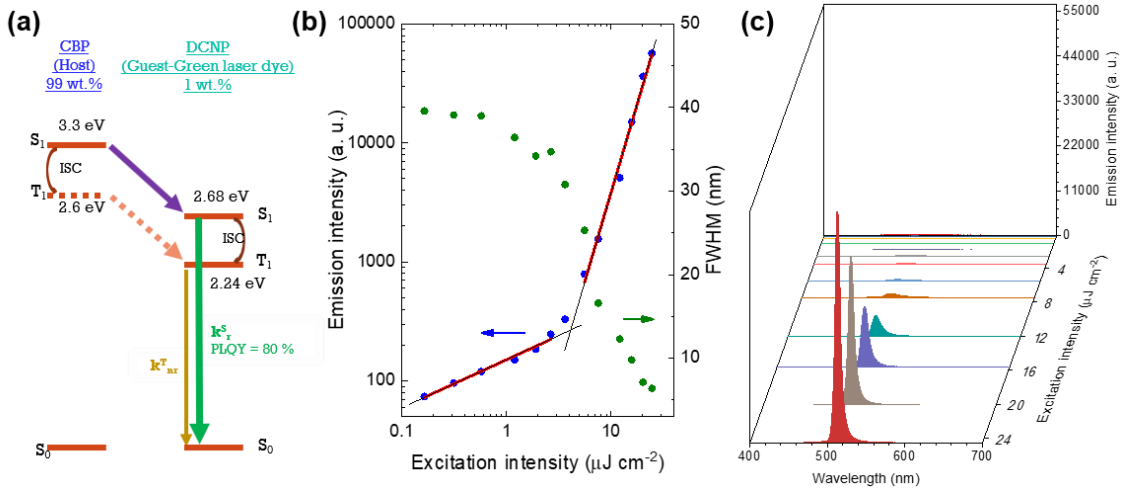


**Figure 2.18.** ASE study of a 1 wt.%-DCNP:CBP film; (a) Jablonski diagram showing energy levels of DCNP:CBP host-guest matrix, (b) emission intensity and FWHM versus excitation intensity plot, (c) each ASE spectrum.

In order to demonstrate ASE capability of DCNP itself, a conventional host material CBP, was used as the host (Figure 2.18a). As the results depicted in Figure 2.18b,c, ASE threshold of 1 wt.%-DCNP doped CBP film is 3.6 μJ cm$^{-2}$. Furthermore, DCNP molecules are intentionally doped in non-emissive polymer matrix to observe its direct excitation behavior at 337 nm excitation wavelength. A

1 wt.%-DCNP:PMMA film did not show ASE characteristics under optical excitation intensities of up to 200 μJ $cm^{-2}$, probably due to low exciton formation density in the excitation area. The low doping concentration (1 wt.%) in an optically inert non-emissive polymer matrix (PMMA) is the main reason for low exciton density formation in the excitation area (Figure 2.19).

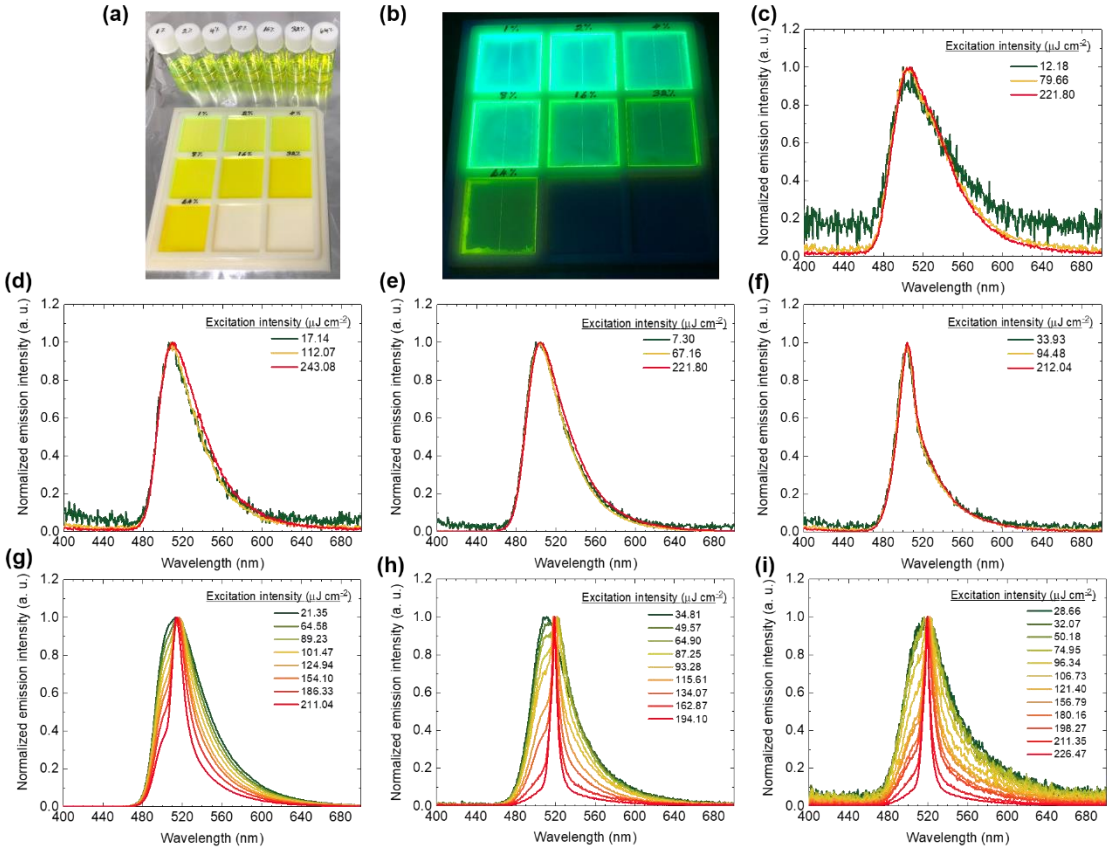


**Figure 2.19.** Photograph when DCNP doped PMMA films were spin coated onto glass substrate and kept under (a) ambient light and (b) UV illumination light ($\lambda_{ex}$ = 356 nm). Normalized ASE spectra of DCNP doped PMMA films. ($\lambda_{ex}$ = 337 nm, pulse width = 3.5 ns, in air); (c) 1 wt.%, (d) 2 wt.%, (e) 4 wt.%, (f) 8 wt.%, (g) 16 wt.%, (h) 32 wt.%, and (i) 64 wt.%.

To increase absorption at 337 nm and increase the number of DCNP molecules in certain volume (thereby exciton density), I carried out the ASE experiment with a series of the doping concentration of 1, 2, 4, 8, 16, 32, and 64 wt.%. However, it is important to note that increasing the DCNP concentration leads to rapid decrease of PLQY due to

concentration quenching (Figure 2.10). Therefore, with increasing doping concentration, results decreased PLQY and an increase of the ASE threshold according to the Einstein's relationship for B coefficient. As depicted in Figure 2.19, I observed ASE characteristics in the DCNP:PMMA films above 16 wt.%-DCNP doping concentration. Therefore, host molecules play an important role in this host-guest matrix to obtain high exciton density by exciton funneling into DCNP molecules.

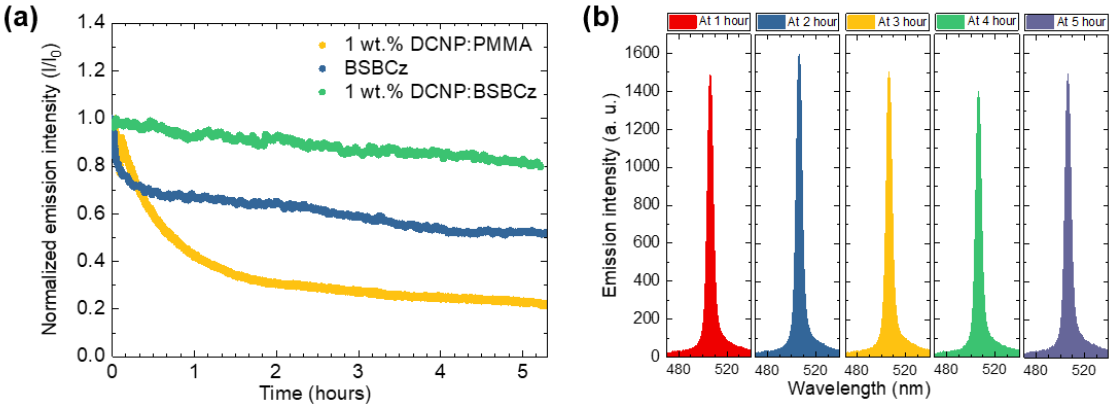


**Figure 2.20.** ASE decay profile measuredin nitrogen at room temperature ($\lambda_{ex}$ = 337 nm). (a) Normalized emission intensity versus time, (b) Respective emission spectra with time for 1 wt.%-DCNP:BSBCz film.

When the stability of ASE of a 1 wt.%-DCNP:BSBCz film was checked with a BSBCz neat film (Figure 2.20), the composite film showed better ASE stability than PL stability of the BSBCz neat films when measured 24 times higher excitation intensity (26 μJ $cm^{-2}$) than the ASE threshold. The half-time ($LT_{50}$), at which ASE intensities decreased to half of the initial, was ~16.5 and 4.8 hrs. for a 1 wt.%-DCNP:BSBCz and a BSBCz neat film, respectively. Here, the $LT_{50}$ of PL in 1 wt.%-DCNP:PMMA film is ~0.8 hrs. Notably, there was no significant broadening of FWHM in the emitted ASE spectrum after long time exposures at 24 times higher excitation intensity (26 μJ $cm^{-2}$) than the ASE threshold (Figure 2.20b). These results suggest that the triplet excitons formed on a DCNP emitter are quickly scavenged by BSBCz host molecules (Figure 2.13), whose non-radiative triplet exciton decay ($k^{T}_{nr}$) is very fast (Figure 2.16) and have

spectral separation with the ASE spectrum of DCNP (Figure 2.21), thereby eliminating triplet-induced losses[8,11].

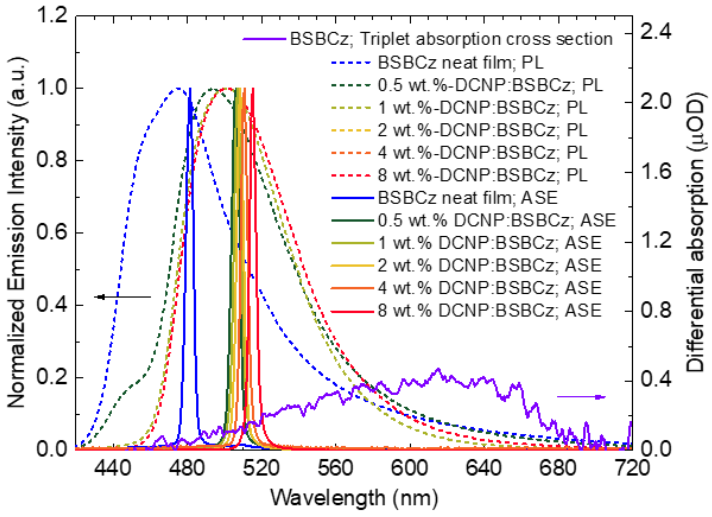


**Figure 2.21.** Spectral comparison of ASE spectra of DCNP and the triplet absorption cross section spectrum of BSBCz.

### 2.3.4 Fabrication of DFB resonators

In a DFB structure, laser oscillation takes place when the following Bragg condition is satisfied: $m\lambda_{Bragg} = 2n_{eff}\Lambda_m$, where $m$ is the order of diffraction, $\lambda_{Bragg}$ is the Bragg wavelength, $n_{eff}$ is the effective refractive index of the gain medium, and $\Lambda$ is the period of the grating. The second-order DFB structure ($m = 2$) gives a vertical outcoupling[12], highly divergent beam with rather high lasing threshold due to radiation loss, while the first-order DFB structure ($m = 1$) provides strong feedback and emits at the edge of the device, giving rise to low diverge beam with low lasing threshold. As shown in previous reports[3,4] I incorporated a mixed-order DFB structure ($m = 1$ and 2) to introduce both features of first and second-order DFB resonator structures to obtain surface emitting low lasing threshold. Supercell of my mixed-order DFB consisted of six periods of first-order and two periods of second-order in a sequence (Figure 2.25a). The grating periods ($\Lambda$) to fabricate DCNP:BSBCz lasers were calculated using $\lambda_{ASE}$ as $\lambda_{Bragg}$,

and a $n_{eff}$ value of 1.72 measured from ellipsometry. The first, second, or mixed-order DFB resonator structure was engraved on a silicon dioxide layer sputtered on glass substrates with electron-beam lithography and reactive ion etching (Figure 2.22).

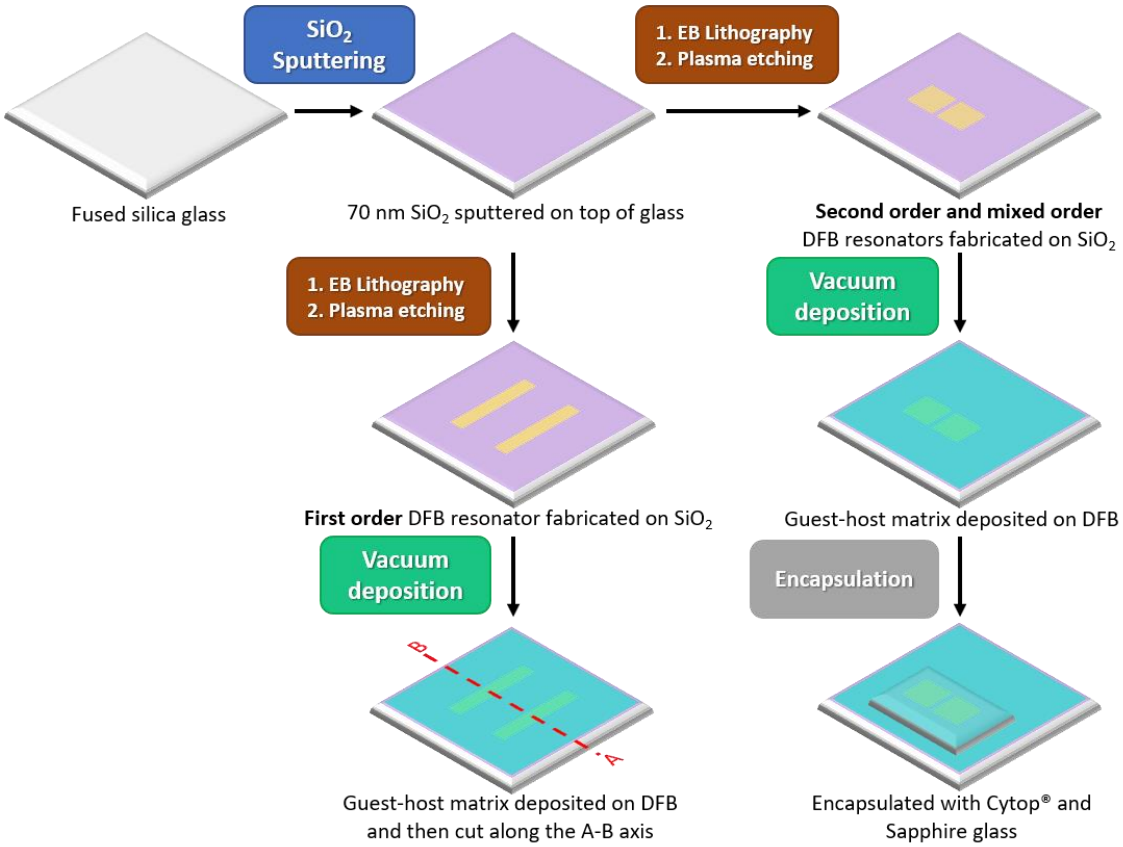


**Figure 2.22.** Schematic procedure of OSSL-device fabrication for optical pumping laser.

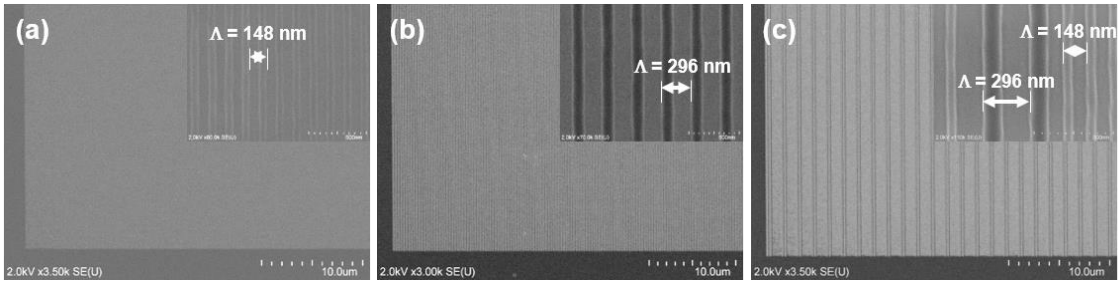


**Figure 2.23.** SEM image of 3500× and (inset) 80000× magnification of a DFB grating (d) first-order DFB (e) second-order DFB (f) mixed-order DFB.

The area of a resonator structure was 5 × 5 $mm^2$ and the period lengths of the first-and second-order grating for DCNP:BSBCz were designed as per the calculated period values ($\Lambda_1$ = 148 nm and $\Lambda_2$ = 296 nm). Scanning electron microscopy (SEM)

(Figure 2.23) was used to confirm the grating periods fabricated in this work and the SEM images were in good accordance with my specifications. A 1 wt.%-DCNP:BSBCz film with a thickness of 200 nm was fabricated by vacuum deposition on top of the DFB resonator structure. To seal the organic laser devices, the substrates were encapsulated (using a nitrogen filled glove box) in optically transparent fluoropolymer CYTOP® (refractive index ≈ 1.35) and thermally conductive sapphire lids (refractive index ≈ 1.77, thermal conductivity ≈ 25 W $mK^{-1}$ at 300 K). These CYTOP® and sapphire lids demonstrated good transparency at the lasing wavelengths. The schematic diagram of the fabrication method of the organic thin-film laser is shown in Figure 2.22.

### 2.3.5 Lasing studies in DFB structures under short pulsed excitation

Once DFB lasers were successfully fabricated, they were optically pumped with an optical pulse excitation from a nitrogen laser to examine the lasing properties of samples. Schematic setup to detect laser emission from edge and surface emission DFB devices are depicted in Figures 2.22a and 2.23b**,** respectively.

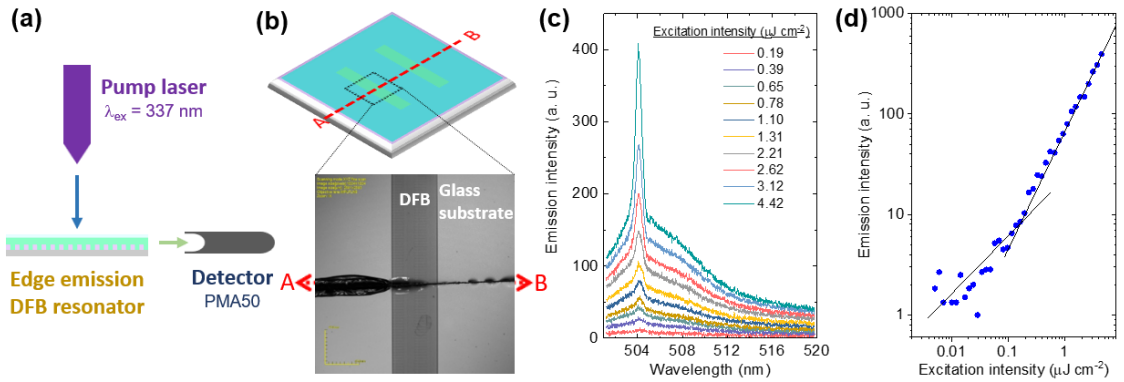


**Figure 2.24.** (a) schematic diagram of side view of apparatus setup for edge emission laser detection. (b) schematic and respective microscope image which shows the first-order DFB and the cut line. Optically pumped edge-emission-laser using first-order DFB ($\lambda_{ex}$ = 337 nm, short pulsed); (c) emission spectra (d) emission intensity versus excitation intensity.

In order to observe edge emission from the first-order DFB lasers, the substrates

should be cut through the axis shown in Figure 2.24b. The edge and surface emission lasing profiles of the 1 wt.%-DCNP:BSBCz films with first, second-order DFB resonator structures are shown in Figure 2.24c and Figure 2.25c, respectively.

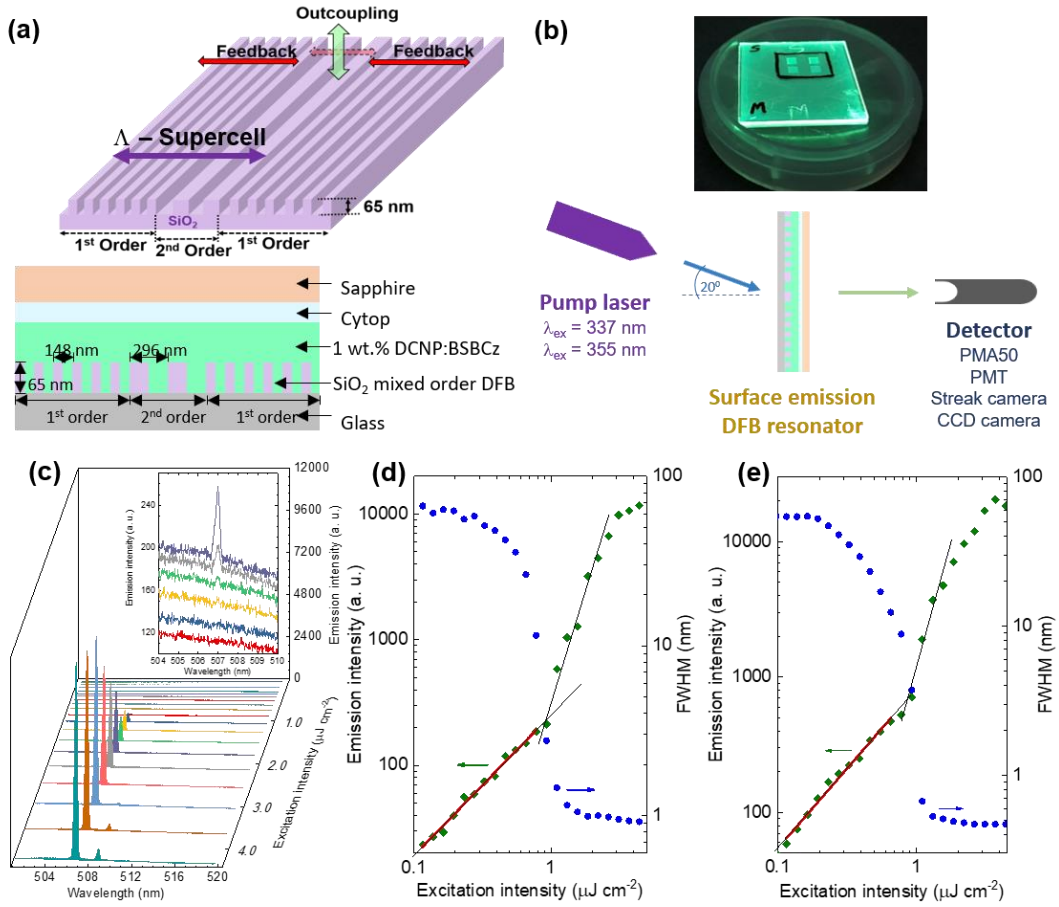


**Figure 2.25.** (a-top) Supercell pattern of mixed-order DFB consisting with two second-order pitches and two sets of six first-order pitches. (a-bottom) schematic diagram of cross section of mixed-order OSSL device. (b-top) Image of DFB-OSSL devices under UV light illumination ($\lambda_{ex}$ = 356 nm). (b-bottom) schematic diagram of apparatus setup for surface emission laser detection. Optically simulated laser emission ($\lambda_{ex}$ = 337 nm, pulse width = 3.5 ns ); (c) emission spectra versus excitation intensity from second-order DFB, (c-inset) evolution of Bragg-dip near to the threshold energy density, intensity and FWHM versus excitation intensity from (d) second-order DFB (e) mixed-order DFB.

The lasing thresholds of DFB lasers are summarized in Table 2.4. I demonstrated the lowest lasing threshold value of 0.18 μJ $cm^{-2}$ from first-order DFB devices (Figure 2.24d). However, I obtained slightly higher lasing threshold values of 0.86 and 0.91 μJ $cm^{-2}$ from mixed-order and second-order DFB lasers, respectively

(Figure 2.25d,e). This indicates that first-order DFB structures work well compared to the second-order and mixed-order DFB structures in order to reduce the lasing threshold. In particular, the lasing threshold obtained from the DFB structure of a composite film is lower than that of the ASE threshold, because of the stimulated emission due to resonance feedback from the DFB resonator (Table 2.4). A Bragg dip corresponding to the stopband of the DFB grating was observed at 508 nm under excitation intensity below lasing threshold 0.86 μJ $cm^{-2}$ (Figure 2.25c-inset). The FWHMs of the lasing obtained from first, second and mixed-order DFB structures are 0.61, 0.92, and 0.47 nm, respectively (Figure 2.25 and Table 2.4).

Moreover, in all of my ASE and laser results, a gain saturation region was observed after the threshold in emission intensity versus excitation intensity curves (Figures 2.17a and 2.25d,e). This typical phenomenon for light amplification from thin-film samples is observed due to saturated exciton population density. The degree of the gain saturation depends on several parameters such as types of gain materials used, optical density of a gain material at a certain excitation wavelength, pulsed width of the pump source, and degradation of a gain material and the microcavity structures used to induce waveguide.

After the onset of lasing, it becomes an avalanche of radiative relaxation due to stimulated emission. Therefore, it is no longer spontaneous emission which obeys first-order decay kinetics of fluorescence[13]. Hence, decay lifetime of laser is much shorter than the decay lifetime of spontaneous emission. To distinguish decay lifetime of laser and spontaneous emission, the time-resolved PL decay curves were measured for mixed-order DFB devices with a 1 wt.%-DCNP:BSBCz film using a picosecond pulsed excitation laser (Figure 2.26). Figure 2.26a shows the respective streak camera images at different excitation power.

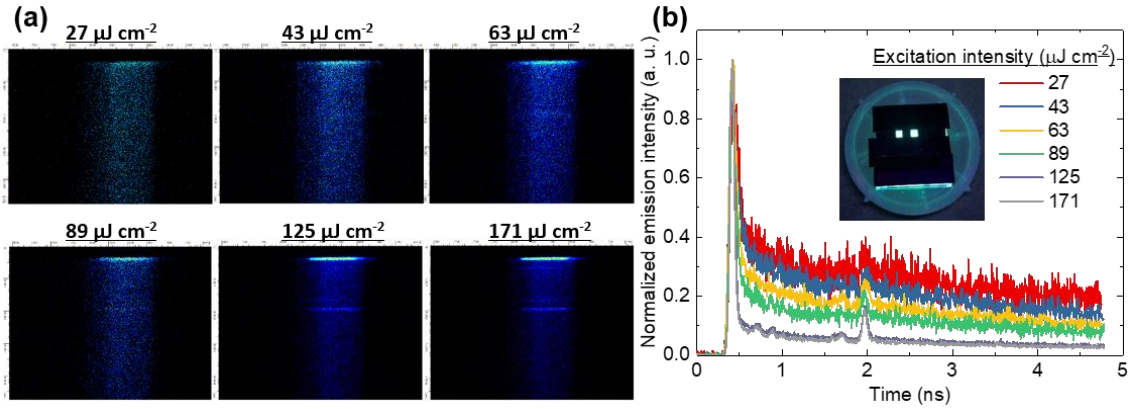


**Figure 2.26.** Transient emission at 5 ns streak time scale when DFB area illuminated with different excitation intensities (excited using Nd:YAG laser; $\lambda_{ex}$ = 355 nm, pulse width = 30 ps, repetition rate = 10 Hz); (c) streak camera images, (d) respective emission decay curves that demonstrate two distinctive emission components i.e., stimulated emission as the prompt component and spontaneous emission as the delay component; the additional spikes observed only at higher intensities around 2 ns is due to our instrumentation problem which is not affecting to data fitting, (d-inset) an optical image of substrate that exposing only its DFB area to UV illumination light ($\lambda_{ex}$ = 356 nm).

The decay profiles (Figure 2.26b) clearly showed that two distinct emission components which are laser (stimulated emission; prompt component) and spontaneous (delayed component) emission. At low excitation power, both laser and fluorescence were visible whereas, upon increasing the excitation power, laser was clearly enhanced while spontaneous emission diminished. Then, the lifetimes of cavity induced spontaneous emission were obtained by fitting the second component of the decay curves with an exponential decay function (Eq. 2.4). The lifetimes of cavity induced spontaneous emission estimated from the decay curves were in between 2.1 to 3.4 ns (Table 2.3) which are shorter than the PL lifetime (8.23 ns).

$$I(t) = A_1 e^{\left(\frac{-t}{\tau_1}\right)} \qquad \text{(Eq. 2.4)}$$

where, I(t) = emission intensity at time t, $A_1$ = pre-exponential factor, $\tau_1$ = lifetime of spontaneous emission

**Table 2.3.** Table of lifetime from the exponential decay fitting for the second emission components of mixed-order DFB emission decay profiles depicted in Figure 2.26b.

| Excitation intensity [μJ cm$^{-2}$][a)] | τ [ns] |
|---|---|
| 27 | 3.4 |
| 43 | 3.1 |
| 63 | 2.8 |
| 89 | 2.5 |
| 125 | 2.2 |
| 171 | 2.1 |

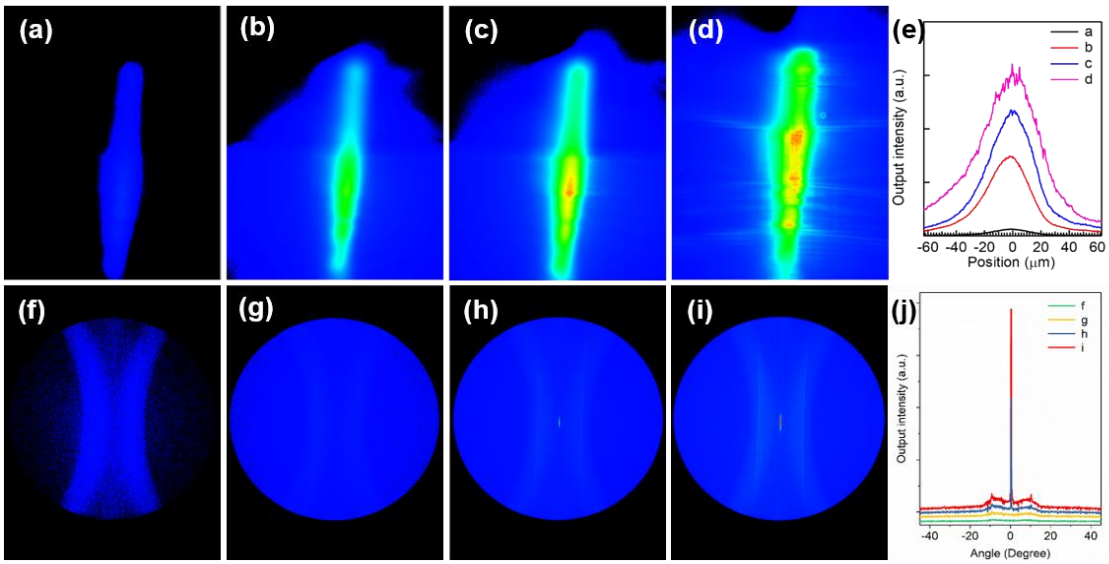


**Figure 2.27.** CCD camera images of diffraction beam interference pattern from second-order DFB under optical pumping ($\lambda_{ex}$ = 337 nm, pulsed); near-field interference (a) below threshold (b,c) near threshold (d) above threshold (e) respective intensity versus position plot of beam cross-sections, and far-field interference; (f) below threshold (g,h) near threshold (i) above threshold (j) respective intensity versus angle plot of beam cross-sections.

Further clarification of laser behavior was investigated by examination of the beam divergence from the laser output below, near and above the lasing threshold of the DFB device with a 1 wt.%-DCNP:BSBCz composite film using near field and far field interference spectra. The far field interference patterns indicate the existence of a well-

defined beam, which is formed only above the lasing threshold. Diffraction laser beam angle of far field interference was estimated using diffraction grating equation $\sin\theta = m\lambda/\Lambda$, where $\Lambda$ is the period of the supercell, $\lambda$ is the wavelength of laser emission, $m$ is the order of diffraction and $\theta$ is the diffraction angle of the emitted laser beam.

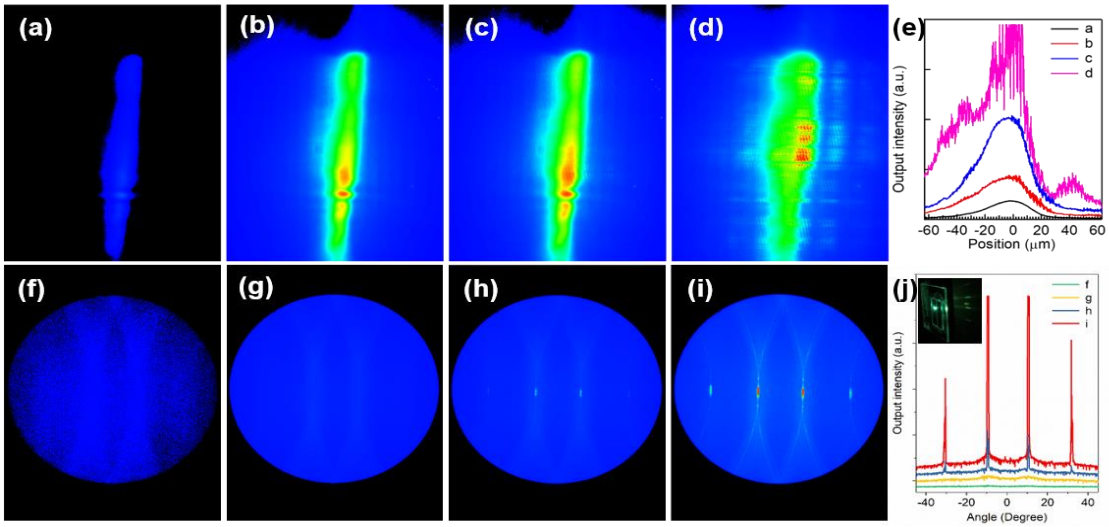


**Figure 2.28.** CCD camera images of diffraction beam interference pattern from mixed-order DFB under optical pumping ($\lambda_{ex}$ = 337 nm, pulsed); near-field interference (a) below threshold (b,c) near threshold (d) above threshold (e) respective intensity versus position plot of beam cross-sections, and far-field interference; (f) below threshold (g,h) near threshold (i) above threshold (j) respective intensity versus angle plot of beam cross-sections. Laser emission interference pattern from mixed-order DFB is verified where the experimental beam angle consisting with constructive interference beam angle calculated using diffraction grating equation. (j-inset) photograph of interference pattern on an illuminance paper.

In my mixed-order DFB grating structure, the period of the supercell is 1480 nm [$\Lambda_{supercell} = 6\Lambda_1 + 2\Lambda_2 = (6\times148 + 2\times296)$ nm] when the resonator structure is designed to oscillate at 508 nm wavelength of light output. Hence, diffraction laser beam angle for the first-order interference was estimated to be 20.07°. The far field beam cross sections are consistent with those of estimated value (Figure 2.28j) for the mixed-order supercell. The interference pattern was observed by placing a luminescent paper in front of the mixed-order DFB device (Figure 2.28j-inset). By looking at the near field patterns of the

output beam, I clearly observed fringes when excitation intensity above the threshold. The nearfield and far-field images (Figure 2.27 and Figure 2.28), along with the two distinctive emission components in time resolved decay (Figure 2.26) and resulting narrow spectra (Figure 2.25), clearly confirmed that the surface emission lasing from a 1 wt.%-DCNP:BSBCz film.

### 2.3.6 Lasing studies in DFB structures under CW operation

As a 1 wt.%-DCNP:BSBCz film showed negligible triplet exciton accumulation in the gain region as discussion in section 2.3.2, focus has been paid to further explore about CW operation. The fabricated DFB devices were investigated for laser characteristics at t-CW excitation using an inorganic laser diode operating at 355 nm with a maximum power of 25 mW. The detection was coupled with streak camera and measurements were taken at a 1 ms time scale which was the maximum limit of streak camera. Results given in Figure 2.29 show the streak camera images and emission profiles of laser integrated over 100 cycles of the encapsulated 1 wt.%-DCNP:BSBCz films fabricated on second and mixed-order DFB structures at a pumping power of 3.6 kW $cm^{-2}$ under t-CW excitation.

When the devices were operated with t-CW excitation to produce green emitting laser (Figure 2.29), laser thresholds were found to be around 76 and 72 W $cm^{-2}$ for second-order and mixed-order DFB devices, respectively (Figure 2.29d and Table 2.4). The inset of Figure 2.29d shows the interference pattern observed by an illuminance paper placed in front of the DFB laser device. Encapsulation of the laser devices using a thermally conductive sapphire lid successfully enabled lasing action under CW operation with higher stability due to the suppression of laser-induced thermal degradation laser ablation[14].

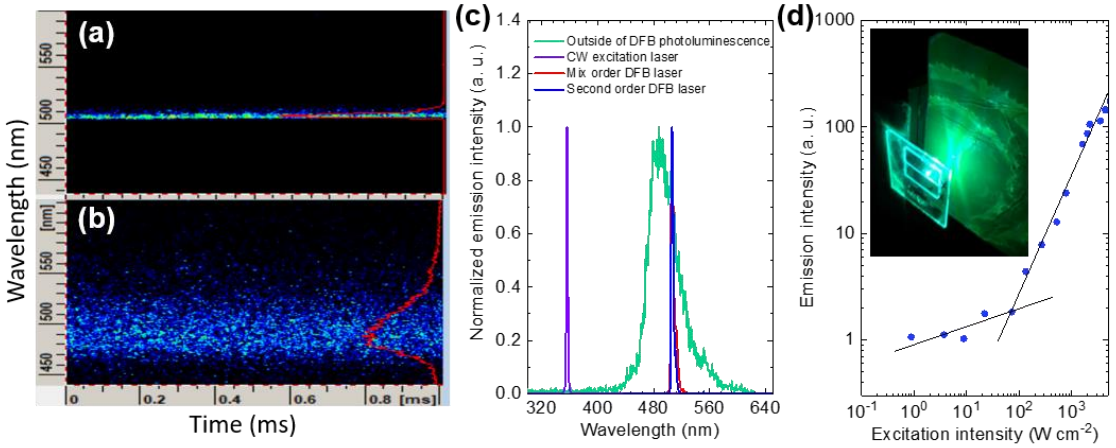


**Figure 2.29.** CW laser operation when excited with t-CW laser ($\lambda_{ex}$ = 355 nm); streak camera images from (a) mixed-order DFB (b) outside of the DFB (d) respective emission spectra. (c) emission intensity versus excitation intensity plot from second-order DFB, (c-inset) the fan shaped interference pattern observed when an illumination paper placed in front of DFB laser emission.

**Table 2.4 :** Threshold at short pulsed and t-CW excitation.

| | Short pulse [μJ cm$^{-2}$]$^{a)}$ ( FWHM [nm] ) | t-CW [W cm$^{-2}$] $^{b)}$ |
|---|---|---|
| ASE | 1.10 (4.68) | - |
| First-order DFB | 0.18 (0.61) | - |
| Second-order DFB | 0.91 (0.92) | 75.85 |
| Mixed-order DFB | 0.86 (0.47) | 72.28 |

In order to further clarify the CW laser behavior, polarization of the emitted light beam was examined[15]. The results shown in Figure 2.30a,b verified that a proper lasing operation takes place in DFB devices under CW photo-irradiation. When the stability was checked with the t-CW excitation, 1 wt.%-DCNP:BSBCz device had half-life of 2.85 and 3.15 min for second-order and mixed-order DFB resonators, respectively, at pumping power of 3.6 kW cm$^{-2}$. The laser emission stayed for about 5 min and then only PL is observed (Figure 2.30c).

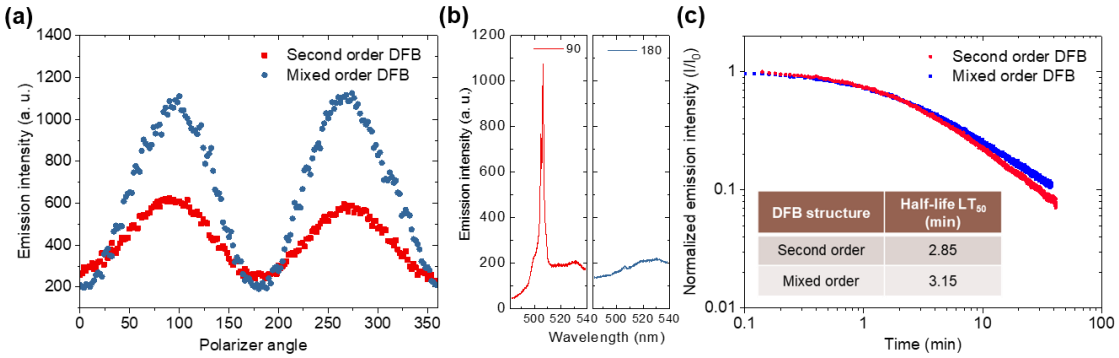


**Figure 2.30.** Optically pumped lasing under true-CW excitation ($\lambda_{ex}$ = 355 nm); polarization of output laser beam (excitation intensity = 3536 W cm$^{-2}$); (a) emission intensity as a function of polarization angle (b) respective emission spectra. Optical stability; (c) intensity/initial intensity versus operation-time (d-inset) table of estimated half-life.

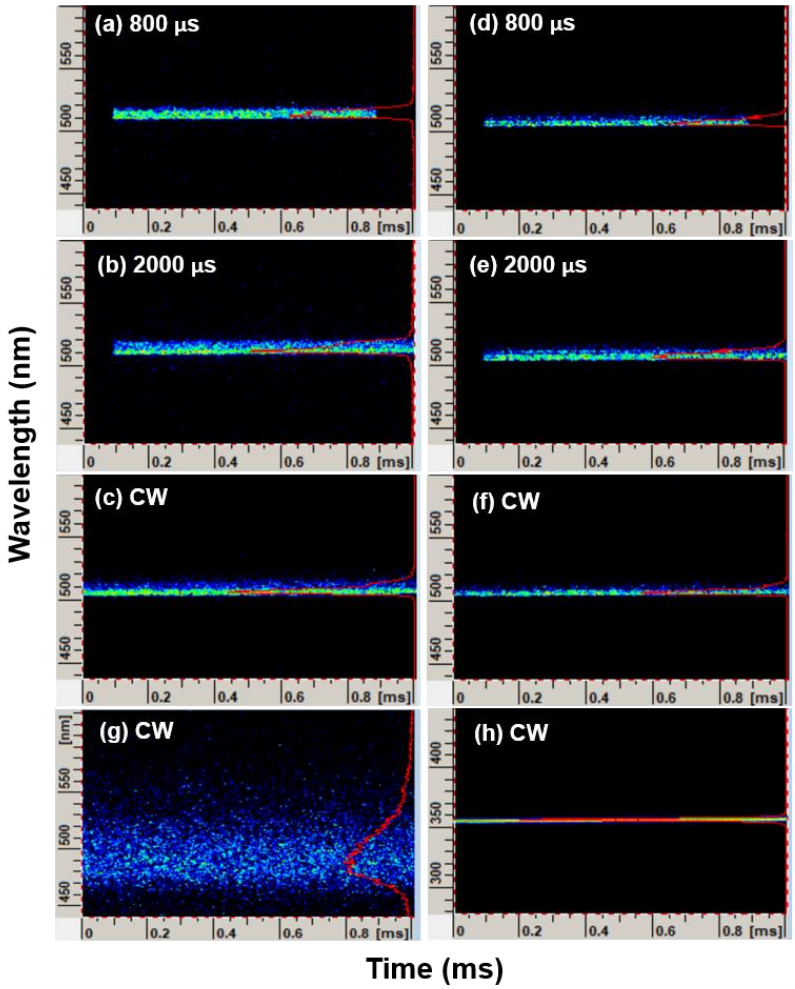


**Figure 2.31.** Streak camera images of long-pulsed (quasi-CW) and true-CW excitation ($\lambda_{ex}$ = 355 nm, excitation intensity = 3536 W cm$^{-2}$); second-order DFB (a) at 800 µs (b) at 2000 µs (c) at true CW, mixed-order DFB (d) at 800 µs (e) at 2000 µs (f) at true-CW, (g) outside of DFB at true CW and (h) excitation laser of true CW.

The fabricated DFB devices were further investigated for laser characteristics in the long-pulse excitation using same inorganic laser diode operating at 355 nm and an acousto-optic modulator (AOM). Results given in Figure 2.31 show the streak camera images of laser integrated over 100 pulses of the encapsulated 1 wt.%-DCNP:BSBCz films fabricated on second and mixed-order DFB structures at a pumping power of 3.6 kW $cm^{-2}$ under long excitation pulse widths of 800 µs or 2 ms or under t-CW excitation, respectively. Lasing thresholds for long pulsed excitation were ranged between 75 and 120 W $cm^{-2}$ (Figure 2.32) for both second and mixed-order DFB devices.

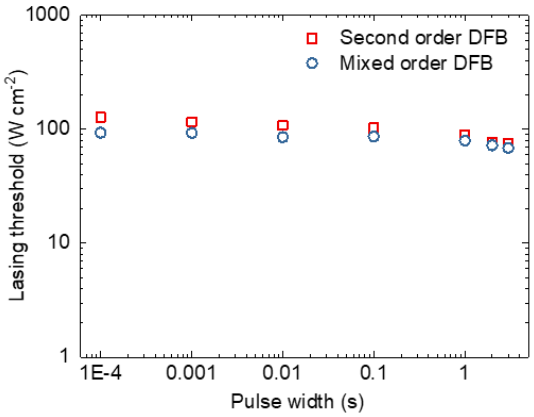


**Figure 2.32.** Lasing threshold versus pulse width when DFB devices excited with long pulsed (quasi-CW) excitation ($\lambda_{ex}$ = 355 nm).

The optically pumped lasers under t-CW operation mode remains a challenge because accumulation of long-lived triplet excitons via ISC could suppress further absorption of excitation laser and then reduce the exciton density that could undergo radiative emission. Moreover, spectral overlap between laser spectrum and triplet absorption spectrum may lead to excited state annihilation processes such as STA which hampers the light amplification in CW regime[11,16,1718]. However, interestingly, triplet exciton formation was not observable in a DCNP:BSBCz composite film under photo-excitation because of the effective removal of DCNP's triplets by BSBCz. Even if triplets may be formed on BSBCz molecules it is not a serious issue as its excited state absorption

has very small overlap with DCNP laser emission (Figure 2.21). Moreover, triplets formed on BSBCz molecules may diffused away from the DCNP emitter molecules and thereby distance between excitons might be larger, suppressing annihilation processes because the doping ratio is 1:99[19–22].

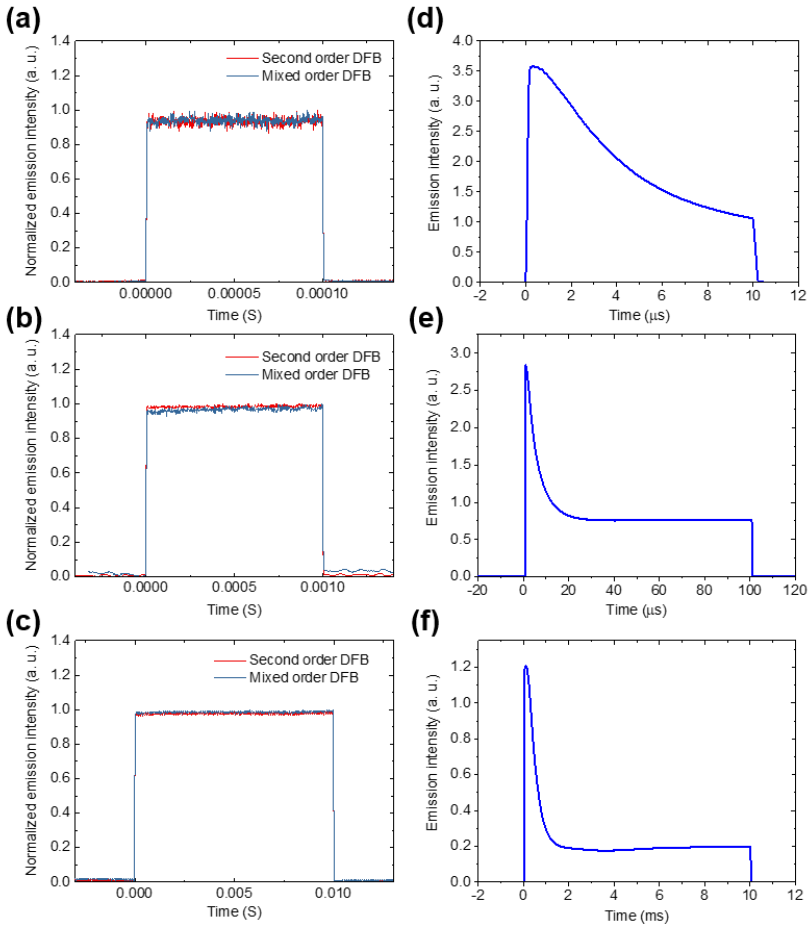


**Figure 2.33.** Transient emission of laser at long-pulsed excitation (temporal profiles) from DFB OSSLs of 1 wt.%-DCNP:BSBCz under (a) 0.1, (b) 1, and (c) 10 ms of optical pulse excitation. The excitation wavelength and the excitation intensity were 355 nm and 3536 W $cm^{-2}$, respectively. Transient emission of PL from a 1 wt.%-DCNP:CBP film under long-pulsed excitation (temporal profiles) of (d) 10 μs, (e) 100 μs, and (f) 10 ms ($\lambda_{ex}$ = 355 nm).

The temporal profiles of transient PL responses at long pulsed optical excitation in Figure 2.33a,b,c clearly shows that there is no quenching by triplet excited-states, i.e., STA, as the intensity of the PL stays the same after 0.1, 1, and 10 ms time scales of

irradiation[11,16,17,23,24]. The same study for a 1 wt.%-DCNP:CBP film shows serious suppression of PL by long lived triplet excitons due to STA (Figure 2.33d,e,f). These results suggest that triplet induced emission quenching such as STA is completely suppressed in a DCNP:BSBCz composite film which is promising for future applications of CW lasing.

## 2.4 Conclusion

In this Chapter, a new laser dye of DCNP was successfully combined with a BSBCz host, resulting in an ideal guest-host system which can scavenge triplet excitons efficiently from DCNP. The photo-physical studies suggested that the triplets formed on DCNP emitters are easily transferred to BSBCz host molecules, whose triplet absorption does not seriously overlap with the DCNP emission spectrum, thereby completely eliminating triplet-induced losses. Therefore, excited state annihilation processes such as STA and TTA are negligible in a DCNP:BSBCz film. DCNP-doped BSBCz films showed green emission with a high PL quantum yield of 83 %. Moreover, it was found that the performance of ASE with a threshold of 1.1 μJ $cm^{-2}$ and DFB laser with thresholds ranging from 0.18 to 0.91 μJ $cm^{-2}$ are promising for future electrically driven organic laser in green color regime. The removal of triplet excitons in the active region led to operate the laser devices under continuous-wave optical excitation, with a low threshold of 75 W $cm^{-2}$ and half-life of laser duration for 3 minutes which is highly promising for future applications of CW lasing.

## References

[1] N. Hashimoto, R. Umano, Y. Ochi, K. Shimahara, J. Nakamura, S. Mori, H. Ohta, Y. Watanabe, M. Hayashi, *J. Am. Chem. Soc.* **2018**, *140(6)*, 2046.

[2] H. Nakanotani, C. Adachi, S. Watanabe, R. Katoh, *Appl. Phys. Lett.* **2007**, *90*, 231109.

[3] A. S. D. Sandanayaka, T. Matsushima, F. Bencheikh, K. Yoshida, M. Inoue, T. Fujihara, K. Goushi, J. C. Ribierre, C. Adachi, *Sci. Adv.* **2017**, *3(4)*, e1602570.

[4] A. S. D. Sandanayaka, T. Matsushima, F. Bencheikh, S. Terakawa, W. J. Potscavage, C. Qin, T. Fujihara, K. Goushi, J. C. Ribierre, C. Adachi, *Appl. Phys. Express* **2019**, *12*, 061010.

[5] A. S. D. Sandanayaka, K. Yoshida, M. Inoue, C. Qin, K. Goushi, J. C. Ribierre, T. Matsushima, C. Adachi, *Adv. Opt. Mater.* **2016**, *4*, 834.

[6] V. G. Kozlov, G. Parthasarathy, P. E. Burrows, S. R. Forrest, Y. You, M. E. Thompson, *Appl. Phys. Lett.* **1998**, *72*, 144.

[7] V. K. Praveen, S. J. George, R. Varghese, C. Vijayakumar, A. Ajayaghosh, *J. Am. Chem. Soc.* **2006**, *128*, 7542.

[8] T. Matsushima, S. Yoshida, K. Inada, Y. Esaki, T. Fukunaga, H. Mieno, N. Nakamura, F. Bencheikh, M. R. Leyden, R. Komatsu, C. Qin, A. S. D. Sandanayaka, C. Adachi, *Adv. Funct. Mater.* **2019**, *29*, 1807148.

[9] T. Aimono, Y. Kawamura, K. Goushi, H. Yamamoto, H. Sasabe, C. Adachi, *Appl. Phys. Lett.* **2005**, *86*, 071110.

[10] G. Henderson, *J. Chem. Educ.* **1977**, *54(1)*, 57.

[11] M. Lehnhardt, T. Riedl, T. Weimann, W. Kowalsky, *Phys. Rev. B* **2010**, *81*, 165206.

[12] S. Riechel, C. Kallinger, U. Lemmer, J. Feldmann, A. Gombert, V. Wittwer, U. Scherf, *Appl. Phys. Lett.* **2000**, *77*, 2310.

[13] M. Goossens, A. Ruseckas, G. A. Turnbull, I. D. W. Samuel, *Appl. Phys. Lett.* **2004**, *85*, 31.

[14] K. Yoshida, T. Matsushima, Y. Shiihara, H. Kuwae, J. Mizuno, C. Adachi, *J. Appl. Phys.* **2017**, *121*, 195503.

[15] F. Chen, D. Gindre, J.-M. Nunzi, *Opt. Express* **2008**, *16(21)*, 16746.

[16] Y. Zhang, S. R. Forrest, *Phys. Rev. B* **2011**, *84*, 241301.

[17] T. G. Pavlopoulos, *Prog. Quantum Electron.* **2002**, *26*, 193.

[18] E. B. Namdas, A. Ruseckas, I. D. W. Samuel, S. C. Lo, P. L. Burn, *Appl. Phys. Lett.* **2005**, *86*, 091104.

[19] M. Inoue, T. Matsushima, C. Adachi, *Appl. Phys. Lett.* **2016**, *108,* 133302.

[20] M. Yokota, O. Tanimoto, *J. Phys. Soc. Japn* **1967**, *22*, 779.

[21] S. M. Menke, W. A. Luhman, R. J. Holmes, *Nat. Mater.* **2013**, *12*, 152.

[22] X. Liu, Y. Zhang, S. R. Forrest, *Phys. Rev. B* **2014**, *90*, 085201.

[23] M. Inoue, T. Matsushima, H. Nakanotani, C. Adachi, *Chem. Phys. Lett.* **2015**, *624*, 43.

[24] L. Zhao, M. Inoue, K. Yoshida, A. S. D. Sandanayaka, J. H. Kim, J. C. Ribierre, C. Adachi, *IEEE J. Sel. Top. Quantum Electron.* **2016**, *22*, 26.

# Chapter 3

## Suppression of external quantum efficiency rolloff in organic light-emitting diodes by scavenging triplet excitons

## 3.1 Introduction and advantage of using a triplet scavenging host material for EL

As I explained in Chapter 1, a larger number of triplets are formed in OLEDs when compared with optical excitation. Therefore, triplet-induced quenching like STA is more serious, leading to serious efficiency roll-off at high current densities in OLEDs. In Chapter 2, I found the proposed triplet scavenging method works properly under optical excitation. Therefore, to demonstrate the effectiveness of the triplet scavenging method for electrical excitation, i.e., suppressing STA, I investigated how this method can suppress efficiency roll-off in the OLEDs having single layer device architecture[1–4].

In conventional device architectures for PHOLEDs and TADF-OLEDs, the use of host materials that can confine triplet excitons were mandatory for high efficiencies[5-15]. In the case of using CBP as the host and DCNP as the emitter, the singlet excitons of CBP could transfer to the guest molecules via FRET while the CBP triplet excitons may transfer via DET (Figure 3.1a). Therefore, at higher current densities, DCNP guest molecules will accumulate triplet excitons, thereby suppressing the rate of singlet exciton formation[8,11,16].

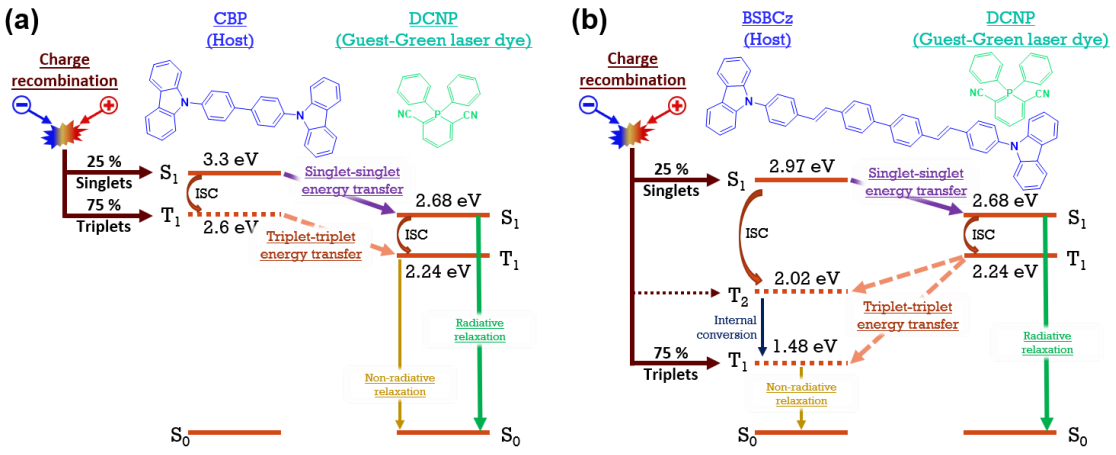


**Figure 3.1.** Jablonski energy diagram of guest-host systems. Energy transfer processes under electrical excitation when the guest material is DCNP and the host material is (a) CBP or (b) BSBCz.

However, interestingly, when the triplet level of host molecules is lower than the triplet level of guest, it is impossible to transfer triplets from host to guest molecules and thereby the triplets stay on the host molecules themselves (Figure 3.1b)[17–19]. In addition, whenever triplet excitons are formed on guest emitter molecules via ISC and direct exciton formation at the emitter molecules, then those triplet excitons will transfer to the host molecules via DET mechanism[20]. In this Chapter, we used a 1 wt.%-DCNP:BSBCz system which corresponds to the molar ratio of 1:43 for DCNP:BSBCz. Thus, it is very easy to undergo this reverse DET because the molar ratio of host molecules is much higher than that of guest molecules in the guest-host system. Therefore, it is obvious that guest emitter molecules are always free to accept FRET from host's singlets and thereby emitter singlet exciton formation and relaxation cycles, i.e., the singlet exciton formation frequency is faster than the usual triplet associated case. Another advantage of using this type of the low doping ratio is that triplet excitons formed on neighboring host molecules may diffused to another host molecule and migrate away from the emitter molecule which could help to suppress STA[21]. Moreover, triplet excitons are almost formed on host molecules and thereby avoiding the triplet induced degradation of guest emitter molecules which may aid in improving device stability. Thus, BSBCz fulfils all the intrinsic requirements as the efficient triplet scavenging host for OLEDs and OSLDs.

## 3.2 Experimental

***Estimation of frontier orbital energy levels***

To estimate the energy level of HOMO of all materials, 100 nm thin films of pristine BSBCz, DCNP and 1 wt.%-DCNP:BSBCz were vacuum-deposited on pre-cleaned ITO-coated glass substrates. The HOMO energy levels were determined using photoelectron yield spectroscopy (AC-3, Riken-Keiki) in neat films, and then the LUMO energy levels were estimated by subtracting the optical energy gap ($E_g$) from the

measured HOMO energies. In the case of the $E_g$ values were determined from the onset of the PL spectra of neat films.

***Variable angle spectroscopic ellipsometry (VASE) measurement***

In order to estimate a molecular orientation of BSBCz, Spectra of refractive index *n* and extinction coefficient *k* of vacuum deposited neat and 1 wt.%-DCNP doped films of BSBCz were obtained using variable angle spectroscopic ellipsometer (M-2000, J.A. Woollam). The measurement was performed on the 100 nm thick films deposited on bare Si substrate. The incident angle was varied from 45° to 75° with a 5° step increment and the spectral measurement range was set to 245–1000 nm. BSBCz films are known to show anisotropy along the directions parallel and perpendicular to the substrate plane because of the orientation of molecules. Therefore, VASE results of BSBCz films were fitted using an uniaxial anisotropic optical model considering molecular anisotropy, and the orientation order parameter *S* was calculated using following Eq. 3.1[22–24];

$$S = \frac{k_z - k_x}{k_z + 2k_x} \quad \text{(Eq. 3.1)}$$

where $k_x$ and $k_z$ are the extinction coefficients in the directions parallel and perpendicular to the substrate, respectively. It should be noted that the same optical model was used for neat and doped films, assuming that the doping concentration of DCNP is sufficiently small (1 wt.%).

***Single-carrier devices and OLED fabrication***

To fabricate an electron only device (EOD), hole only device (HOD) and OLEDs, all organic and metal layers were vacuum-deposited on clean ITO-coated glass substrates under a pressure of $10^{-4}$ Pa. The deposition rates were 1.0 Å $s^{-1}$ for Cs doped films of BSBCz and CBP, 2.5 Å $s^{-1}$ for DCNP doped films of BSBCz and CBP, 0.3 Å $s^{-1}$ for $MoO_3$, and 1.0 Å $s^{-1}$ for Al. The completed OLEDs were directly transferred into a nitrogen filled glovebox and encapsulated using a glass cap and an UV curing epoxy resin.

***OLED characterization***

The current density-voltage (*J-V*), external quantum efficiency-current density curves and EL spectra at DC operation were measured using an external quantum efficiency measurement system (C9920-12, Hamamatsu Photonics). Pulsed voltage operation were measured using rectangular pulses with a pulse width of 400 ns, repetition frequency of 1 kHz, and varying peak voltages were applied to the devices at ambient temperature using a pulse generator (NF, WF1945) while applied voltage ($V_{CH1}$) was monitored on a multichannel oscilloscope (MSO6104A, Agilent Technologies). To measure current flow through the device a 51.4 Ω resistor was connected in serial connection to the OLED and voltage across the resistor ($V_{CH2}$) was monitored on the oscilloscope (Figure 3.2). Therefore, in-situ voltage across the OLED device can be reported as $V_{CH1} - V_{CH2}$ based on voltage division rule (Figure 3.2).

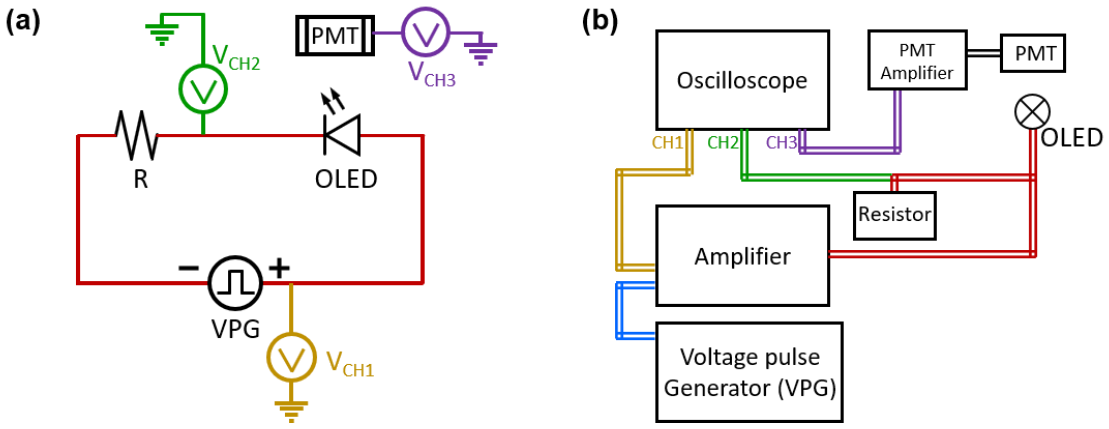


**Figure 3.2.** (a) Circuit diagram of our transient EL measurement setup using square pulsed voltage, (b) the same setup as a schematic of showing BNC cable connections.

***Transient EL at long pulsed voltage***

Long-pulsed voltage was generated same as the short-pulsed voltage measurement explain in OLED characterization. The EL intensity from OLED was recorded using a photomultiplier tube (PMT) (C9525-02, Hamamatsu Photonics) for the measurement of temporal emission profile. Driving square wave voltage signal ($V_{CH1}$),

voltage across resistor ($V_{CH2}$) and PMT response ($V_{CH3}$) were monitored on a multichannel oscilloscope (MSO6104A, Agilent Technologies). The circuit diagram and schematic of BNC cable connection is depicted in Figure 3.2.

## 3.3 Results and discussion

### 3.3.1 Frontier molecular orbitals and charge carrier balance in thin film diode

The HOMO levels of BSBCz and DCNP were −5.9±0.1 and −6.0±0.1 eV, respectively (Figure 3.3a), whereas the LUMO levels of those were estimated to be −3.1±0.1 and −3.5±0.1 eV, respectively. It can be assumed that charge transport is mainly dominated by the host molecule of BSBCz, leading to similar charge balance as the reference device[2]. In order to study whether the charge transport channel is affected by molecular orientation of BSBCz[22,23], the VASE measurements were conducted. The obtained *n*-*k* spectra are shown in Figure 3.3b,c. Here, $k_x$ and $k_z$ values at a wavelength of 370.61 nm were used for the calculation of the orientation order parameter *S* value, which corresponds to the π-π* transition of BSBCz. The molecular orientation discussed here indicates the orientation of the transition dipole moment which is almost along the molecular long axis of BSBCz[24]. The calculated *S* values of neat and doped films were −0.374 and −0.381, respectively, which are similar to our previous report[24] and it indicates that the DCNP doping does not change the molecular orientation in films. Although molecular orientation is one of the critical factors influencing charge carrier transport in organic semiconductor films[22–24], this effect is negligible in the comparison of our neat and doped films.

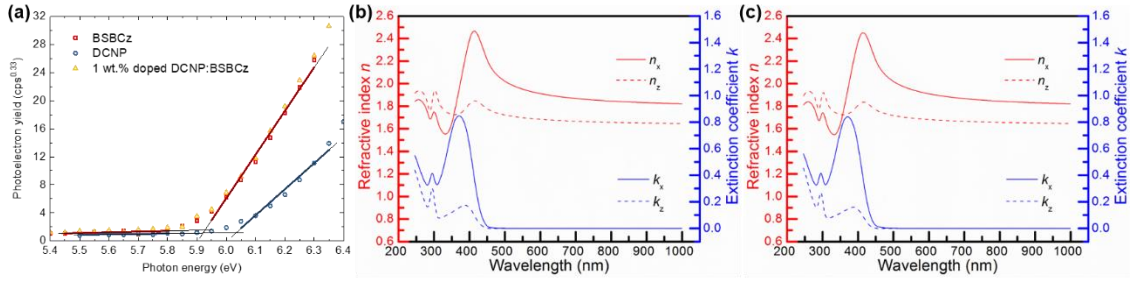


**Figure 3.3.** (a) Photoelectron yield spectra of 100 nm-thick films of neat BSBCz, neat DCNP and 1 wt.%-DCNP:BSBCz. Refractive indices and extinction coefficients of (b) BSBCz neat films (100 nm) and (c) 1 wt.%-DCNP:BSBCz films (100 nm), which were obtained using VASE and a uniaxial anisotropic fitting model[8].

Apart from the intrinsic properties of materials used for OLEDs, it is very important to consider about the device architecture in concern to other EQE governing factors of OLEDs. In conventional OLED architectures, multi-layer interfaces play important role in balancing hole injection and electron injection which is one of the crucial factors for exciton formation efficiency, thereby it is directly related to the internal quantum yield. However, detrimentally there is possibility to occur polaron absorption at the electron transport layers (ETL) and hole transport layers (HTL) which may quench the light output[4,25], especially considering about organic semiconductor laser diodes where the light travels back and forth within the resonator structure for high optical feedback. Particularly, at high current densities, the polaron densities in ETLs and HTLs are very high, inducing rapid efficiency rolloff[26,27]. Therefore, using ETLs or HTLs will hamper the optical gain unless the polaron absorption spectra of both ETL and HTL materials are not overlapping with laser emission spectra. Therefore, easiest way to avoid this complex material selection for ETLs and HTLs is using single layer architecture of OLEDs as the first generation of OSLDs[2]. Thus, we need to pay attention only about the polaron absorption of the EML material itself. Nevertheless, in order to obtain high performance from the single layer architecture, well balanced hole and electron mobilities

of an organic layer are strongly required. Hence, for the optimum performance of single layer OLEDs, intrinsic properties of the host molecules play a very important role.

To investigate the carrier transport properties of DCNP:BSBCz, a EOD and HOD was fabricated with the structures of glass substrate / ITO (30 nm) / $MoO_3$ (10 nm) / 1 wt.%-DCNP:BSBCz (200 nm) / $MoO_3$ (10 nm) / Al (100 nm) and glass substrate / ITO (30 nm) / 20 wt.%-Cs:BSBCz (30 nm) / 1 wt.%-DCNP:BSBCz (180 nm) / Cs (30 nm) / Al (100 nm) (Figure 3.4a). Current density–voltage curves of the HODs and EODs were measured under direct current (DC) and as well as pulse operation. Notably, the current density–voltage curves of the HODs and EODs almost overlapped relative to each other in the whole voltage range (Figure 3.4b). This indicates that 1 wt.%-DCNP-doped BSBCz films have well balanced hole and electron mobilities, leading to higher efficiency.

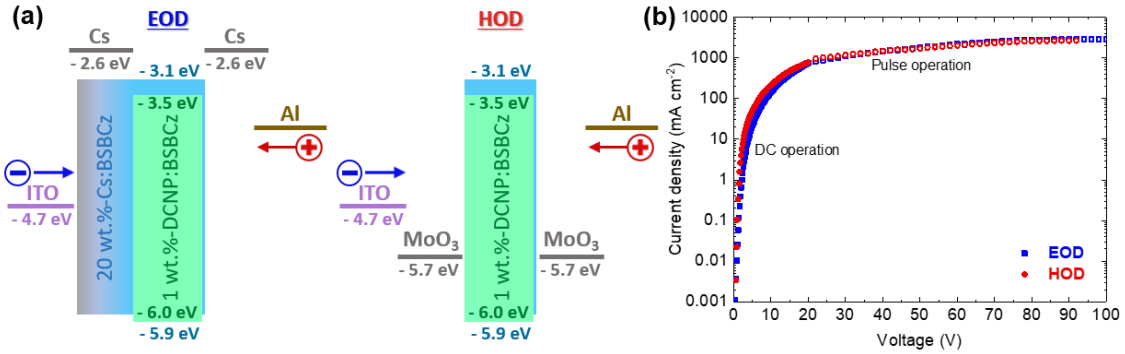


**Figure 3.4.** Evaluation of charge transport properties. (a) Energy level diagrams for the EODs and HODs of single layer devices. (b) current density−voltage (*J*−*V*) curves of EODs and HODs.

### 3.3.2 Electrical and electroluminescent properties

Furthermore, EL properties of DCNP was studied using separately CBP and BSBCz as the host with single layer OLEDs. Device A consists with a glass substrate / ITO (30 nm) / Cs (10 nm) / 20 wt.%-Cs:CBP (30 nm) / 1 wt.%-DCNP:CBP (180 nm) / $MoO_3$ (10nm) / Al (100 nm), device B consists with a glass substrate / ITO (30 nm) /

20 wt.%-Cs:BSBCz (30 nm) / BSBCz (180 nm) / $MoO_3$ (10 nm) / Al (100 nm) and device C consists with a glass substrate / ITO (30 nm) / 20 wt.%-Cs:BSBCz (30 nm) / 1 wt.%-DCNP:BSBCz (180 nm) / $MoO_3$ (10 nm) / Al (100 nm).

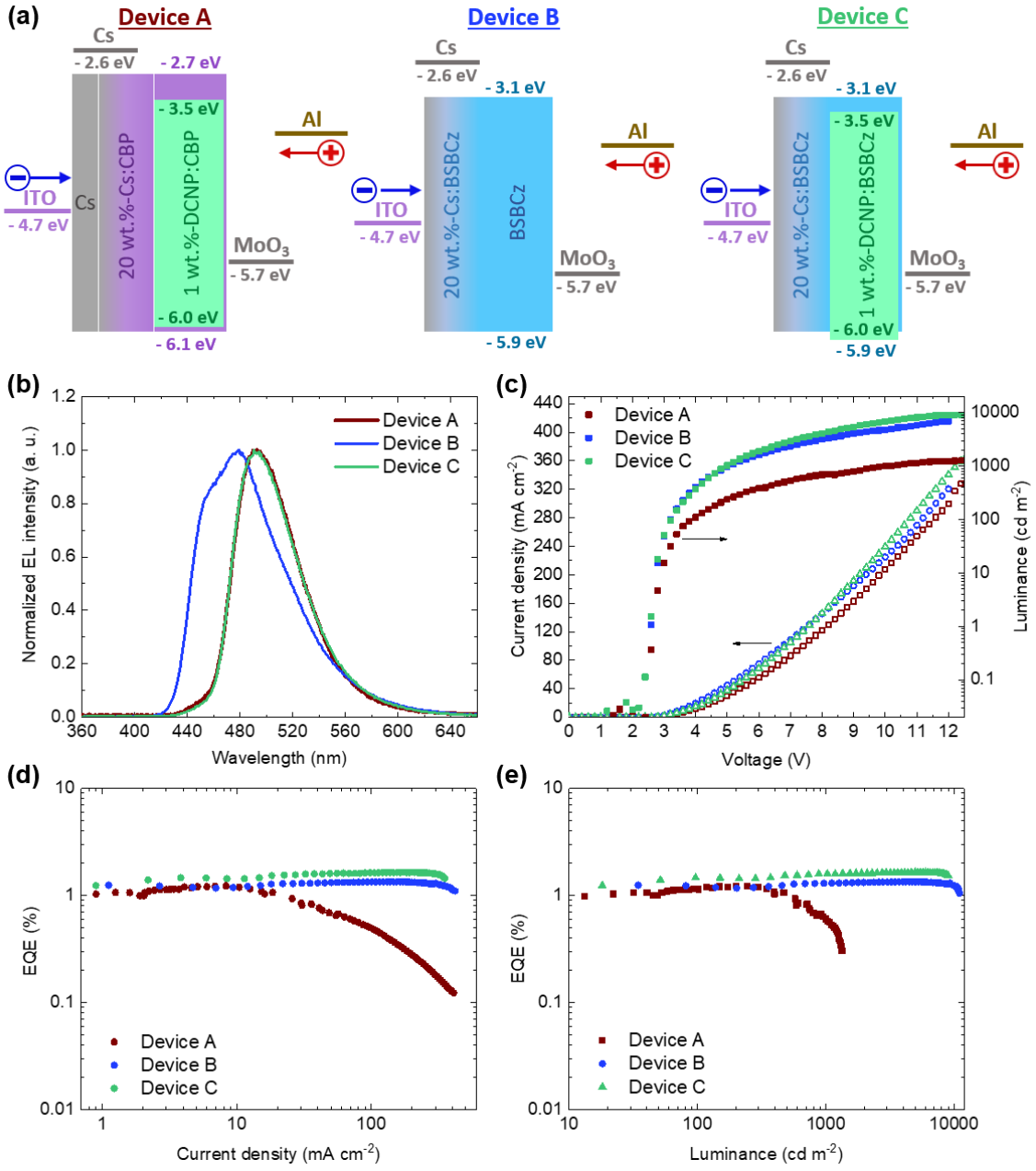


**Figure 3.5.** Comparison of OLED performance. (a) Energy level diagrams for the OLEDs which were used to evaluate triplet scavenging property of BSBCz as the host (Device A, B and C). (b) EL spectra. (c) current density−voltage and luminance−voltage curves. (d) EQE−current density curves (e) EQE−luminance curves.

The energy level diagrams of the OLEDs are shown in Figure 3.5a. Doping of

Cs into BSBCz or CBP and the insertion of $MoO_3$ between organic layer and Al facilitate electron and hole injection from electrodes, respectively. Even though, the relatively shallower HOMO level of BSBCz and deeper LUMO level of DCNP may create an exciplex, we observed no exciplex emission because the EL spectra are exactly similar as the DCNP PL spectra (Figure 2.9). Considering the frontier orbital energy levels and the very low doping concentration of DCNP in BSBCz (1 wt.%), it would be reasonable that charge recombination mainly occurs on CBP or BSBCz host molecules. Thereafter, the formed singlet exciton energy will be transferred into DCNP via FRET. As shown in Figure 3.5b, both DCNP doped devices showed similar emission spectra to the PL of DCNP without yielding additional shoulder peaks from residual host emission, which suggests almost perfect FRET from host to guest.

In the case of CBP host device (Device A), the luminance output is lower (Figure 3.5c) and efficiency rolloff is higher at larger current densities (Figure 3.5d,e) due to accumulation of triplet excitons which causes STA. In the case of BSBCz host device (Device C), triplet excitons formed on BSBCz molecules would not transferrable and hence it would be relaxed via nonradiative relaxation pathways as clarified earlier in Figure 3.1. Faster nonradiative relaxation of BSBCz triplet excitons is explained in section 2.3.2, as the triplet exciton lifetime is in nano-second range[28]. Advantageously, due to suppressed STA in BSBCz based devices (Devices B and C), efficiency rolloff suppressed until the current density is 500 mA $cm^{-2}$, where after the device starts to breakdown due to joule heating under DC operation (Figure 3.5d,e). EQE of an OLED can be expressed as,

$$\text{EQE}\ \% = \gamma \times \beta \times \phi \times \eta \times 100\ \% \qquad \text{(Eq. 3.1)}$$

where $\gamma$ = charge recombination efficiency, $\beta$ = exciton formation probability, $\phi$ = PL quantum yield, $\eta$ = light out-coupling efficiency. Based on the results of EOD and HOD,

well balanced electron and hole transport is expected in all devices, hence, γ is expected to be closer to 1.0. In 1 wt.%-DCNP:BSBCz host-guest matrix, PLQY is 0.83 and singlet exciton formation probability should be 0.25 according to spin statistics under electrical excitation. Therefore, if light outcoupling from the device is assumed to be 0.2, then the device should exhibit maximum external quantum efficiency ($EQE_{max}$) of 4.15 % based on Eq. 3.1. However, in the experimental conditions, it shows (1.4±0.1 %), (1.4±0.1 %), and (1.5±0.1 %) $EQE_{max}$ for device A, B, and C, respectively (Figure 3.5d). Detrimentally, the single layer devices do not have an electron blocking layer or a hole blocking layer to confine charge recombination in the emissive layer which is typical in multilayer device architecture. Therefore, some of electrons and holes could reach counter electrodes without recombination, leading to low efficiency in the single layer devices, although balanced carrier mobilities were observed. However, advantageously for OSLDs, this single-layer device architecture is very effective for suppressing the efficiency-rolloff, especially at higher current densities[2].

### 3.3.3 Suppressed EL quenching with long lived excitons

As shown in Figure 3.6a,b, when DCNP was doped in a CBP host, it shows clear quenching of singlet emission (EL intensities) by long lived triplet excitons with time when OLEDs are driven at 50 μs square pulses. At low current densities, EL was rising because the triplet induced EL quenching was not in progress. However, when the devices are operated at higher current densities, the accumulation of triplets take place and then annihilation processes with singlet excitons undergoes, thereby decreasing EL intensity by time.

On the other hand, very interestingly, devices with 1 wt.%-DCNP:BSBCz showed complete suppression of EL-STA when driven at 50 μs square pulses even until 10 A $cm^{-2}$ very high current density (Figure 3.6c,d). This is evidences by no decrease in

EL intensity. Major reason is that triplet scavenging mechanism realized using BSBCz as the host instead of CBP, led to the complete removal of triplets from the emitter molecules, thereby completely avoiding the emitter-emitter STA. The other reasons are negligible overlap of the DCNP emission spectrum with the BSBCz triplet absorption spectrum which was explained in Chapter 2.

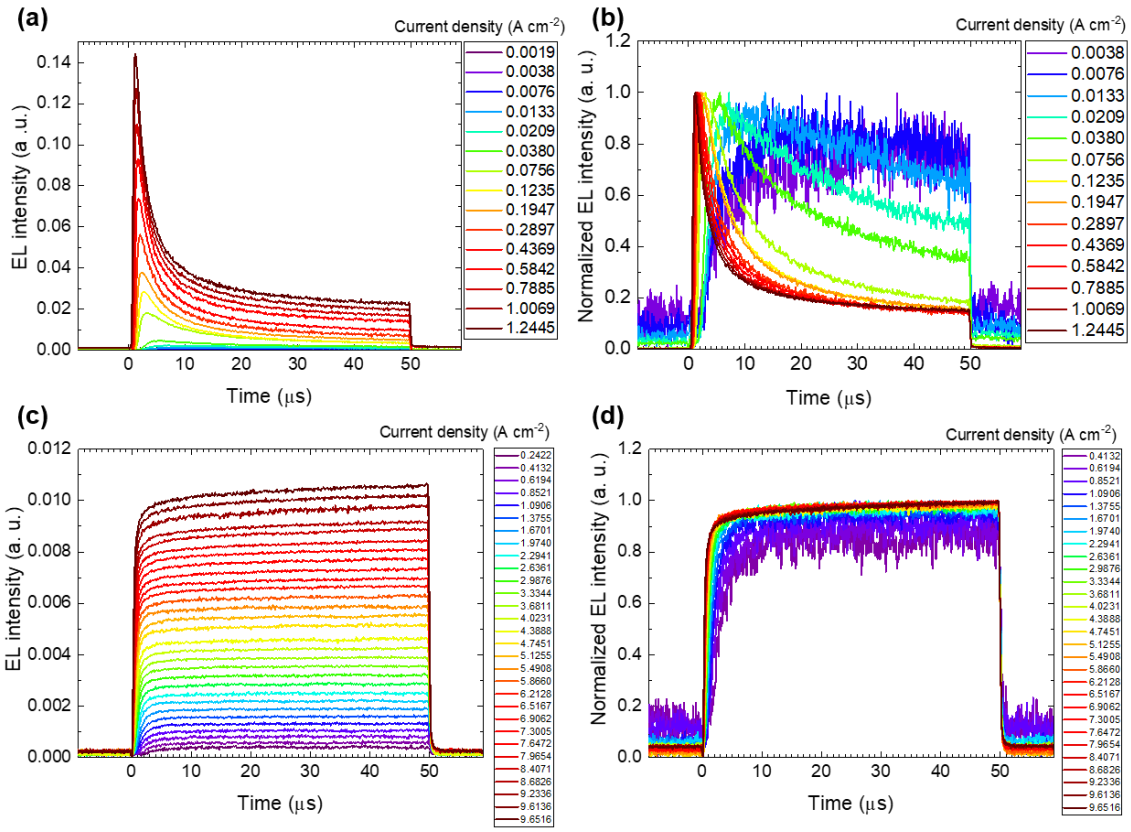


**Figure 3.6.** Transient EL responses of OLEDs. (a,b) when the host is CBP for device A or (c,d) when the host is BSBCz for device C, which were measured at different current densities with a pulse width of 50 μs. The EL intensities of (a and c) are normalized in (b and d) respectively to make it easy to see the response shapes.

Faster triplet relaxation lifetime of BSBCz became an additional advantage[28] (Figure 2.16) to complete suppression of emitter-host STA. In order to find out triplet accumulation at longer pulse width, tests were carried out for transient EL at 100, 200, 500 μs and even up to 1 ms square pulses driven until 10 A cm$^{-2}$ current density (Figure 3.7). Surprisingly, it showed no EL quenching even at 1 ms long pulse width and

10 A $cm^{-2}$ very high current density. Thus, as expected by the energy diagrams and all other phenomenon explained in the introduction section, complete suppression of EL-STA was found by adding DCNP into BSBCz. This result is highly promising for prospective OSLD devices in order to reach high optical gain at higher current densities and for better device stability.

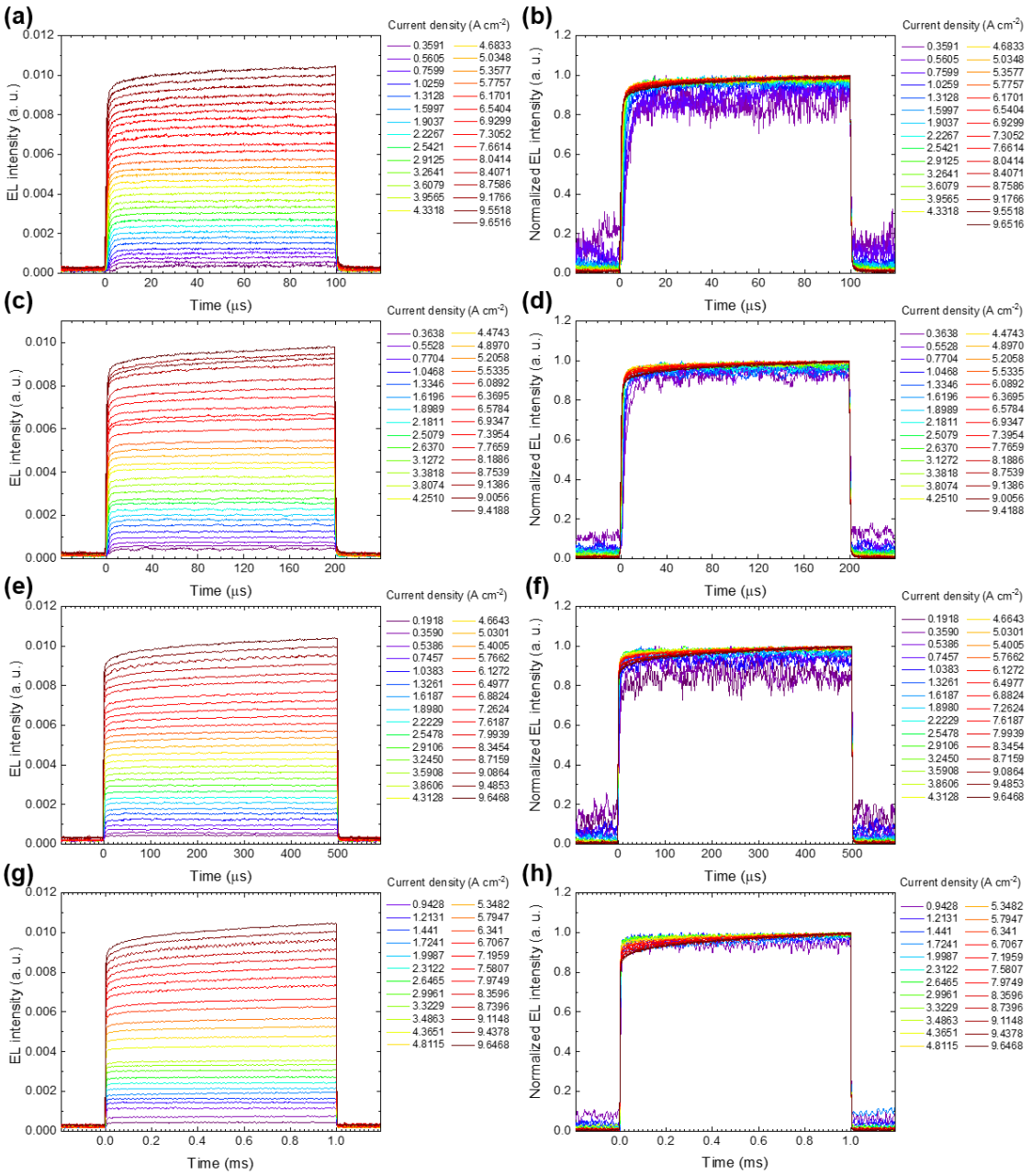


**Figure 3.7.** Transient EL responses of OLEDs with the BSBCz host layer. Temporal profiles of EL intensity when the pulse widths were (a,b) 100 μs, (c,d) 200 μs, (e,f) 500 μs, (g,h) 1 ms. The EL intensities of (a,c,e and g) were normalized in (b,d,f and h) respectively to make it easy to see the response shapes.

### 3.4 Conclusion

Objective of this Chapter is to demonstrate the effectiveness of my triplet scavenging material for suppressing EL-STA and efficiency rolloff at higher current densities of OLEDs. Triplet scavenging mechanism was successfully realized by using a $\lambda^5$-Phosphinine fluorescent emitter and BSBCz as a guest-host matrix. Doping DCNP into BSBCz yielded similar EQE as non-doped devices. It showed clear STA even at 50 μs pulsed voltage when CBP was used as the host, while on the other hand using BSBCz as the host showed no EL quenching by STA, SPA or any other manner from 50 μs to 1 ms long pulse width until the very high current density of 10 A $cm^{-2}$. The suppressed STA and suppressed efficiency rolloff for DCNP:BSBCz-based devices open a way to the fabrication of OSLDs with high performance.

### References


[1] C. Murawski, K. Leo, M. C. Gather, *Adv. Mater.* **2013**, *25*, 6801.

[2] A. S. D. Sandanayaka, T. Matsushima, F. Bencheikh, S. Terakawa, W. J. Potscavage, C. Qin, T. Fujihara, K. Goushi, J. C. Ribierre, C. Adachi, *Appl. Phys. Express* **2019**, *12*, 061010.

[3] F. Bencheikh, A. S. D. Sandanayaka, T. Fukunaga, T. Matsushima, C. Adachi, **2019**, *126*, 185501.

[4] Y. Setoguchi, C. Adachi, *J. Appl. Phys.* **2010**, *108,* 064516.

[5] F. C. Chen, S. C. Chang, G. He, S. Pyo, Y. Yang, M. Kurotaki, J. Kido, *J. Polym. Sci. Part B Polym. Phys.* **2003**, *41*, 2681.

[6] A. Ligthart, X. de Vries, L. Zhang, M. C. W. M. Pols, P. A. Bobbert, H. van Eersel, R. Coehoorn, *Adv. Funct. Mater.* **2018**, *28(52)*, 1804618.

[7] S. Gong, X. He, Y. Chen, Z. Jiang, C. Zhong, D. Ma, J. Qin, C. Yang, *J. Mater. Chem.* **2012**, *22*, 2894.

[8] Y. J. Pu, G. Nakata, F. Satoh, H. Sasabe, D. Yokoyama, J. Kido, *Adv. Mater.* **2012**, *24*, 1765.

[9] K. Hayashi, H. Nakanotani, M. Inoue, K. Yoshida, O. Mikhnenko, T. Q. Nguyen, C. Adachi, *Appl. Phys. Lett.* **2015**, *106*, 093301.

[10] M. A. Baldo, R. J. Holmes, S. R. Forrest, *Phys. Rev. B - Condens. Matter Mater. Phys.* **2002**, *66*, 353211.

[11] S. Tokito, T. Tsuzuki, F. Sato, T. Iijima, *Curr. Appl. Phys.* **2005**, *5*, 331.
[12] J. Lee, N. Chopra, S. H. Eom, Y. Zheng, J. Xue, F. So, J. Shi, *Appl. Phys. Lett.* **2008**, *93*, 123306.
[13] I. Tanaka, Y. Tabata, S. Tokito, *Phys. Rev. B* **2005**, *71*, 205207.
[14] H. Nakanotani, K. Masui, J. Nishide, T. Shibata, C. Adachi, *Sci. Rep.* **2013**, *3*, 2127.
[15] A. Ligthart, X. de Vries, P. A. Bobbert, R. Coehoorn, *Org. Electron.* **2020**, *77*, 105510.
[16] V. Jankus, C. Winscom, A. P. Monkman, *J. Chem. Phys.* **2009**, *130*, 074501.
[17] S. Tokito, I. Tanaka, *Electrochemistry* **2007**, *76*, 24.
[18] Y. Zhang, M. Slootsky, S. R. Forrest, in *Conference on Lasers and Electro-Optics 2012, OSA Technical Digest* **2012**, paper CW1L.6.
[19] L. Zhao, M. Inoue, K. Yoshida, A. S. D. Sandanayaka, J. H. Kim, J. C. Ribierre, C. Adachi, *IEEE J. Sel. Top. Quantum Electron.* **2016**, *22*, 26.
[20] Y. Zhang, S. R. Forrest, *Phys. Rev. B* **2011**, *84*, 241301.
[21] E. B. Namdas, A. Ruseckas, I. D. W. Samuel, S. C. Lo, P. L. Burn, *Appl. Phys. Lett.* **2005**, *86*, 091104.
[22] D. Yokohama, Y. Setoguchi, A. Sakaguchi, M. Suzuki, C. Adachi, *Adv. Funct. Mater.* **2010**, *20*, 386.
[23] D. Yokoyama, *J. Mater. Chem.* **2011**, *21*, 19187.
[24] D. Yokoyama, A. Sakaguchi, M. Suzuki, C. Adachi, *Org. Electron. physics, Mater. Appl.* **2009**, *10*, 127.
[25] D. Zhao, H. P. Loebl, *Org. Electron.* **2015**, *24*, 147.
[26] S. Reineke, K. Walzer, K. Leo, *Phys. Rev. B* **2007**, *75*, 125328.
[27] D. Kasemann, R. Brückner, H. Fröb, K. Leo, *Phys. Rev. B* **2011**, *84*, 115208.
[28] Y. Oyama, M. Mamada, A. Shukla, E. G. Moore, S.-C. Lo, E. B. Namdas, C. Adachi, *ACS Mater. Lett.* **2020**, *2*, 161.

# Chapter 4

## Summary and perspectives

## 4.1 Summary of all Chapters

In this thesis, I focused on a triplet scavenging guest-host system having a unique lasing material of DCNP aimed for efficient and stable lasing.

In **Chapter 2**, a novel laser material, DCNP, was synthesized and dispersed into a BSBCz host layer. Optical properties of this guest-host matrix were discussed and experimentally evaluated in detail with the extensive photophysical assessment such as triplet scavenging capability, ASE, lasing at short pulsed excitation, lasing at CW excitation, and suppression of STA at long pulsed optical excitation. The optically driven lasing properties were further verified with monochromaticity and polarization of output beam, far-field and near-field interference patterns, and lifetime of excitons.

In **Chapter 3**, based on the excellent optical properties of the guest-host matrix, the experiment was extended to evaluate electrical and EL properties. Single layer OLEDs were optimized for obtaining perfect charge balance and 3 types of OLEDs were compared to clarify the triplet scavenging capability of BSBCz as a host material. Even though 75 % triplet excitons were generated under electrical excitation, the device with the well-controlled material combination showed the complete suppression of STA, i.e., no efficiency roll-off at high current densities. More interestingly, in the transient EL, it showed complete suppression of EL quenching even under the condition of 1 ms long pulses with 10 A $cm^{-2}$ current densities.

## 4.2 Future perspectives

### 4.2.1 From OLED to OSLD

Based on the results explained in Chapters 2 and 3, it has been clarified that the DCNP:BSBCz guest-host matrix can effectively scavenge triplet excitons, showing t-CW lasing under optical excitation, and completely suppress STA and efficiency rolloff in OLEDs under electrical excitation. In fact, this unique guest-host system is promising for

current driven OSLDs and I fabricated devices having OLED architecture combined with the DFB structures (2nd order and mixed order) on ITO[1] (Figure 4.1).

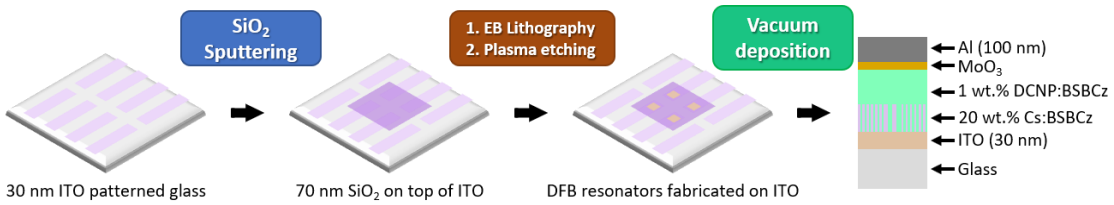


**Figure 4.1.** Schematic procedure of DFB-OLED fabrication.

As shown in Figure 4.2a, the EQEs of both second order and mixed order DFB-OLEDs are slightly higher (~2.0 %) than that of reference OLED (~1.5 %) and the DFB-OLEDs showed the significant spectral narrowing (Figure 4.2b,c)[2]. The DFB-OLED devices also showed very clear polarization along the DFB axis while the EL from reference OLEDs does not show polarization (Figure 4.2d). As shown in Figure 4.2e, the EL spectra consisted of two components; spectrally narrowed monochromatic emission with the plane-polarized emission, and spectrally broad and non-polarized emission.

Interestingly, it is possible to observe beams emerging out from the DFB-OLEDs by simply placing an illumination paper in front of the devices or take a photograph of the beams by using water vapor mist created from liquid nitrogen (the inset of Figure 4.2a). However, both DFB-OLEDs did not show clear threshold of light amplification in the plot of EL intensity vs current density up to 20 A $cm^{-2}$. Major reasons might be the current density is below the threshold or some defects in the DFB structures[3] or a shift of charge recombination zone to out-side of the DFB structure. Thus, future works are planned and in progress upon two different approaches to reach practical OSLD; optimizing the DFB-OLED architecture and development of laser gain medium.

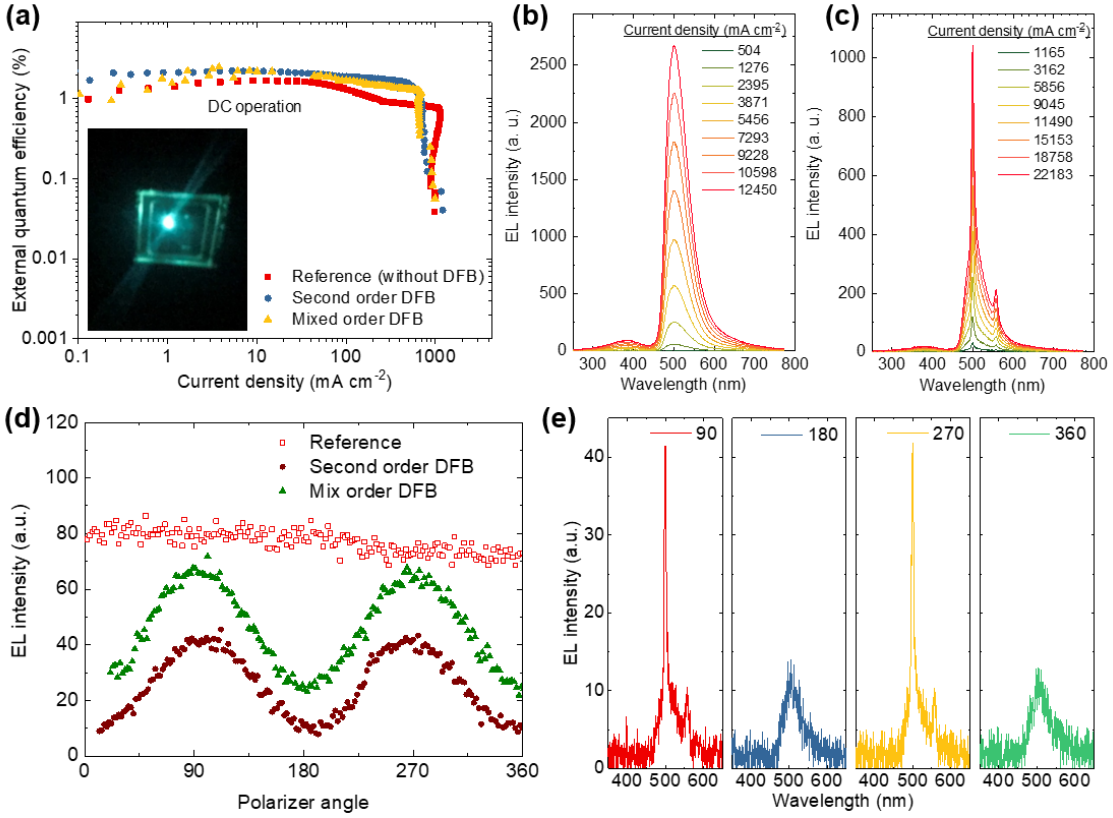


**Figure 4.2.** DFB-OLED characteristics; (a) EQE versus current density plot at DC operation, EL spectra upon variation of current density (pulse operation) from (b) reference OLED device without DFB and (c) DFB-OLEDs device with second order DFB. Polarization dependence of the outcoupled light beams (d) emission intensity as a function of polarization angle (e) emission spectra at different polarizer angles.

### 4.2.2 Prospects of OSLDs

***Approach for optimizing DFB-OLEDs***

In order to enhance light amplification in OLEDs, there should be strong feedback of photons within the resonator structure[3–5] (See appendix A for detailed explanation). However, in single layer device structures, the hole and electron charge balance can be easily varied depending on the conditions of carrier injection and transport[1]. Therefore, it is important to finely optimize the injection characteristics until the recombination zone sites into the DFB (Figure 4.3). Moreover, next OSLDs might be designed with multilayer architecture that does not induce serious charge accumulation[6-11]. Furthermore, modifying pitch pattern, pitch height, and period of the

DFB may also enhance the optical feed-back, thus improving stimulated emission than optical losses.

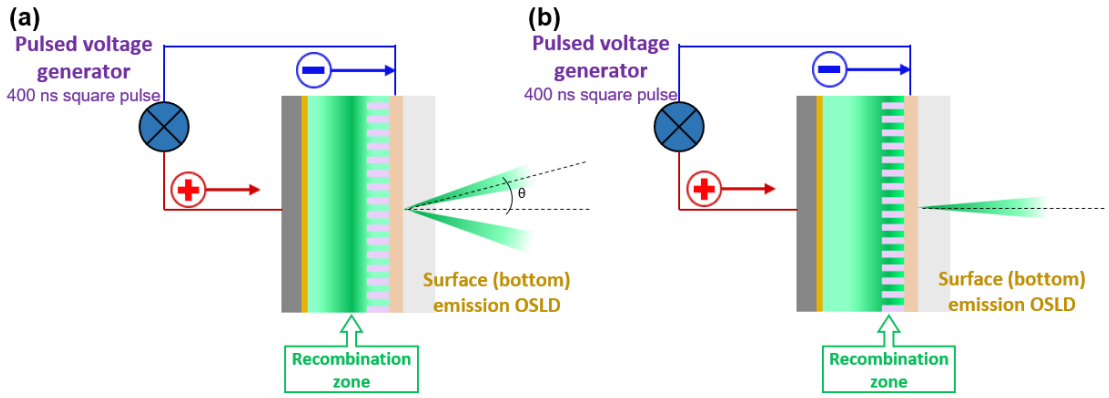


**Figure 4.3.** Proposed model of shifting charge recombination zone for stimulated emission enhancement.

***Approach for optimizing laser gain medium***

The material strategy can be further incorporated by designing and synthesizing new molecules with similar but improved optoelectronic properties. As an example, improving stability of triplet scavenging hosts by designing BSBCz derivatives with more rigid structures[12], or designing laser emitters with small $\Delta E_{ST}$ and higher $k_r$ which fit into singlet-triplet energy levels of BSBCz or derivatives are proposed. However, the designing criteria of molecules with a small $\Delta E_{ST}$ while maintaining a higher $k_r$ has some limitations. In general, a simplistic consideration has often been used in the context of TADF molecules; a very small $\Delta E_{ST}$ value can be obtained when there is the spatial separation of HOMO ad LUMO wavefunctions. Unfortunately, this spatial separation can reduce the transition from the $S_1$ state to the ground state ($S_0$) because of the lower exchange integral ($J$), resulting in the small oscillator strength ($f$), low PLQY, and low $k_r$. Therefore, the careful molecular design should be performed for effective and optimum HOMO-LUMO separation to strike the right balance of a small $\Delta E_{ST}$ along with a higher oscillator strength[13-17]. In addition, realization of red color OSLDs are still lagging due to the exciton losses as non-radiative relaxation. Thus, the triplet scavenging guest-host

system explained in this thesis can be utilized to fabricate red emission OSLDs.

### 4.2.3 Future aspects of triplet-management

In this thesis, one way of managing unwanted triplet excitons is demonstrated. However, instead of removing triplet excitons, there are some other methods for utilizing those triplet excitons into light generation. As an example, TADF mechanism[13-17] or TTA mechanism[18–23] can be utilized to upconvert triplet excitons into singlets. Adachi group reported a novel method, i.e., the TADF assisted fluorescence (TAF) system which employs a TADF molecule as an assistant dopant for a triplet harvester and a fluorescence molecule as an emitter[24–27]. By using a TADF molecule as a triplet harvester, lower ASE threshold was achieved[28]. However, regarding OSLDs which are operating at high current densities, this material combination has some intrinsic issues to overcome. To date, the maximum $k_{RISC}$ of the TADF molecules is around $10^6$ $s^{-1}$, meaning that the upconversion process occurs in the time scale around 1 μs[29,30]. However, laser is avalanche of radiation which occurs in short time scale within few picoseconds. Thus, TAF system provides insignificant contribution for lasing in OSLDs at this moment. However, designing TADF molecules with much faster $k_{RISC}$ will lead to enable the use of TAF system. Further, a TTA host can upconvert triplets into the higher energy singlet state such as $S_2$. Thus, it is advantageous for the electrical pumping where 75 % triplets are forming which might also enhance the device efficiency by utilizing those triplet excitons.

### References

[1] A. S. D. Sandanayaka, T. Matsushima, F. Bencheikh, S. Terakawa, W. J. Potscavage, C. Qin, T. Fujihara, K. Goushi, J. C. Ribierre, C. Adachi, *Appl. Phys. Express* **2019**, *12*, 061010.

[2] M. Wang, J. Lin, Y. C. Hsiao, X. Liu, B. Hu, *Nat. Commun.* **2019**, *10*, 1614.

[3] T. Zhai, X. Zhang, Z. Pang, *Opt. Express* **2011**, *19*, 6487.
[4] A. S. D. Sandanayaka, T. Matsushima, F. Bencheikh, K. Yoshida, M. Inoue, T. Fujihara, K. Goushi, J. C. Ribierre, C. Adachi, *Sci. Adv.* **2017**, *3(4)*, e1602570.
[5] A. S. D. Sandanayaka, K. Yoshida, M. Inoue, C. Qin, K. Goushi, J. C. Ribierre, T. Matsushima, C. Adachi, *Adv. Opt. Mater.* **2016**, *4*, 834.
[6] H. Nakanotani, K. Masui, J. Nishide, T. Shibata, C. Adachi, *Sci. Rep.* **2013**, *3*, 2127.
[7] J. Lee, N. Chopra, S. H. Eom, Y. Zheng, J. Xue, F. So, J. Shi, *Appl. Phys. Lett.* **2008**, *93*, 123306.
[8] C. Xiang, X. Fu, W. Wei, R. Liu, Y. Zhang, V. Balema, B. Nelson, F. So, *Adv. Funct. Mater.* **2016**, *26*, 1463.
[9] J. H. Lee, C. H. Chen, P. H. Lee, H. Y. Lin, M. K. Leung, T. L. Chiu, C. F. Lin, *J. Mater. Chem. C* **2019**, *7*, 5874.
[10] C. Murawski, K. Leo, M. C. Gather, *Adv. Mater.* **2013**, *25*, 6801.
[11] Y. J. Pu, G. Nakata, F. Satoh, H. Sasabe, D. Yokoyama, J. Kido, *Adv. Mater.* **2012**, *24*, 1765.
[12] Y. Oyama, M. Mamada, A. Shukla, E. G. Moore, S.-C. Lo, E. B. Namdas, C. Adachi, *ACS Mater. Lett.* **2020**, *2*, 161.
[13] H. Uoyama, K. Goushi, K. Shizu, H. Nomura, C. Adachi, *Nature* **2012**, *492*, 234.
[14] H. Sun, Z. Hu, C. Zhong, X. Chen, Z. Sun, J. L. Brédas, *J. Phys. Chem. Lett.* **2017**, *8*, 2393.
[15] X. Wei, Z. Li, T. Hu, R. Duan, J. Liu, R. Wang, Y. Liu, X. Hu, Y. Yi, P. Wang, Y. Wang, *Adv. Opt. Mater.* **2019**, *7*, 1801767.
[16] R. S. Nobuyasu, J. S. Ward, J. Gibson, B. A. Laidlaw, Z. Ren, P. Data, A. S. Batsanov, T. J. Penfold, M. R. Bryce, F. B. Dias, *J. Mater. Chem. C* **2019**, *7*, 6672.
[17] A. Pershin, D. Hall, V. Lemaur, J. C. Sancho-Garcia, L. Muccioli, E. Zysman-Colman, D. Beljonne, Y. Olivier, *Nat. Commun.* **2019**, *10*, 597.
[18] J. Y. Lee, K. H. Lee, S. O. Kim, J. N. You, S. Kang, J. Y. Lee, K. S. Yook, S. O. Jeon, S. S. Yoon, *J. Mater. Chem.* **2012**, *22*, 5145.
[19] D. Y. Kondakov, *Philos. Trans. R. Soc. A* **2015**, *373*, 20140321.
[20] B. Y. Lin, C. J. Easley, C. H. Chen, P. C. Tseng, M. Z. Lee, P. H. Sher, J. K. Wang, T. L. Chiu, C. F. Lin, C. J. Bardeen, J. H. Lee, *ACS Appl. Mater. Interfaces* **2017**, *9*, 10963.
[21] A. Ligthart, X. de Vries, L. Zhang, M. C. W. M. Pols, P. A. Bobbert, H. van Eersel, R. Coehoorn, *Adv. Funct. Mater.* **2018**, *28(52)*, 1804618.
[22] A. Dey, D. Kabra, *J. Phys. Chem. A* **2019**, *123*, 4858.
[23] C. Mayr, T. D. Schmidt, W. Brütting, *Appl. Phys. Lett.* **2014**, *105*, 183304.
[24] H. Nakanotani, T. Higuchi, T. Furukawa, K. Masui, K. Morimoto, M. Numata, H. Tanaka, Y. Sagara, T. Yasuda, C. Adachi, *Nat. Commun.* **2014**, *5*, 4016.

[25] T. Furukawa, H. Nakanotani, M. Inoue, C. Adachi, *Sci. Rep.* **2015**, *5*, 8429.

[26] R. Nagata, H. Nakanotani, C. Adachi, *Adv. Mater.* **2017**, *29(5)*, 1604265.

[27] Y. K. Wang, C. C. Huang, S. Kumar, S. F. Wu, Y. Yuan, A. Khan, Z. Q. Jiang, M. K. Fung, L. S. Liao, *Mater. Chem. Front.* **2019**, *3*, 161.

[28] H. Nakanotani, T. Furukawa, T. Hosokai, T. Hatakeyama, C. Adachi, *Adv. Opt. Mater.* **2017**, *5(12)*, 1700051.

[29] S. H. Han, J. H. Jeong, J. W. Yoo, J. Y. Lee, *J. Mater. Chem. C* **2019**, *7*, 3082.

[30] L. Zhang, K. W. Cheah, *Sci. Rep.* **2018**, *8*, 8832.

# Appendix A

## Fundamentals of DFB lasers

Laser oscillation in a DFB resonator was firstly demonstrated in 1971 by H. Kogelnik and C. A. V. Shank using a periodic structure of gelatin and organic laser dye "rhodamine 6G"[1]. The DFB cavity provides a distributed feedback mechanism as well as outcoupling through a selected diffraction order of an optical grating, which depends on the Bragg order ($\Lambda$) of the DFB lasers (Appendix Figure 1)[2,3]. The Bragg condition is $2n_{eff}\Lambda = m\lambda_{Bragg}$, where $\lambda_{Bragg}$ is the Bragg wavelength, $n_{eff}$ is the effective refractive index of the waveguide, $\Lambda$ is the period of the grating and m is the diffraction order responsible for light feedback. Therefore, lasing wavelength of a DFB laser and $\lambda_{Bragg}$ can be tuned by varying $n_{eff}$ or $\Lambda$ of the DFB laser device[4].

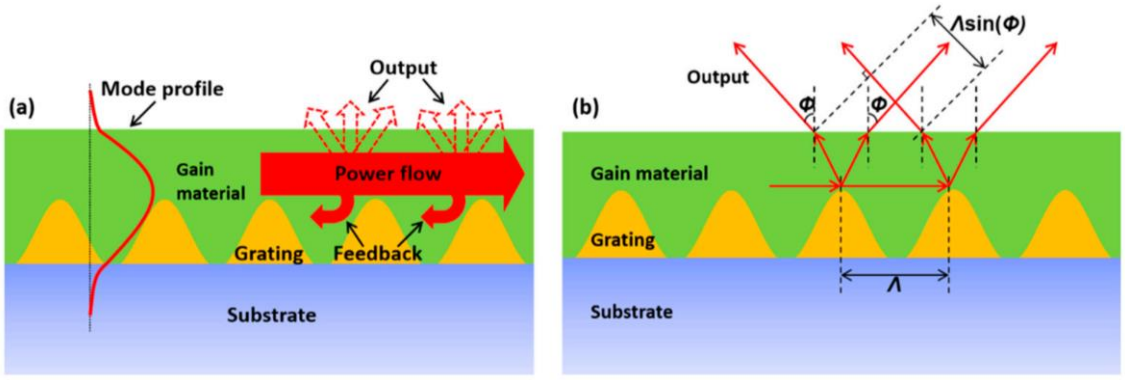


**Appendix Figure 1.** (a) Schematic of the feedback and the outcoupling of the waveguide mode; (b) diffraction theory of DFB lasers. Reproduced from Zhou, P. *et al.*, *Polymers* **2019**, *11*, 258[2].

When a light with a broad spectrum is spontaneously emitted in the DFB architecture, the part of the light with wavelength matching the Bragg grating wavelength ($\lambda_{Bragg}$) will be reflected back and forth creating feedback similar to a resonance cavity[4]. The fundamental principle behind this reflection phenomena is Fresnel reflection; when light travelling between media of different refractive indices could undergoes both reflection and refraction at the interface[3]. Thus, when the light travels through both grating material and organic gain material alternatively, it passes number of interfaces with different refractive index, yielding effective reflection feedback within the grating.

This transmission DFB grating geometry is called or periodic modulation of refractive index where the light reflected by Bragg scattering[5]. The strong feedback of these DFB structures helps to yielding stimulated emission over spontaneous emission with same wavelength (monochromatic) and same phase (coherence)[3]. There is another DFB laser architecture which was achieved using a reflection grating geometry[6].

At the same time of optical feedback, part of light will be outcoupled from the device due to the diffraction of light from the edge of the DFB ridges. Based on the period of Bragg grating ($\Lambda$), the constructive interference occurred at certain angle ($\phi$) called diffraction beam (Appendix Figure 1b)[2]. For a first order DFB laser, both feedback and outcoupling mechanisms are supported by first order diffraction whereas for a second order DFB laser, the feedback mechanism and output coupling are provided by second and first order diffraction, respectively. In general, for a $m^{th}$ order DFB laser, the feedback mechanism is always established via $m^{th}$ order diffraction. However, different diffraction orders below or equal to m could yield various light output coupling directions[2].

By theory, in a dielectric waveguide, if the angle of incident light wave is smaller than the critical angle of total internal reflection (dense to rare medium), it can refract through the interface. Thus, apart from the diffracted light from DFB ridges, most part of the light generation closer to the opposite surface of organic gain material (top surface in Appendix Figure 1) can be easily refracted out of the device as leaky waves. Since these leaky waves can have any angles of refraction, it does not support for the constructive interference of diffraction beams from DFB ridges[4]. As depicted in Appendix Figure 1a, the mode profile of the light propagation mode, is responsible for how much fraction of light is leaked out by refraction or feedback by reflection or outcoupled by diffraction from DFB ridge. Thus, it can be considered light generation within the DFB trenches or closer to DFB ridges are mainly responsible for light feedback as well as the for the

diffracted light beams from DFB ridges. Based on this discussion, I proposed optimization of recombination zone of DFB-OLEDs into DFB trench or closer to DFB ridge is required in future experiments for better feedback and diffraction.

Moreover, the mode profile, which is schematically drawn on the Appendix Figure 1a is depends on the $n_{eff}$ of slab waveguide of gain material[2]. Although the thin film of the gain material has a wavy pattern as shown in Appendix Figure 2a, the $n_{eff}$ usually modelled using a uniform slab waveguide (Appendix Figure 2b) and the value can be estimated by solving the propagation wave equation[7]. For a uniform slab waveguide, $n_{eff}$ depends on $n_a$, $n_f$, $n_s$, and $d_f$ which are refractive index of air, organic gain material, substrate, and wave guided film thickness, respectively.

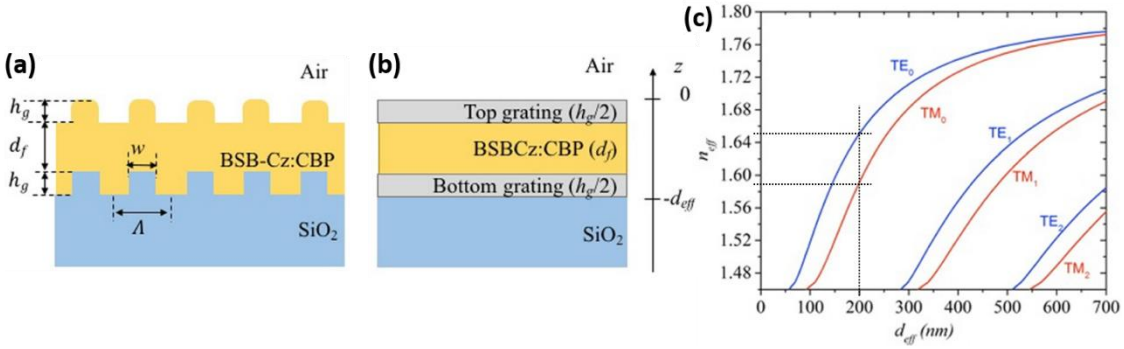


**Appendix Figure 2.** (a) Scheme of the trilayer slab waveguide. (b) $n_{eff}$ values for the TE and TM modes as a function of $d_{eff} = d_f + 2(h_g/2)$ at a lasing wavelength of 477 nm for 6 wt.%-BSBCz:CBP film. Reproduced from F. Bencheikh *et al.*, **2017**, *121*, 233107[7].

To estimate effective film thickness ($d_{eff}$) in DFB architecture, half of the pitch height of trenches and ridges are added to each side of the thin film as shown in Appendix Figure 2a,b. Thus, based on these approximations, F. Bencheikh *et al.* estimated effective film thickness as $d_{eff} = d_f + 2(h_g/2)$ and then $n_{eff}$ for each transverse electric (TE) and transverse magnetic (TM) mode for 6 wt.%-BSBCz:CBP film[7] as depicted in Appendix Figure 2c. This figure shows the $n_{eff}$ values of 1.65 and 1.59 for $TE_0$ and $TM_0$ modes, respectively, when the film thickness is 200 nm. Thus, the light

confinement within the thin film slab wave guide is high for TE mode. Therefore, light outcoupled from the ridges of DFB (Appendix Figure 1b) gave constructive interference as laser beams at certain angle ϕ consisting with TE mode polarization. When the DFB period (Λ) is set to first order Bragg condition, the constructive interference occurs at ϕ = 90°, the edge emission laser is observed where we can see TE mode polarization parallel to substrate plane. When the DFB period (Λ) is set to second order Bragg condition, the constructive interference of diffracted waves from DFB ridges occurs at ϕ = 0° as surface emission, where we can see TE mode polarization parallel to the 1D-DFB ridges.

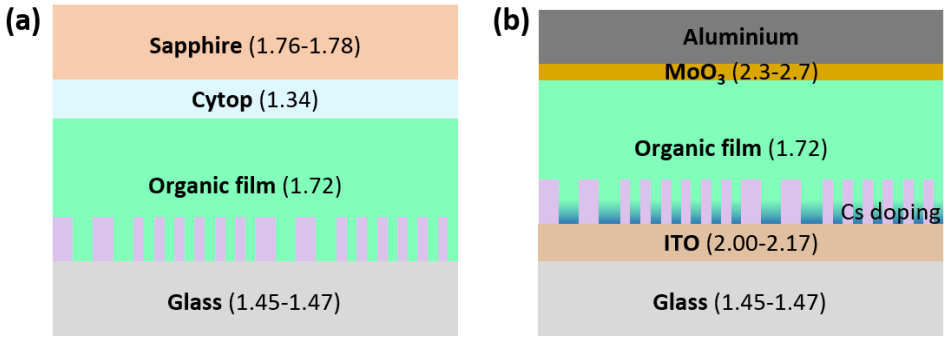


**Appendix Figure 3.** Schematic representation of refractive index of each layer for my DFB laser devices, (a) device for optical pumping (b) device for current injection OSLD.

As depicted in Appendix Figure 3, I used the reported $n_{eff}$ value calculated for BSBCz neat film[8], assuming that the $n_{eff}$ is not significantly changed when 1 wt.%-DCNP is doped in BSBCz. As depicted in Appendix Figure 3a, organic film has high refractive index comparing to adjacent materials, suggesting high light confinement within the slab waveguide. However, in DFB-OLED device architecture, both adjacent layers (charge injection layers) have higher refractive index than organic material. Thus, thickness of those layers was kept small in order to reduce the waveguide losses within the DFB structure. In addition, I used inverted-OLED device architecture where electrons are injected from ITO side and holes are injected from Al side in order to shift the

recombination zone closer to DFB trench pattern. As explained in the previous paragraph both of my optical driven lasers and DFB-OLEDs, TE mode plane-polarized light was outcoupled parallel to the trench-ridge pattern of DFB in all first, second and mixed order devices (Appendix Figure 4).

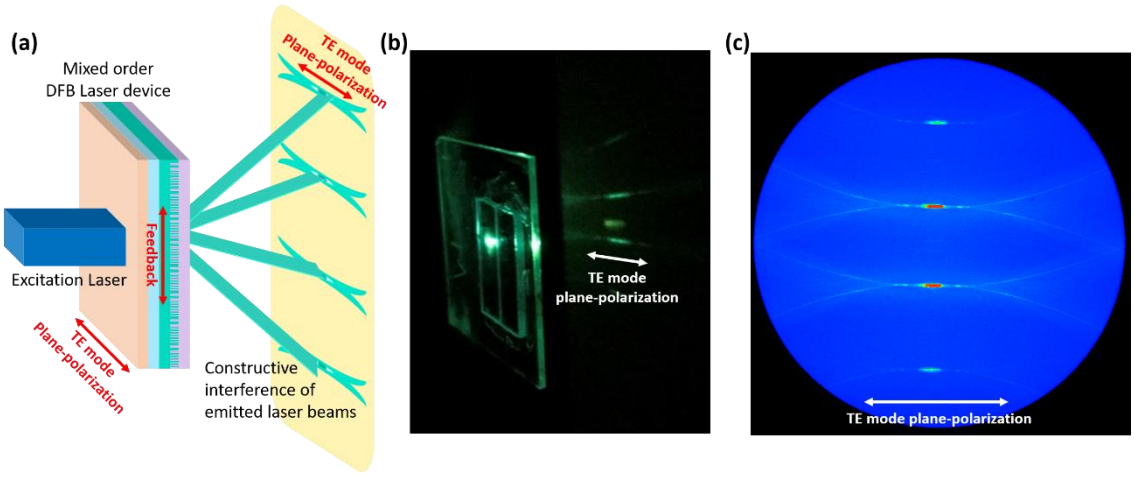


**Appendix Figure 4.** (a) Schematic orientation of DFB trench-ridge pattern, feedback and respective TE mode plane-polarized laser emission (b) the same in photograph, (c) far-field interference beam observed on CCD camera and respective orientation of TE mode plane-polarization.

In addition to the diffraction from the ridges of DFB, plane-polarized light emission could occur in a dielectric slab waveguide if the dipole moment of molecules is parallel to the slab waveguide. At this condition, the emitted light has its electric field component parallel to the plane of slab waveguide, while magnetic field component is perpendicular to the waveguide. Thus, if the light travels within the slab wave guide which causes light amplification such as ASE, the emitted beams have higher ratio of TE mode polarization parallel to the plane of slab wave guide[5,7,9].

As depicted in Appendix Figure 5, R. Ding *et al.* demonstrated intrinsic polarization at different wavelengths of EL from organic single-crystal based light emitting diodes[10]. In their experimental results of surface emission which was measured at normal direction to the device surface, the polarization ratio was TE:TM is 5:1 at the emission peak of 575 nm, and 1:4.7 at the emission peak of 635 nm, respectively

(Appendix Figure 5b). They ascribed it for the alignment of transition dipole moments of molecules in a nearly vertical direction using a organic single crystal (Appendix Figure 5a)[10]. However, this result contradicts to the TE polarization observed in ASE of a slab waveguide, which favors for horizontal orientation of molecules having transition dipole moment parallel to the slab waveguide.

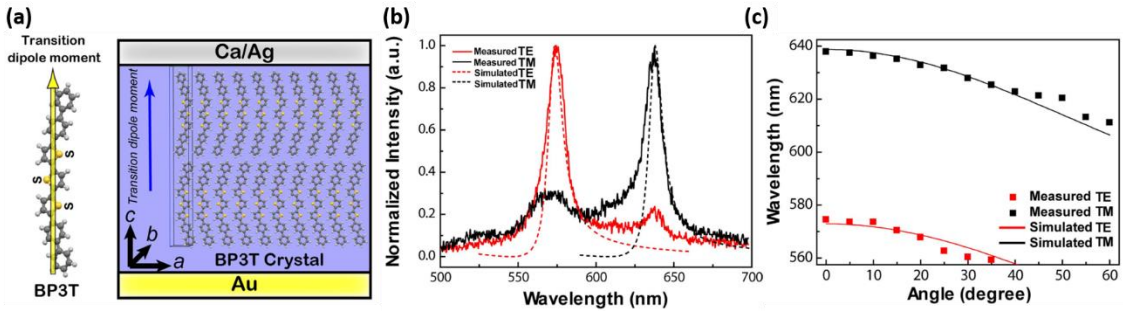


**Appendix Figure 5.** (a) The molecular orientation in BP3T single crystal OLEDs, (b) EL spectra of TE and TM modes measured at normal to OLED surface (c) Wavelength of TE and TM mode variation upon angle of detection. Reproduced from R. Ding *et al.*, *Sci. Rep.* **2015**, *5*, 12445[10].

Moreover, circularly polarized lasing was also demonstrated by F. Chen *et al.* using reflection-DFB type dye lasers[6]. In their experiment, a solution of 4-(dicyanomethylene)-2-methyl-6-(4-dimethylaminostyryl)-4H-pyran (DCM) doped methanol is used as laser gain medium where we could not expect particular molecular orientation. Based on these results, it can be concluded, even though molecular orientation is important to get plane-polarized ASE from a slab waveguide, it is not a mandatory requirement to get plane-polarized laser emission using DFB structure.

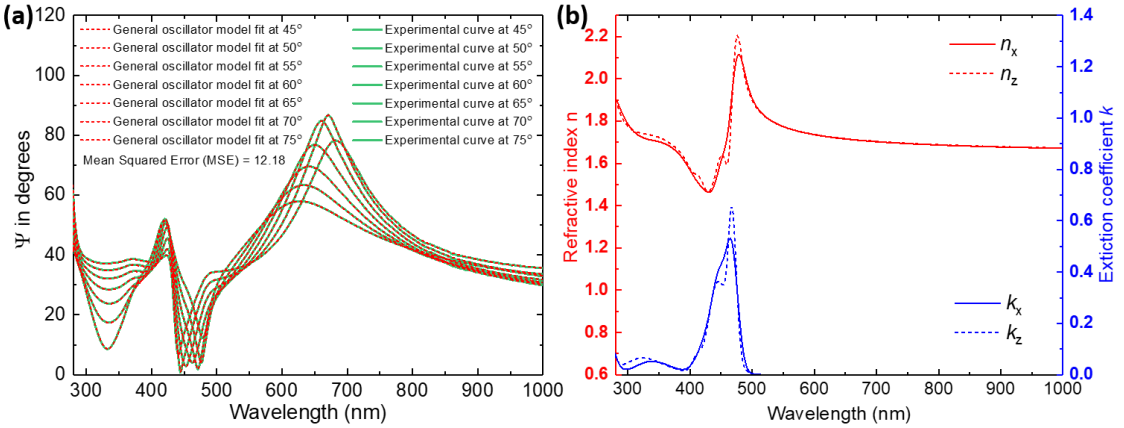


**Appendix Figure 6.** VASE measurement of DCNP neat film (a) Fitting result using Cauchy model, (b) estimated ordinary and extraordinary refractive index versus wavelength.

In my DFB laser devices, the gain medium was 1 wt.%-DCNP:BSBCz host guest system. Although BSBCz molecules have uniaxial anisotropy, which should induce large birefringence for TE and TM modes, the DCNP molecules have completely random orientation, yielding isotropic effect for TE and TM modes in VASE measurement. As shown in Appendix Figure 6, even partially crystalized DCNP film showed good fitting for general oscillator model, indicating molecules have similar curves for ordinary ($k_x$) and extraordinary ($k_z$) refractive index (Appendix Figure 6b), thus dipole moment of DCNP molecules is completely random[11]. Therefore, the TE mode plane-polarization of laser emission occurred not due to the planer orientation of dipole moment of emitter molecules but due to the diffraction from the DFB ridges.

**References:**

[1] H. Kogelnik, C. V. Shank, *Appl. Phys. Lett.* **1971**, *18*, 152.

[2] P. Zhou, L. Niu, A. Hayat, F. Cao, T. Zhai, X. Zhang, *Polymers (Basel).* **2019**, *11*, 258.

[3] K. Porsezian, K. Senthilnathan, In *Guided Wave Optical Components and Devices*; Pal, B. P., Ed.; Academic Press: Burlington, 2006; pp. 251–280.

[4] Y. Fu, T. Zhai, *Front. Optoelectron.* **2020**, *13*, 18.

[5] M. D. McGehee, A. J. Heeger, *Adv. Mater.* **2000**, *12*, 1655.

[6] F. Chen, D. Gindre, J.-M. Nunzi, *Opt. Express* **2008**, *16*, 16746.

[7] F. Bencheikh, A. S. D. Sandanayaka, T. Matsushima, J. C. Ribierre, C. Adachi, *J. Appl. Phys.* **2017**, *121*, 233107.

[8] A. S. D. Sandanayaka, T. Matsushima, F. Bencheikh, S. Terakawa, W. J. Potscavage, C. Qin, T. Fujihara, K. Goushi, J. C. Ribierre, C. Adachi, *Appl. Phys. Express* **2019**, *12*, 061010.

[9] M. D. McGehee, M. Diaz-Garcia, F. Hide, R. Gupta, E. K. Miller, D. Moses, A. J. Heeger, *Appl. Phys. Lett.* **1998**, *72*, 1536.

[10] R. Ding, J. Feng, W. Zhou, X. L. Zhang, H. H. Fang, T. Yang, H. Y. Wang, S. Hotta, H. B. Sun, *Sci. Rep.* **2015**, *5*, 12445.

[11] D. H. Kim, A. S. D. Sandanayaka, L. Zhao, D. Pitrat, J. C. Mulatier, T. Matsushima, C. Andraud, J. C. Ribierre, C. Adachi, *Appl. Phys. Lett.* **2017**, *110*.

## List of Publications

### *Publications as first author:*

1) Buddhika S. B. Karunathilaka, Umamahesh Balijapalli, Chathuranganie A. M. Senevirathne, Yu Esaki, Kenichi Goushi, Toshinori Matsushima, Atula S. D. Sandanayaka and Chihaya Adachi. *Advanced Functional Materials*, (in press, 2020), An organic laser dye having a small singlet-triplet energy gap makes the selection of a host material easier. DOI: 10.1002/adfm.202001078.
2) Buddhika S. B. Karunathilaka, Umamahesh Balijapalli, Chathuranganie A. M. Senevirathne, Seiya Yoshida, Yu Esaki, Kenichi Goushi, Toshinori Matsushima, Atula S. D. Sandanayaka and Chihaya Adachi. *Nature Communications*, (in peer-review, 2020). Suppression of external quantum efficiency rolloff in organic light-emitting diodes by scavenging triplet excitons.

### *Patents:*

1) Atula S. D. Sandanayaka, Buddhika S. B. Karunathilaka, Umamahesh Balijapalli, Chathuranganie A. M. Senevirathne, Toshinori Matsushima, and Chihaya Adachi. Laser element, JP2019-178599, 30$^{th}$ September, 2019.
2) Atula S. D. Sandanayaka, Chathuranganie A. M. Senevirathne, Buddhika S. B. Karunathilaka, Toshinori Matsushima, and Chihaya Adachi. Laser element, JP2020-031025, 26$^{th}$ February, 2020.

### *List of presentations at international conferences:*

1) Buddhika S. B. Karunathilaka, Umamahesh Balijapalli, Chathuranganie A. M. Senevirathne, Yu Esaki, Toshinori Matsushima, Atula S. D. Sandanayaka and Chihaya Adachi. Oral presentation 12p-A409-13, *The 67th JSAP Spring Meeting*, Tokyo, Japan, 12$^{th}$ March 2020, Novel lasing dye having small $\Delta E_{ST}$ easing the selection of host materials.
2) Buddhika S. B. Karunathilaka, Umamahesh Balijapalli, Chathuranganie A. M. Senevirathne, Yu Esaki, Toshinori Matsushima, Atula S. D. Sandanayaka and Chihaya Adachi. Oral presentation 11473-8, *SPIE Organic Photonics + Electronics*, San Diego, California United States of America, 23 August 2020, Continuous-wave laser operation based on triplet management of guest-host matrix.

# List of Abbreviations

***Keywords***

Amplified spontaneous emission (ASE)

Continuous wave (CW)

Förster resonance energy transfer (FRET)

Dexter energy transfer (DET)

Nuclear magnetic resonance (NMR)

Distributed-feedback (DFB)

Direct current (DC)

Electroluminescence (EL)

Electron-injection layer (EIL)

Hole-injection layer (HIL)

Electron-blocking layer (EBL)

Electron-transport layer (ETL)

Emitting layer (EML)

External quantum efficiency (EQE)

Full width at half maximum (FWHM)

Highest occupied molecular orbital (HOMO)

Hole-blocking layer (HBL)

Hole-transport layer (HTL)

Intersystem crossing (ISC)

Lowest singlet excited state ($S_1$)

Lowest triplet excited state ($T_1$)

Lowest unoccupied molecular orbital (LUMO)

Organic light-emitting diodes (OLEDs)

Phosphorescent organic light-emitting diode (PHOLED)

Organic semiconductor laser diodes (OSLDs)

Photoluminescence (PL)

Photoluminescence quantum yield (PLQY)

Reverse intersystem crossing (RISC)

Singlet ground state ($S_0$)

Singlet-polaron annihilation (SPA)

Singlet-singlet annihilation (SSA)

Singlet-triplet annihilation (STA)

Thermally activated delayed fluorescence (TADF)

Thermally activated delayed fluorescence assisted fluorescence (TAF)

Triplet-polaron annihilation (TPA)

Triplet-triplet annihilation (TTA)

***Materials***

Aluminum (Al)

Cesium (Cs)

Molybdenum trioxide ($MoO_3$)

2,6-dicyano-1,1-diphenyl-$\lambda^5\sigma^4$-phosphinine (DCNP)

4,4'-bis[(*N*-carbazole)-styryl]biphenyl (BSBCz)

4,4'-bis(*N*-carbazolyl)-1,1'-biphenyl (CBP)

tris(2-phenylpyridinato)iridium(III) [$Ir(ppy)_3$]

Indium tin oxide (ITO)

Silicon dioxide ($SiO_2$)

***Physical symbols***

Absorption cross-section ($\sigma_a$)

ASE/laser threshold ($E_{th}$)

Current density (J)

Effective refractive index in an emission region ($\eta_{eff}$)

Einstein's B coefficient ($B$)

Energy gap between a lowest singlet excited state and a lowest triplet excited state ($\Delta E_{ST}$)

External quantum efficiency ($\eta_{EQE}$)

Light out-coupling efficiency of OLEDs ($\eta_{out}$)

Period of grating ($\Lambda$)

Photoluminescence lifetime ($\tau$)

Photoluminescence peak wavelength ($\lambda_{max}$)

Photoluminescence quantum yield ($\Phi_{PL}$)

Rate constant of intersystem crossing from a lowest singlet excited state to a lowest triplet excited state ($k_{ISC}$)

Rate constant of non-radiative decay from a lowest triplet excited state to ground state

($k^T_{nr}$)

Rate constant of radiative emission from a lowest singlet excited state to a ground state ($k_r$)

Rate constant of reverse intersystem crossing from a lowest triplet excited state to a lowest singlet excited state ($k_{RISC}$)

Temperature (*T*)

Triplet lifetime ($\tau_T$)

Wavelength ($\lambda$)

Wavelengths of ASE ($\lambda_{ASE}$)

Voltage (V)

## Acknowledgements

First, I would like to pay my honoured gratitude to my advisor senior professor Chihaya Adachi for accepting me into his world-renowned research group as a PhD student. It is such a privilege and honour to study research work in this highly sophisticated laboratory on the way to become a future scientist. Professor Adachi being so patient throughout the entire duration of my graduate student life, beginning from the research proposal, departmental progress presentations, purchasing chemicals and laboratory equipment, revisions of paper publications, suggesting cover pages for journals, suggesting patent applications during thesis revision, granting me unparalleled freedom to conduct scientific research at any time and so much more. It is very important to note my father got seriously ill, just four months after I joined Kyushu university. At that time Adachi sensei not only gave me his full support to go back to my country and spend time with my father as it required but also sent his sympathies with an endowment for alms giving to Buddhist monks as a religious ritual. When I became the best presenter at departmental progress review of my first year of PhD studies, Adachi sensei congratulate me by offering a special party with another famous scientist professor Eli Zysman Colman. Afterwards, Adachi sensei encouraged me by offering a 10 days training program at St. Andrews University, Scotland which was fully funded by Japan society for the promotion of science (JSPS) core to core programme, where I gathered lots of knowledge regarding molecular simulations and calculations. I do not know how to return his favour now, but I will surely carry on the spirit of always avoiding careless mistakes, thinking originality and acting passionately for the research and life.

When I looked back, I found my research direction was not clear, and I spent a lot of time in another field of interest. To rearrange the topic, professor Adachi allowed me to focus on organic lasers with the help of professor Atula Sandanayaka.

Professor Atula dedicated his full commitment and support throughout this work beginning from the ideas of the work until the completion of this thesis. Working continuously throughout day and nights with prof. Atula and having only a couple of hours to rest or sleep pushed me to the statement of "hard work paid off". Simultaneously, we had multiple discussion with Professor Adachi to direct the research progress in the proper direction. Finally, the extreme effort became to a success with two patent publications, two papers in high impact journals and conference proceedings. Without professor Atula's excellent mentorship and experience to guide a student like me, the work described herein would not have been possible.

I also deeply grateful to the other members of my committee, professor Hiroyuki Furuta and professor Yuji Oki for serving on my dissertation committee and their kindly, helpful suggestions and comments on my presentation and thesis.

I would like to pay my sincere gratitude to associate professor Youichi Tsuchiya who was serving the entire initial two years of my PhD as my co-supervisor, and Dr Morgan Auffray who was my immediate post-doctoral mentor. When I joined into Adachi laboratory my knowledge regarding organic photonics and applications were very poor. Tsuchiya sensei and Dr Morgan helped me to lay down an excellent foundation of knowledge and strengthen me to become an efficient researcher. They taught me so many experimental procedures, starting from the photophysical measurements to the OLED fabrications. The knowledge, skills and experience gathered during this period driven me to become an independent researcher who can debate with correct facts and matters in the discussions in front of more experienced researchers.

I would also like to highly appreciate associate professor Toshinori Matsushima for kindly revising my paper publications and thesis while guiding me for the higher possibility of acceptance of the papers. He dedicates an enormous amount of his valuable

time to improve my written documents up to the standard and attractive level.

My special thanks to Dr Umamahesh Balijapalli who synthesized DCNP in large amounts and found initial ASE characteristics beforehand. This special molecule leads me to get one patent using its unique properties. I would like to pay my gratitude to assistant professor Kenichi Goushi, for his incessant help for research discussion, measurement and instrumentation. Especially his experimental support and discussion helped me to pass through the reviewers' comments of my first paper publication. My sincere appreciation to prof Ryota Kabe especially regarding streak camera measurement.

I would like to express my appreciation to prof. Hajime Nakanotani and assoc. prof. Masashi Mamada for their kind suggestions and comments during my study since my first regular meeting presentation. Further, my sincere gratitude to Dr Takashi Fujihara for setting CW laser testing setup, Dr Ryutaro Komatsu and Dr Jun-ichi Nishide for their technical assistance regarding new deposition chamber. My special thanks to Ms Chathuranganie Senevirathne and Mr Xun Tang, Mr Jaehyun Bae for teaching me DFB fabrication, doing research discussion, and being a close friend during this whole period of study. My specific thanks to Mr Seiya Yoshida for introducing me into the mountaineering club while helping me to blend with Japanese society. I am highly appreciating Mr Koudai Ikesue especially for teaching me molecular simulations and calculations, Dr Masaki Tanaka for teaching me EQE and ellipsometry instruments, Dr Yu Esaki for teaching me ellipsometry instrument, Mr. Ryo Nagata for teaching me magneto EL setup and photolithographic technique, Mr Kazuya Jinnai for helping me with the new streak camera setup, Mr Yuya Oyama for teaching me cyclic voltammetry.

Furthermore, I am also indebted to all my fellow Adachineses for offering their help and advice whenever I was in need, Dr Hao Ye, Dr Daichi Okada, Mr Tai Cheng, Mr Ganbaatar Tumen-Ulzii, Dr Chin-Yiu Chan, Dr Kou Yoshida, Dr Fatima Bencheikh,

Dr Matthew Leyden, Dr William J. Potscavage, Dr Yi-Ting Lee, Dr Zesen Lin, Mr Masayuki Yokoyama, Mr Ryota Nakamura, Mr Nguyen Thanh Ba, Mr Naohiro Nishimura, Ms Ayano Abe, Mr Tomohiro Ishii, Mr Ieuji Ryota, Mr Kenta Yamaguchi, Mr Shinichi Tan, Mr HyunSuk Park, Mr Naoto Noutsuka, Mr Ryo Akamatsu, and all other students. And I also want to thank all the staffs of Adachi lab for kindly support on my life, study and experiments. Especially to Ms Mayumi Kudo, Ms Rei Sasagawa, Ms Hiroko Kuratomi, Ms Sachiko Higashikawa, Mrs Yuko Kawahara for their always kindly assistance on study and life, Ms Keiko Kusuhara, Ms Nozomi Nakamura, Ms Shinobu Terakawa for their kindly help on technical support.

My research and work in this thesis owe their existence to the influence of all the members of Adachi laboratory and all persons whom I met through these three years. Finally, I would like to thank Ministry of Education, Culture, Sports, Science and Technology (MEXT), JSPS core to the core programme and Japan Science and Technology Agency (JST), ERATO, Adachi Molecular Exciton Engineering Project for financial support that made it possible to complete this study. Last but not least, I would also like to express my gratitude to my parents, my sister and my close friends for their moral support and unwavering love. I dedicate this thesis to them and hope that whatever I have accomplished to date and, in the future, will stand testimony to the fact that all their hard work and sacrifice over the years have not been in vain.

15th July, 2020.

K. P. W. Buddhika S. B. Karunathilaka